Review

Microscale combustion: Technology development and fundamental research

Yiguang Ju [a], Kaoru Maruta [b],*

[a] Department of Mechanical and Aerospace Engineering, Princeton University, Princeton, NJ 08544-5263, USA
[b] Institute of Fluid Science, Tohoku University, Sendai, Miyagi 980-8577, Japan

ARTICLE INFO

ABSTRACT

The high energy density of hydrocarbon fuels creates a great opportunity to develop combustion based micro-power generation systems to meet increasing demands for portable power devices, micro unmanned aerial vehicles, micro-satellite thrusters, and micro chemical reactors and sensors. In this paper, the recent technological development of micro-power systems and progress in fundamental understanding of micro-scale combustion are reviewed. At first, micro-scale combustion regimes are categorized by using different physical and chemical length and time scales and the resulting non-dimensional parameters and their correlations to various combustion regimes for micro and mesoscale combustion are discussed. Secondly, the recent successful developments and technical challenges of micro-thrusters, micro internal combustion engines, and micro chemical reactors summarized. Thirdly, the underlying fundamental mechanisms and ignition and flame dynamics in micro-scale combustion are reviewed, respectively, in premixed, non-premixed, catalytic, and non-equilibrium, micro-scale combustion systems. The conventional concepts of combustion limits such as the flammability limit, quenching diameter, and flame extinction and heat recirculation are revisited. The unique thermal and chemical transport mechanisms such as flame structure interaction, radical quenching, non-equilibrium transport appearing in micro-scale combustion are discussed. New flame regimes and instabilities such as flame bifurcation, weak flames, flame cells/streets, thermal and kinetic quenching, flameless low temperature catalytic combustion, repetitive extinction and ignition, spinning flames, spiral and multi-branched flames, symmetric and asymmetric oscillating flames are discussed. Finally, an overview of future research and conclusion are made. The goal of this review is to present an overview of the development of micro-power generators by focusing more on the advance in fundamental understanding of micro-scale combustion.

© 2011 Elsevier Ltd. All rights reserved.

Contents

* Corresponding author. Tel.: +81 22 217 5319; fax: +81 22 217 5311.
  E-mail address: maruta@ifs.tohoku.ac.jp (K. Maruta).

1. Introduction

1.1. Needs of micro-scale combustion

The recent development of nano and micro-fabrication technologies have accelerated dramatically the minimization and multi-functionalization of micro-mechanical, portable, communicational, imaging, sensing, chemical analytical, and biomedical devices. These devices require a compact, long lifetime, and instantly rechargeable power supplies capable of providing power from several milliwatts to hundreds watts. Today, these portable devices heavily rely on batteries, creating a battery market of $37 billion per year [1]. With the rapid growth of portable devices such as cellular phones, notebook computers, and personal power, the market request for small power generators will continue to grow. Unfortunately, the energy density of the existing batteries is very low. Even the most advanced lithium ion batteries only have an energy density about 0.20 kWh/kg [2,3]. This low energy density can only support a few hours for notebook computers and video cameras. In addition, batteries need several hours to recharge and only have a limited number of rechargeable cycles. Moreover, battery disposal for being used causes various environmental concerns. The lack of compact, durable, efficient, light weight, and instantly rechargeable power sources limits greatly the development of micro-mechanical and chemical systems for various applications.

Micro-satellite thrusters for station keeping require a small thrust (1–1000 mN) and a high specific impulse (250–450 s) with a small impulse bit ($\sim$1–5 Ns) for an operation period of years [4]. Therefore, an efficient micro-thruster requires propellants with a large energy density ($\sim$4 kWh/kg for solid propellants) and to have an accurate thrust control. Unfortunately, a battery based thruster is unable to provide such a specific impulse and has a very low thrust to weight ratio. In addition, existing solid rockets and catalytic monopropellant thrusters are not able to provide such a low thrust and at the same time providing high specific impulse [5]. Although pulsed thrusters produce a small impulse bit they have a low specific impulse because of the low energy density of propellants and heat losses. Moreover, micro-air vehicles for reconnaissance and surveillance in urban and battle field also require compact and efficient power generators for propulsion and

electricity supplies ranging from 1 W to 1000 W [6,7]. Therefore, the development of efficient micro-thrusters is critical for both micro-satellites and micro-air vehicles.

Micro-sensing and chemical analytical systems also use a micro-reactor and provide new opportunities to analyze a small amount of chemical substances rapidly and efficiently for safety detection and security [8]. A typical micro-reactor for chemical analysis comprises of a temperature control system, valves, pumps, sensors, actuators, and motors. As such, delivery of chemical species, species analysis, and actuation of sensors on a microchip chemical analyzer needs an efficient micro-combustor to raise reaction temperature, to provide partial oxidation, and to deliver electrical power. Obviously, a battery is not an appropriate option because of its low density.

Recently, with the advances in the fabrication technologies for microelectromechanical systems (MEMS), efforts are moving toward the integration of microelectronic and micro-mechanical systems on a single chip. The acceleration sensors developed for automobile air bags is an example of the commercialization of such integration. Unfortunately, today's MEMS are still relying on an external power. Therefore, there is a great need to combine the micromachined electronic and mechanical systems with an on chip micro-power (power MEMS). The availability of efficient micro-power generators will significantly enhance the functionality of MEMS for many portable devices.

Furthermore, the development of advanced communication systems such as the 4G cellular phones and multi-CPU notebook computers presents new challenges to portable power generators requiring increased energy density and reduced recharge time. In addition, biomedical devices for drug delivery and artificial heart also need efficient and compact power sources. Therefore, the development of new micro-power devices with a high energy density to replace existing batteries is critical to meet the demands of technological innovations.

In order to increase the operational lifetime of a power device, the energy densities of the fuels and the energy conversion systems need to be examined. Fig. 1 shows the comparison of energy densities between lithium ion batteries, hydrocarbon fuels, mono-propellants, diesel engines, micro-engines, and micro-fuel cells [9]. It is seen that the most advanced currently available lithium ion batteries have an energy density of 0.2 kWh/kg [3], which is almost one sixtieth of hydrocarbon fuels (e.g. methane and diesel). In
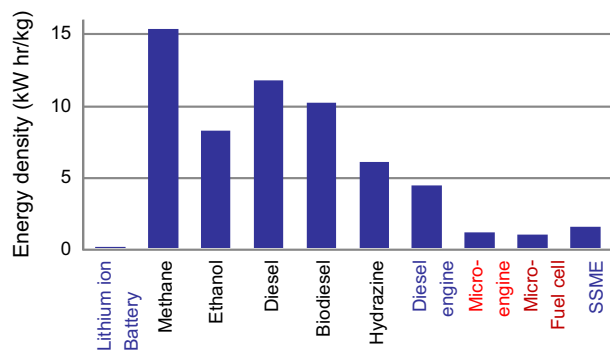
Fig. 1. Comparison of specific energy densities of lithium ion batteries with hydrocarbon and oxygenated hydrocarbon fuels as well as different engines [2].

addition, the energy density of lithium battery is also one twentieth of a diesel engine (200 kW with 450 kg engine weight), and one eighth of the space shuttle main engine (SSME, 1.8 MN thrust and 730,000 kg of propellants with an exhaust gas velocity of 4400 m/s for 540 s). This comparison clearly shows that by using liquid hydrocarbon fuels, even with 10% of energy conversion efficiency, the energy density of a micro-combustor is six times higher than that of a lithium battery. In addition, it is also noticed that a liquid hydrocarbon fuel based micro-thruster will have a higher energy density than hydrazine based monopropellant rockets for satellite station keeping. With the decrease of power device, the weight of combustor chamber significantly decreases at elevated pressures. Micro-engine may have much higher energy density than that of conventional engines. Chigier et al. [6] estimated that a micro-combustor can achieve energy density up to 10 kWh/kg. In addition, micro-engines do not need long time recharging and is cheap and chemically stable. As such, a hydrocarbon fuel based micro-combustor can replace lithium ion batteries to deliver much higher specific energy density and specific power for the development of microelectromechanical devices for biomedical applications, chemical sensing, telecommunication, and micro-propulsion.

1.2. Scaling parameters of micro-scale combustion

In last ten years, various micro-thrusters [4,10–13], micro-engines [2,14–19], micro-reactors [8,20] have been developed. Due to the arbitrary choices of reference length scales the definition of "micro-scale combustion" becomes ambiguous and sometimes is confused with "mesoscale combustion". In general, in previous studies, three different length scales have been used in the definition of "micro-scale" combustion (Table 1). One length scale, which has been widely used to define "micro-scale" and "mesoscale" combustion, is the physical dimension of the combustor. If the combustor physical length scale is below 1 mm, the combustion

is called micro-combustion. Otherwise, if the physical length scale is larger than 1 mm but in the order of 1 cm, the combustion is called mesoscale combustion. This definition is widely used in the development of micro-engines [2]. The second definition is to use a reference length scale of flame, the quenching diameter [21]. In this way, the combustion is called micro-scale (mesoscale) if the combustor size is smaller (larger) than the quenching diameter. This definition makes more sense in terms of physical flame regimes and is favored by researchers for fundamental studies of micro-combustion. However, since the quenching diameter is a function of mixture composition and wall properties (temperature and surface reactivity), it is difficult to quantitatively define the boundary of micro and meso combustion. A third way to define meso and micro-scale combustion is to use the relative length scale of the entire device to that of conventional large scale devices for similar purposes. For example, a micro-combustor for a micro-satellite does not necessarily mean the combustor is micro-scale [4]. It only indicates that the combustor is used for a micro-satellite, which is about 10–100 kg and is "micro" compared to a typical commercial satellite (above 1000 kg). Therefore, this definition is sometimes used by researchers to develop micro-thrusters for specific applications.

Micro-combustion depends on many physical and chemical processes such as gas-phase and surface reactions, molecular transport, thermal and mass diffusion, convection, and radiation. The combustion process for micro-power generation involves many different length and time scales. Table 2 lists some important length and time scales which strongly affect the phenomena of micro-scale and mesoscale combustion. Note that the combustor length scale is the characteristic size of combustor inner diameter and the combustor structure scale is the characteristic length scale of the structure (solid phase). The quenching diameter is about a few times (n) of the flame thickness depending on the wall temperature. For a wall temperature at room temperature, n is about 15. The time scale of heat loss is a function of convective and radiative heat losses. The acoustic wave time scale depends both on the span-wise and streamwise dimensions of the combustor.

The effects of the length and time scales on combustion in small scale are listed in Table 3 by using non-dimensional parameters. For example, when the combustor size is in the order of 10 times that of flame thickness or close to the quenching diameter, flame extinction or flame instability starts to occur due to wall heat loss and/or radical quenching depending on the wall temperature. In addition, mixing of fuel and oxidizer is limited by molecular diffusion. With the coupling of wall heat loss and auto-ignition at isolated hot spots, isolated flame cells as well as steady or unsteady flame streets can be observed. As the structure of the combustor decreases, the time scale of thermal diffusion in solid phase becomes comparable to the time scale of combustion, the flame temperature begins to couple with the temperature of the structure, leading to multiple flame regimes in which both normal flame

Table 1
Definition of micro-scale and mesoscale combustion using different length scales.

Definition based on	Combustion regime	Length scale	Examples	Applications
Physical length	Mesoscale	1–10 mm	Rotary engine (UCB)	MEMS power
	Microscale	1–1000 μm	Micro-reactor (UIUC)	Thruster
Flame quenching diameter	Mesoscale	~Quenching diameter (equilibrium)	Swiss-roll combustor (USC)	Power generation
	Microscale	Quenching diameter ~ Mean-free path (non-equilibrium)	Fuel Cells Nano-particle reactors	Energy conversion
Device scale	Microscale	Smaller than conventional engine size	Micro-thrusters (PSU) Micro-gas turbine (MIT)	Micro-satellites Micro-air planes

Table 2
Typical length and time scales in micro-scale combustion.

Length scales	Time scales
Combustor scales, d	Flow residence time, t_{res}
Combustor structure scale, d_s	Characteristic combustion time, t_c
Flame thickness, δ_f	Diffusion time scale of gas-phase, $t_\alpha = d^2/\alpha$
Quenching diameter, $d_0 = n\delta_f$	Diffusion time scale of solid phase, $t_s = d_s^2/\alpha_s$
Mass diffusion length, δ_D	Time scale of heat loss, t_h
Thermal diffusion length, δ_α	Time scale of acoustic wave, t_a
Mean free path, λ	Ignition time scale, t_{ig}

and weak flame may exist. Several experiments and theoretical analyses have demonstrated these phenomena. This strong flame-wall coupling may significantly extend the flammability limit of the flame via the effect of excess enthalpy. As the wall temperature increases, the ignition time becomes shorter. Weak flames or flameless combustion can also be observed. When the ignition time approaches the flow residence time and the combustor size is close to the quenching limit, flame instability via flame extinction and reignition will occur. The wall temperature coupling with the flame is governed by the Biot number (the ratio of diffusion time scale to the convective and radiative heat loss time scale). At large Biot numbers, the wall temperature change is small. However, if the Biot number is not large, the wall temperature change will affect combustion in small scale. In addition, the wall temperature distribution is also affected by the Fourier number (the ratio of combustion time scale to the diffusion time scale in solid phase). If the Fourier number is very large and sufficiently high reactivity is maintained during the transient reactor response, the temperature distribution in the solid phase of the combustor can be considered quasi-steady-state.

When the combustor scale is further reduced, for example, the Knudsen number is larger than 0.01, the non-equilibrium transport effect (temperature and concentration slips on the wall surface) starts to play a role in affecting combustion. Several researchers have addressed these issues and found that the non-equilibrium effect strongly affects the ignition and extinction.

In micro-scale combustion, when the flow residence time becomes close to the characteristic combustion time, extinction will occur via incomplete combustion. In addition, the Lewis number effect (Le) will affect the thermal-diffusional instability. However, as shown in Table 3, different from conventional combustion in large scale, the thermal transport in the solid phase will significantly modify the effective Lewis number and the boundary of flame instability. Spinning combustion and pulsating combustion have been observed for mixture Lewis numbers close to or below unity. Furthermore, because of the wall confinement and high wall temperature, the acoustic waves also have a strong effect in micro-scale combustion. All these phenomena can be characterized by using the relative length and time scales. Otherwise, the unsteady temperature distribution in solid phase has to be considered.

1.3. Development and challenges of micro-power generators

Since the pioneering work of micro-gas turbines by Epstein et al. [15], many innovative micro-combustors for propulsion, power generation, chemical sensing, and heating have been designed or under development. The MIT gas turbine laboratory designed a micro-gas turbine generator capable of producing up to 50 W of electrical power by consuming 7 g of jet fuel per hour [14,15]. At UC Berkeley, Fernandez-Pello and coworkers [2] developed both mesoscale and micro-scale liquid hydrocarbon fueled rotary

engines to produce 30 W and a few milliwatts power, respectively, from micro-mechanical systems (MEMS). Honeywell [16], Georgia Tech [17], University of Michigan [18], and Aerodyne Research [19] developed free-piston engines with homogeneous charge compression ignition (HCCI). These engines have successfully produced 10–50 W power. However, due to the use of moving parts, friction loss, heat loss, leakage, sealing, and materials erosion led to low energy conversion efficiency. In addition, delivery, atomization, and ignition of liquid fuel are also difficult issues.

At the same time, digital monopropellant [13] and bipropellant micro-thrusters [12] were tested by using silicon based MEMS fabrication technologies. Unfortunately, the low thermal stability of silicon at high combustion temperatures (1600–1800 K) makes the engine lifetime very short. Recently, mesoscale and micro-scale thrusters using high melting temperature metals [4], ceramics [22], and quartz [23] have been developed. The combustion efficiency and flame stability is improved considerably. However, the wall heat loss is still large and the combustion efficiency remains low. In addition, problems such as liquid fuel injection, mixing, ignition, and cold start of the thruster are still the challenging issues. Particularly, fabrication technologies of ceramic micro-combustors remain difficult.

In order to improve thermal efficiency and combustion stability of microcombustors, various efforts have been paid on the optimization of thermal management and the use of catalyst. The concept of "excess enthalpy" has been widely adopted in the design of micro-combustor. The earliest work on excess enthalpy was carried by Weinberg and coworkers [24–26] and Takeno et al. [27]. The idea is to use Swill-roll type of burners (Fig. 2b) to recycle the burned gas energy to the unburned gas mixture. As a result, compared to the combustion without heat recirculation (enthalpy feedback), although the adiabatic flame temperature does not change, the maximum flame temperature at the reaction zone can be significantly higher than the maximum adiabatic flame temperature of combustion without heat recirculation, resulting in the so called "excess enthalpy" or superadiabatic combustion. With the increase of the maximum flame temperature, flame becomes stronger to resist flame quenching via heat loss and can burn much leaner than the standard flammability limits [28,29] (the lean or rich propagating limits of the one-dimensional, adiabatic, and unstretched planar flames). Based on this concept, different kinds of Swiss-roll microcombustors have been designed [30,31]. The experimental results showed that steady combustion and even flameless combustion can be achieved with mixture compositions beyond the standard flammability limits. By further raising the wall temperature, sub-millimeter combustion was also observed [4,14,20]. In order to further overcome the heat loss and/or radical loss induced

Table 3
Non-dimensional parameters vs. micro-scale combustion phenomena.

| Non-dimensional numbers	Phenomena
$d/\delta_f \sim O(10)$ or $d/d_0 \sim 1$	Flame extinction due to heat loss to the wall Wall catalytic/quenching effects, flame street & cells
$t_c/t_s = O(1)$, $d/d_0 \sim 1$	Flame-wall thermal coupling, multiple flame regime
$t_{ig}/t_{res} = O(1)$, $d/d_0 \sim 1$	Extinction and reignition instability, Weak flame Flameless combustion
$Bi = t_\alpha/t_h \gg 1$	Small wall temperature change
$Fo = t_c/t_s \gg 1$	Steady-state temperature distribution in solid phase
$Kn = \lambda/d > 0.01$	Non-equilibrium transport effect
$Da = t_{res}/t_c$ or $t_D/t_c \sim 1$	Flame extinction due to incomplete combustion
$Le = \delta_\alpha/\delta_D \sim 11$	Pulsating instability via flame structure coupling
$t_a/t_c = O(1)$	Acoustic instability
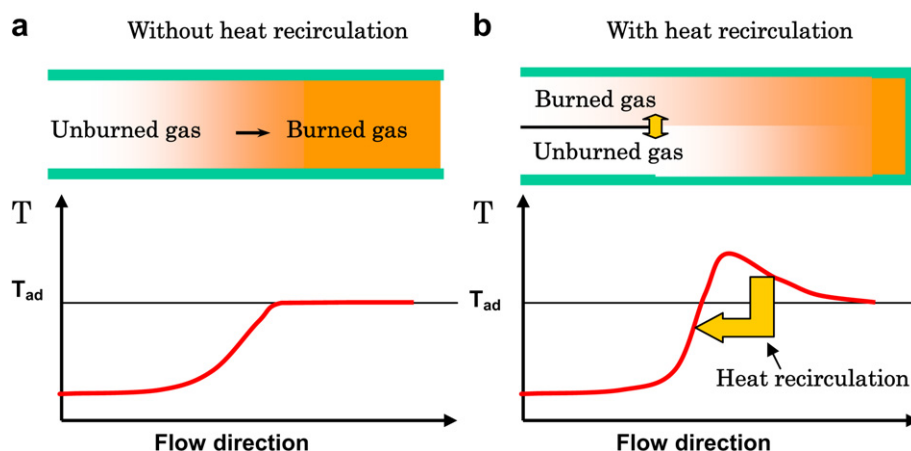
Fig. 2. Temperature distributions of the swirling burner and heat recirculation burner.

combustion, meso and micro-scale catalytic reactors have also been developed [23,32–34]. Nevertheless, a successful design of micro-combustor with a high energy conversion efficiency needs fundamental understanding of the effects of heat loss, radical loss, excess enthalpy, wall-flame thermal/chemical coupling, fuel-air mixing, liquid fuel vaporization, flow field, and non-equilibrium transport on ignition, burning rate, flame temperature, and flame stabilization.

1.4. Challenges in fundamental research of micro-scale combustion

As the combustor size is reduced, the combustor surface to volume ratio increases dramatically, creating strong thermal and chemical couplings between flame, flame–solid interface, and combustor structure. In order to understand the effect of heat loss on the flame extinction in a channel, Daou et al. [35–37] studied the effect of flow velocity, Lewis number, and channel width on the flame propagation limit. The results showed that the near wall-flame quenching and flame curvature plays an important role in flame extinction. This study was extended by Ju et al. [38] to include the heat transfer in solid phase and the coupling of flames. The results demonstrated that the flame-wall thermal coupling significantly extends the quenching limit and led to a new flame regime. To examine the effect of excess enthalpy on the flame stabilization in a Swiss-roll type burner, Ronney [28] and Ju et al. [29] investigated independently the impacts of heat recirculation from the burned gas to the unburned mixture (Fig. 2) by using the counter propagating flames in two parallel channels. The results showed that the flame location and flame temperature can be affected by heat recirculation. Sub-limit flames can be established when the flow velocity is increased. The results showed that the flammability limit can be significantly extended by burned gas heat recirculation. The theoretical results confirmed the experimental observation by Weinberg et al. [24]. To further understand the effects of flame-wall thermal coupling on flame propagation in small scale combustion, theoretical and experimental studies of flame propagation in a mesoscale channel and near a hot wall with flame-wall interaction were carried out by Ju et al. [39,40], Maruta et al. [41,42], and Leach et al. [43]. For the first time, both the theory and the experiments demonstrated that the flame-wall interaction created a new flame regime, the weak flame regime, which significantly extended the conventional flammability limit to allow larger heat losses from the flame. On the other hand, various flame instabilities, extinction and reignition instability [41,44–46], spinning instability [47], cellular instability [48], and

flame streets [49] were observed in mesoscale combustion via flame-wall interaction. A computational work was carried out to reproduce the observed reignition and pulsating flame instabilities by Buckmaster and coworkers [50]. Direct numerical simulations of multi-dimensional Swiss-roll were carried out by Ronney and coworkers [51]. For micro-scale combustion, non-equilibrium effects via temperature and concentration slips on the wall and radical quenching were recently studied by Ju and coworkers [52,53] and Vlachos and coworkers [54]. These quantitative and interesting findings significantly advanced our understanding of the physical and chemical processes in micro-scale combustion and had a great impact on the design of efficient micro-scale combustors.

1.5. Focus of previous and the present reviews

Several reviews [1,2,6,15,55–59] on the progress of technological development in micro-power generation have been made since 1999. Epstein et al. [15,57] presented a work in progress review on MIT MEMS-based gas turbine engines and rocket engines and discussed the technology challenges and the future development of power MEMS. The review focused on the millimeter-size gas turbine engine design, integration, manufacturing, materials, fluid mechanics, cycles, and applications, and economics. Whitehead et al. [55] reviewed the application of a self-pressurizing hydrogen peroxide monopropellant and bipropellant propulsion systems for maneuvering tests of a 25 kg micro-satellite prototype. Ohadi et al. [59] discussed the application of high temperature heat exchanger for heat recovery in microcombustors. Janson [56] gave a review of fabrication and development of micro-propulsion systems with special attention on a prototype micro-power device based on the concept of a thermophotovoltaic (TPV) system of generating electricity. Recently, Dunn-Rankin et al. [1] used fuel cells, model airplane engines, and hummingbird metabolism as examples and reviewed the concepts of electrochemical, thermochemical, and biochemical approaches to a small scale personal power, as well as their technological and physical challenges and limitations. Emphases were made, particularly on fuel cells and metabolic processes of biological energy converters. Chia et al. [58] briefly discussed micro-thermoelectric power generators, micro-rotary engine, and micro-gas turbine engines, with more focus on micro-fuel cells. However, none of the above reviews have emphasized micro-scale combustion processes, particularly on the fundamentals of micro-scale combustion.

Table 4
Meso and micro-scale thrusters and power generators using gas-phase combustion.

Micro-thrusters & engines	Materials	Size/length scale	Thrust, Power	Propellant	Pressure	Challenges
Digital rocket chip (Caltech)	Silicon	0.5 mm^3	0.1 N 100W	$C_6H_3N_3O_8Pb$	~1atm	Large heat loss d/δ_f ~O (10)
Bi-propellant (MIT)	Silicon	705 mm^3	1N, 750 W	O_2/CH_4	12.3 atm	Low flame temperature and small $Da = t_{res}/t_c$
Staged thruster (PU)	Quarz	2000 mm^3	~500 W	Methanol, butene/air	2 atm	Strong wall-flame coupling t_c/t_s = O (1)
Vortex flow combustor (PSU)	Inconel	10–50 mm^3	~500 W	methane/oxygen	1 atm	Small $Da = t_{res}/t_c$
Electrolytic thruster (PSU)	ceramic	322 mm^3	197 mN	HAN	1 atm	Cracking, heat loss, d/δ_f ~ O (10)
Non-premixed combustor (UIUC)	Quartz, alumina	0.1–2 mm	10–50 W	H_2, methane	1 atm	Thermal, radical quenching $Da = t_{res}/t_c$ ~ 1
Micro-gas turbine (MIT, Tohoku)	Silicon	60–200 mm^3	50W	Jet fuel	1 atm	Friction, sealing
Rotary engine (UCB)	Silicon, Stainless	1–1000 mm^3	0.01–30 W	Hydrocarbon fuel	1atm	Fuel delivery, friction, sealing, Da = t_{res}/t_c ~ 1
Free-piston engine (Honeywell, UM, Georgia Tech)	Stainless	1 cm^3	~10W	heptane, butane, Jet fuel	1–5 atm	Mass loss, sealing, ignition, t_{ig}/t_{res} = O (1)

Two reviews on micro-scale power generation using combustion were made by Fernandez-Pello [2] and Chigier et al. [6]. The reviews presented a detailed summary of the opportunities, technological progresses, and operation issues of micro-power generators using thermochemical processes such as combustion and catalytic reaction. The reviews also provided an analysis of challenges such as liquid fuel injection, fluid–wall interaction, fuel-air mixing, thermal quenching, catalytic combustion, and micro-fabrication. Since then, a number of important progresses have been made in achieving micro-scale combustion and propulsion. Furthermore, significant progresses have been made in fundamental studies of micro-scale combustion. Compared to 2003, today we have a much better fundamental understanding of micro-scale combustion such as heat recirculation, flame-wall thermal and kinetic couplings, new flame regimes, fuel/oxidizer mixing, flame instabilities, and non-equilibrium transport. After one decade of research and development, the study of micro-scale combustion is moving into new directions. Therefore, it is an appropriate time to make a comprehensive review of micro-scale combustion. The goal of this review is to not so much to describe details of the tests and designs of micro-power generations systems, but rather to present an overview of the development of micro-power generators by focusing more on the advance in fundamental understanding of micro-scale combustion, so that the knowledge which we have learned in micro-scale combustion can be applied in other new systems involving small scale transport and chemical reaction to achieve improved energy conversion efficiency and reduced combustion emissions.

2. Meso and micro-scale combustors

2.1. Micro-thrusters

A micro-combustor has a number of advantages over a conventional thruster to deliver low thrust (~1 mN) and low impulse bit (~10^{-5} Ns) for precise attitude and positioning control of micro-satellites (10–100 kg) [10]. Various micro-fabrication technologies such as stereolithography [60], low temperature co-fired ceramic taping (LTCC) [10,61] and silicon based microelectromechanical system (MEMS) fabrication techniques [20] have been used for the design of micro-thrusters (Table 4). As the combustor scale decreases, igniting the propellants and establishing sustainable combustion become more challenging because of the increased wall heat and radical losses. In addition, as the flame temperature increases, increase of materials strength at high temperature and elevated pressure is another difficult issue. To overcome these challenges, in last ten years, many kinds of micro-thrusters with different combustor length scales, materials, propellants, and ignition methods have been designed and tested successfully [10,13,20]. In this and the following sections, we focus our discussions on gas-phase micro-thrusters and power generators (Table 4). Catalytic reactors and catalytic micro-thrusters [62] will be discussed in Section 2.3.

The DARPA-funded MEMS Digital Micro-Propulsion "rocket chip" [13] (Fig. 3) was developed at Caltech in collaboration with TRW and the Aerospace Corporation. The goal was to demonstrate and characterize different types of MEMS micro-thrusters, and to test MEMS micro-thrusters in space for micro-spacecraft. The micro-thruster array was made by the silicon and glass by using the MEMS micro-fabrication technology. Each chip consisted of a three-layer sandwich of silicon and glass, and was mounted in a standard 24-pin ceramic dual-inline electronics package. The top layer had nozzles wet etched. In the middle layer, the combustion chamber was etched on photosensitive glass. The bottom layer was patterned with polysilicon ignitors with direct inter-connection circuits (~50 W). A prototype thruster contained 15 individual thrusters in the central 3 by 5 array. Each chamber has an approximate volume of 0.5 mm^3 and is filled with lead styphnate ($C_6H_3N_3O_8Pb$) as the solid propellant. Electric resistors were used in each thruster to initiate combustion of the lead styphnate fuel. Each thruster cell produced 0.1 milli-Newton-seconds of impulse, 0.1 N thrust, and about 100 W of mechanical power. A successful suborbital test flight of these MEMS devices were also conducted. A similar type of micro-solid propellant thruster was fabricated by Honeywell Technology Center [63]. The thruster array consisted of 512 × 512 cells on a 1.3 inch × 1.3 inch silicon die. Each micro-solid rocket cell with size of 51 μm × 51 μm could work individually or together. Nitrocellulose mixtures were used as the main propellant. Each rocket cell was ignited by using lead styphnate and produced an impulse of 0.5–20 μNs. However, the small size and low
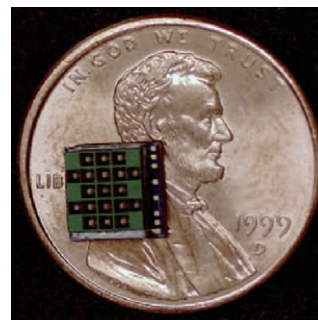

Fig. 3. The TRW/Aerospace/Caltech MEMS Digital Micro-Propulsion "rocket chip" [13].

pressure of the thruster caused a large heat loss ($d/\delta_f \sim O(10)$) and limited its propulsion efficiency.

In order to improve the performance of micro-rocket, a high pressure bipropellant rocket engine using oxygen and methane as the propellants was developed at MIT [12] (Fig. 4). The thruster was manufactured by fusion bonding on a stack of six individually etched single crystal silicon wafers. The thruster chip was 18 mm long, 13.5 mm wide, and 2.9 mm thick, and weighed 1.2 g. The chamber volume was approximately 100 mm^3 [12] and the chamber pressure reached 12.3 atm. The thruster test showed that it was able to produce 1N thrust and specific impulse of 300s, and delivered a thrust power of 750 W. The characteristic exhaust velocity (c*) of the rocket reached the predicted ideal rocket engine value within 5−15%. Again, the use of silicon greatly limited the maximum flame temperature and resulted in a small reaction Damkohler number ($Da = t_{res}/t_c \sim 1$).

To achieve better chemical and thermal sustainability, several meso and micro-scale thrusters with high melting temperature materials have also been fabricated. By using quartz and ceramic tubes, a two-staged mesoscale combustor consisting of a sub-millimeter scale catalytic reactor and a mesoscale quartz main combustor (10 mm in diameter) was designed at Princeton University (Fig. 5) [23]. The catalytic microtube with 1-butene and airflow was used to produce active radicals and recirculation flow for the stabilization of the flame in main combustor. The main combustor was a nested doll structure to enable heat recirculation using liquid fuels. The performance of the mesoscale combustor was tested for both gaseous (methane) and liquid fuels (ethanol), resulting in stable combustion for both cases. The results showed that this catalytic reaction significantly extended the lean and rich flammability limits of fuels in the main combustor and sustained a reaction at significantly lower flow rates. The difficult issues were the lifetime of the catalytic reactor with nickel catalysts and the strong flame-wall thermal coupling.

By using inconel (melting point 1700 K) with an electro-discharge machining technique, the Pennsylvania State University group led by Yetter [60] developed a mesoscale vortex flow combustor to establish non-premixed combustion. The combustor volume was as small as 10.6 mm^3. Hydrogen and hydrocarbon fuels (e.g. methane and propane) were employed and the mixture was ignited by a spark igniter located at the center of the combustor head end. As shown in Fig. 6, fuel is injected perpendicularly to the tangentially injected oxidizer to increase the flame stability and mixing. The combustion products also exit tangentially from the exit, forming a center recirculation zone and enhancing the mixing between the burned products with the unburned mixture. In addition, due to the swirling flow, the centrifugal force drives the cold and unburned mixture toward the wall, and the hot burned gas
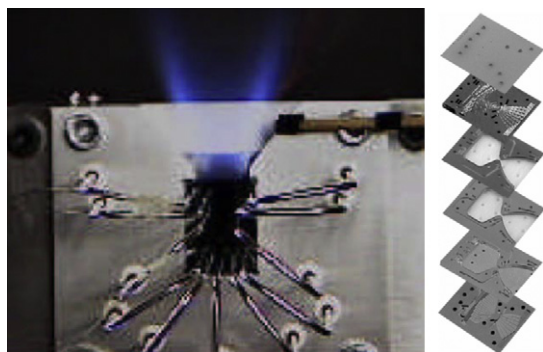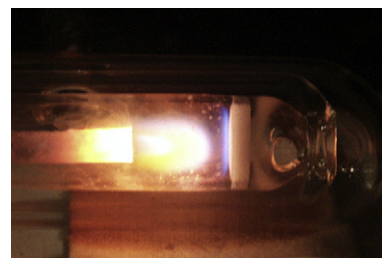

Fig. 5. A two-staged mesoscale combustor consisting of a sub-millimeter scale catalytic reactor to produce radicals and recirculating flow for a mesoscale, dual shelled main combustor [23].

to the center. As a result, the swirling combustion is able to reduce heat loss to the wall and enables combustion at much higher flame temperatures than the melting temperature of the structure. The combustion efficiency and flame stability was studied both numerical and experimentally for hydrocarbon-air mixtures. Fig. 6 (bottom left) shows the front view of a propane/air flame with an overall equivalence ratio of 0.8. The flame exhibits a luminous blue ring with a non luminous core of burned products (1650 K). The near wall quenching distance is 0.5 mm. Fig. 6 also shows the flame structure of methane/oxygen-enriched-air mixture in a 49.1 mm^3 combustor with an overall equivalence ratio of 0.3 (bottom right). Compared with the propane/air flame, the oxygen enrichment enhances the flame stability and results in a stronger luminous flame zone. The combustor core temperature increases to 2000 K, reaching combustion efficiency more than 85%.

However, when the combustor size further decreases, a swirling flow becomes difficult because of the strong viscous loss and low angular momentum. In addition, the quenching distance (0.5 mm) reported in the swirling flow burner makes it impossible to
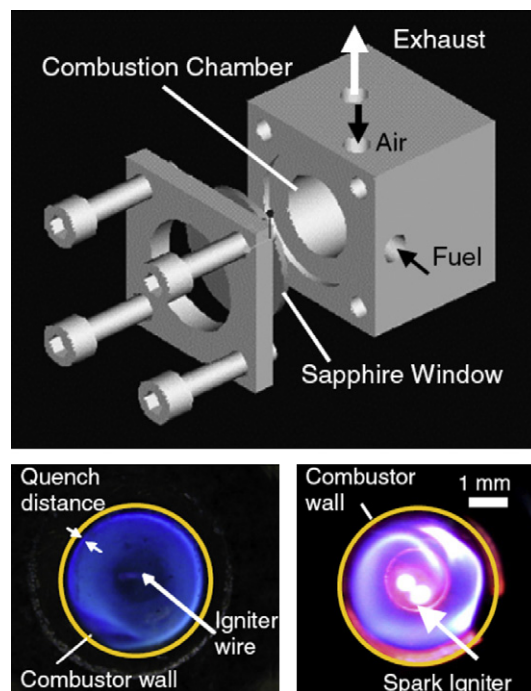

Fig. 6. Top: schematic of mesoscale vortex flow combustor, Bottom left: flame structure of propane/air with an overall equivalence ratio of 0.8 in the 124 mm^3 combustor, Bottom right: flame structure of methane/oxygen-enriched air combustion in the 49.1 mm^3 combustor with an overall equivalence ratio of 0.3 (50% N$_2$ and 50% O$_2$ by volume in the oxidizer stream) [60].

Fig. 4. A bipropellant micro-thruster developed at MIT [12].

manufacture a sub-millimeter thruster. As such, in order to achieve micro-scale combustion, the wall temperature and high temperature stability have to be increased. Instead of using silicon, ceramic materials have been used to develop micro-combustors. The LTCC fabrication method was employed for the fabrication of micro-thrusters [10,22,61]. In LTCC, ceramic structures are made from alumina, glass, and binders in a tape form. Yetter et al. [64] built an alumina micro-thruster using ceramic stereolithography and demonstrated hydrogen/air combustion at a chamber pressure of approximately 8 atm. Miesse et al. also developed an alumina micro-burner [48]. By using LTCC tape technology [65], sub-milli-meter scale diffusion flame burners and liquid monopropellant micro-thrusters with electrolytic ignition were fabricated by Yetter and coworkers [10].

The design of the electrolytic micro-thruster consisted of three-layers (Fig. 7) [10]. The electrodes on the inner surfaces of layer 1 and layer 3 provide direct contacts for electrolytic reaction of a hydroxylammonium nitrate (HAN, $NH_3OH^+NO_3^-$) based liquid propellant to occur in the thruster combustion chamber. The thruster combustion chamber and nozzle were fabricated on layer 2 using micro punches. Vias were punched on layers 2 and 3 and filled with conductor paste. The vias and wiring patterns on layer 1 and layer 3 provided electric connections between the electrodes and the electric contacts on the outer surface of layer 3. LTCC tapes were prelaminated and fired to obtain required thickness layer. The thickness for layer 1 and 3 are approximately 386 μm after cofiring, while the thrust chamber is 290 μm thick. The electrode and wiring patterns were screen printed on layer 1 and 3 with silver cofireable ink (Dupont 6141) and dried in a 60 °C oven for 15 min. Four thrusters were designed on each 3″ by 5″ LTCC tape stack and individual thrusters were cut out before sintering. The dimensions of the whole thruster chip are approximately 25.4 mm wide, 12.7 mm in height, and 1 mm thick. The volume of the internal combustion chamber is 0.82 mm³. The silver electrodes cover the entire top and bottom surfaces of the chamber. The half angle of the nozzle contraction is 54° and 15° for the nozzle expansion. HAN-based liquid monopropellant (RK315A) was filled into the thrust chamber. A DC power supply working at constant voltage mode provided the current flow for ignition in the electrolytic process. A micro force transducer (PCI, U209C11) with a resolution of 0.0001 N was used to measure the thrust.

Fig. 8 shows the thrust and current profiles during the ignition burst. The voltage applied was 45 V and a longer ignition delay of ∼2.255 s was recorded. The clipping of the output current indicates that the reactivity of the propellant becomes so high that the resistivity through ionic flow in the liquid propellant becomes negligible. The impedance across the liquid propellant becomes so small that the circuit draws all the maximum current the power supply is able to provide (50 A). The thrust history shows
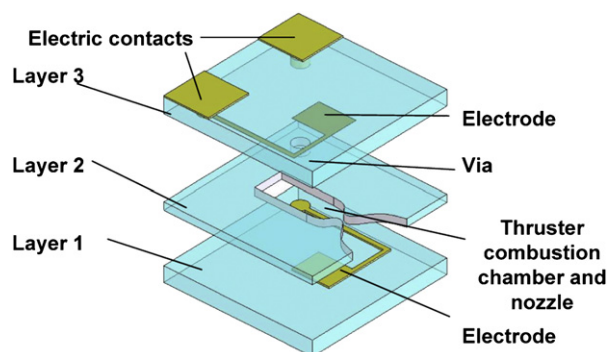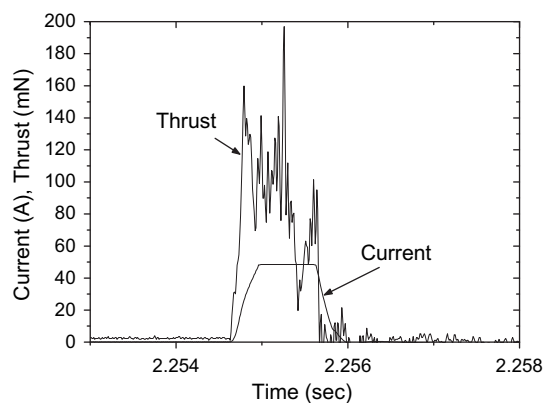

Fig. 8. The evolution of the measured force and the corresponding current readings during the ignition burst [10].

a maximum thrust of 197 mN for the currently designed HAN-based liquid monopropellant micro-thruster. The impulse is 3.1×10^{-3} Ns. The energy input during the ignition process is 14.7 J. Experiments with different ignition voltage (power) and propellants were also conducted. Under rapid ignition conditions, cracking of the combustor wall was observed.

To examine the effect of materials thermal diffusivity and surface reactivity on flame quenching limits and combustor thermal stability, Miesse et al. [20] compared the quenching lengths in a non-premixed micro-combustor made of quartz, cordierite, alumina, and stainless steel. The results showed that at low temperatures (∼500 °C), the quenching lengths (∼2.5 mm) were relatively independent on wall materials when the thermal quenching was a dominant mode. However, at higher surface temperatures (∼1000 °C), it was reported that the quenching length varied strongly with the wall materials. The results showed that cordierite and quartz respectively had the smallest (100 μm) and the largest (1.8 mm) quenching distance. This result indicates that at higher wall temperatures, the radical quenching played an important role in flame quenching. Inconel have been used to vary the thermal diffusivity and surface properties to extend the flame quenching limits and combustor temperature limit, and to reduce the surface radical extinction.

As such, the current micro-thruster manufacturing technology is still facing many challenges. New micro-fabrication technologies using high melting ceramic materials to improve combustor thermal stability at elevated pressures are needed. New ignition methods which can ignite liquid and solid propellants with minimal impacts on combustor structures are necessary. Fundamental understanding of the mechanisms of thermal and kinetic flame quenching in micro-combustion is needed.

2.2. Micro internal combustion engines

The high energy density of liquid fuels offers great opportunities to develop efficient internal combustion engines to replace batteries for power and electricity generation for micro-air planes, micro-pumps, MEMS, and drug delivery systems. Several innovative designs of micro-engines using gas turbines, rotary engines, and piston engines have been developed.

The MIT gas turbine research laboratory developed several advanced gas turbine engines for power generation by using the silicon based micro-fabrication technology [14,15,66]. Epstein et al. [15] reported the design of a micro-gas turbine generator capable of producing up to 50 W of electrical power by consuming 7 g of jet fuel per hour. Later, stable hydrogen combustion in a micro-
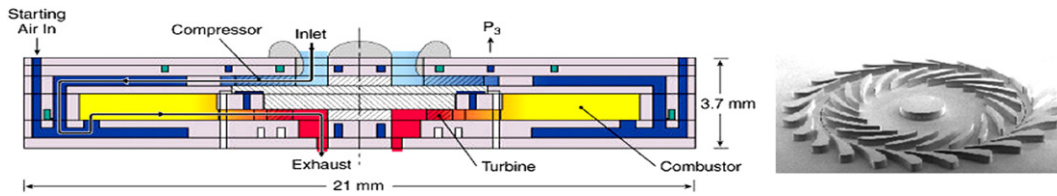

Fig. 7. Schematic of LTCC electrolytic micro-thruster design [10].

Fig. 9. Schematic of the MIT micro-gas turbine (left) and the turbine blades (right) [66].

combustor of 66 mm^3 for gas turbine engines was demonstrated [67]. The exhaust gas temperature reached 1800 K. This combustor was integrated with a micro-gas turbine engine (static structure and combustor) by Mehra et al. [14]. Test of the integrated micro system demonstrated that the system was able to deliver 2 GW/m^3.

A schematic of the one stage, single shaft micro-gas turbine engine and the turbine blade are shown in Fig. 9 [15,66,67]. The system includes a co-axial compressor/turbine unit, air inlet, fuel injectors, a combustion chamber, and an electrical generator. Air enters the turbine engine axially and makes right angle turn into the centrifugal compressor. At a tip speed of 500 m/s, the compressor's adiabatic pressure ratio is 4. Fuel is injected through a circular array of holes with diameters between 60 μm and 224 μm, and mixes with the compressed air. The flow enters the combustor through an axial inlet and is burned in a combustion chamber of 195 mm^3. The burned gas passes the turbine static vanes to raise the combustor pressure through a choked flow and is impinged on the spinning turbine rotor for power extraction. With a 4 mm rotor diameter and airfoil height of 200 μm, the turbine rotation speed has reached 1.3 million rpm with sustainable combustion of hydrogen and producing 10−20 W. Ethylene-air combustion in the static structure showed that stable combustion was obtained with exhaust gas temperatures higher than 1600 K, combustion efficiency up to 80%, and the maximum power density of 500 MW/m^3. For propane-air mixtures, due to the longer ignition delay time, combustion was obtained only with a maximum power density of 140 MW/m^3. Therefore, one of the main challenges is to achieve sustainable combustion with high combustion efficiency for liquid phase hydrocarbon fuels such as jet fuels. Other challenges include materials thermal stability, thermal isolation and turbine cooling, bearing wear at high turbine speeds, and the increase of the compression ratio of compressor. As a preliminary effort to achieve sustainable combustion for hydrocarbon fuels, a catalytic micro-combustor with platinum-coated nickel foam inserts was designed and tested for propane-air mixtures [68]. An overall efficiency of 40% was achieved.

A research group at Tohoku University led by Tanaka and Esashi [69,70] in cooperation with IHI Corporation has succeeded in the demonstration of the world's smallest class gas turbine engine

(Fig. 10). The outer size of the engine is about 10 cm in diameter and 15 cm in length. It includes a compressor of 16 mm diameter, a turbine of 17.4 mm diameter, an annular combustor, and a dummy electromagnetic generator. The impellers are connected by a shaft of 8 mm diameter made by a single piece of Inconel. The total weight of the rotor is approximately 37 g. The combustor is a swirl flow type, and the flame is stabilized at the swirler step downstream. The Brayton cycle was established at 360000 rpm with the combustor temperature between 800 and 900 °C. The success of the miniature of gas turbine engines opens applications for mobile robots and personal vehicles.

At UC Berkeley, Fernandez-Pello and coworkers [71–74] have developed several liquid hydrocarbon fueled rotary engines. Two different sizes of rotary engines, a mesoscale rotary engine with an output about 30 W and a micro-rotary engine with an output of a few milliwatt were designed (Fig. 11). The Rotary Wankel engine was invented by an engineer Felix Wankel [75] in 1957. Wankel engine uses a rotating motion of a triangular rotor housed in an oval-like chamber to convert thermal energy into mechanical energy without the conventional reciprocating pistons. This compact engine design makes it possible to deliver higher power per unit weight than piston engines. The engine has been successfully used by Mazda. The biggest challenge is the sealing between combustion chambers and errosions of the rotor at high rpm. The UCB's mesoscale rotary engine is EDM-fabricated from steel, with an epitrochoidal-shaped housing chamber (12.5 mm) and a rotor (10 mm). Tests have been conducted with different mesoscale rotary engine designs to examine the effects of sealing, ignition, and thermal management on efficiency by using hydrogen/air mixtures. Ignition is initiated by employing electrical spark and catalytic glow plug. An net power output of up to 3.7 W at 9000 rpm has been obtained with a thermal efficiency around 0.2% [71]. The major reasons for such a low efficiency of the engine are the low compression ratio, leakage between the rotor apex tip seals and the housing and over the rotor faces [2]. In spite of great efforts, improvements of sealing and compression ratio remain as difficult issues to achieve a dramatic increase of thermal efficiency.

As an effort to improve the engine design and efficiency for micro-mechanical power devices, micro−rotary engines were also
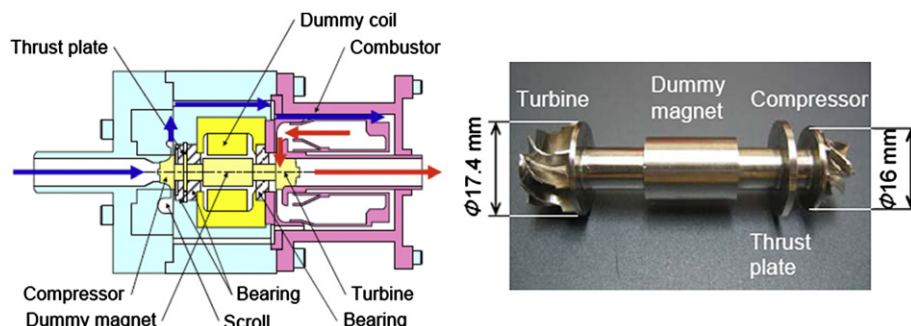

Fig. 10. Left: Schematic structure of the miniature gas turbine engine. Right: Rotor with compressor and turbine impellers [70].
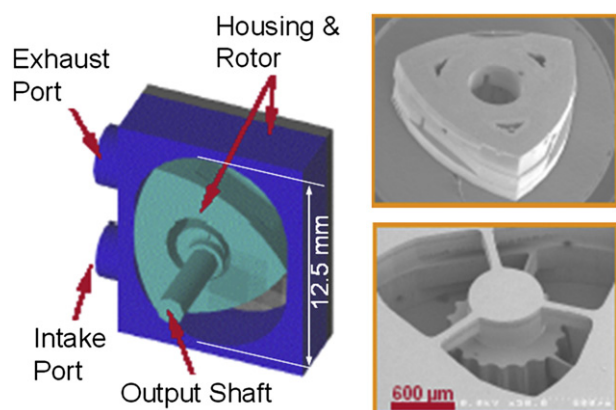
Fig. 11. The UCB mesoscale rotary engine (left) and micro-rotary engine (right) [2].

developed by the UCB group by using silicon based MEMS fabrication techniques. The project is to produce 10–100 mW of mechanical power with an engine chamber size below 1 mm^3 [2,72,74]. Two kinds of MEMS-based micro-engines were fabricated, one made of SiC with a 2.3 mm rotor and another of Si with a 1 mm rotor. The housing spur gear and rotor through holes have been fabricated using a self-masking method to produce structures of 150 μm. The sealing, lubricity, and toughness of the fabricated engines were tested by using compressed air. Unfortunately, issues still remain with the fabrication process, fuel delivering valves, sealing, materials, friction, fuel vaporization, ignition, combustion, thermal management, and efficiency to achieve the design targets.

To resolve the serious sealing issues in rotary engine, a mesoscale free-piston "knock" engine using homogeneous charge compression ignition (HCCI) of hydrocarbon fuels (heptane, butane, and diesel) is being developed at Honeywell [16,76] in collaborating with University of Minnesota (Fig. 12). The goal is to produce 10 W of electrical power from 1 cm^3 packaged volumes. Test experiments showed that HCCI combustion of heptane at equivalence ratios of $\Phi = 0.69$ and 0.25 was successful and that HCCI was even possible in spaces 3 mm diameter and 0.3 mm long. However, in order to achieve reliable auto-ignition of the fuel and to develop these power densities, the engine has to operate at kilohertz frequencies, resulting in strict requirement of short ignition delay times. Theoretically, these high operating frequencies yield nearly adiabatic compression, ignition, and expansion without allowing flame propagation, leading to a higher overall thermal efficiency. Unfortunately, sealing problems and mass losses in the piston/cylinder appeared to have limited the fuel efficiency of the engine and caused a distortion of the piston-time path during the expansion stroke. Moreover, materials erosion also limited the lifetime of the device.

A free-piston/cylinder direct electrical power generator based on a ferromagnetic piston oscillating in a magnetic field is developed at Georgia Tech [17] (Fig. 13). The piston is driven by the alternated combustion of a hydrocarbon fuel/air mixture at each end of the cylinder. The magnetic field is produced by permanent magnetic arrays that surround the cylinder assembly. A power generator with a displacement of 4.3 cm stroke and 13.4 cm^3 has been developed. To date, 12 W of electrical power has been extracted. Sealing and heat loss problems in the piston cylinder and combustion chamber remain to be the limiting issues to improve efficiency.

At University of Michigan, a rotationally oscillating free-piston, micro internal combustion swing engine (MICSE) [18,77] was developed. The swing-arm creates four distinct combustion chambers in a single base structure, leading to more efficient use of

both chamber space and system mass for power generation than linear free-piston engines (Fig. 14). Since timing is based on the swing-arm position, the system automatically adjusts to changes in external load, ambient temperature, and equivalence ratio. The engine is designed to operate on a four-stroke Otto cycle and the mechanical-to-electrical power conversion is via a shaft-coupled inductive alternator outside the combustion chamber. The design goal is to produce 20 W of electrical power by using a liquid hydrocarbon fuel (e.g. butane) at a size of a few cubic centimeters. However, although the rotating swing-arm also produces less vibration and provides simple motion for direct electrical power generation than a linearly translating piston, the production of mechanical torque is inefficient [3]. In addition, the shortening of the mixing and combustion time may cause the decrease of thermal efficiency. A recent numerical simulation [77] showed that the minimum combustion time in such small scale engines is governed by the mean turbulent kinetic energy. The results also suggested that the turbulence induced by the motion of the moving component can enhance in-chamber turbulence and therefore reduce combustion time.

A Miniature Internal Combustion Engine (MICE) generator consisting of a miniature linear engine coupled with a linear electric alternator, is developed at Aerodyne Research [19] to address the need for light weight portable power. The MICE generator is a two-stroke, free-piston engine with glow plug assisted ignition and air pre-heating. The kinetic energy of piston motion is stored in a spring and the engine operates at the resonant frequency of the spring-mass system with very low frictional losses. It uses HCCI combustion to achieve a wide fuel capability, including low volatility fuels such as JP-8 and diesel. Extensive testing has been performed on a nominal 500 W MICE generator using propane and Jet-A fuels. Test data showed the wide range of scavenging ratio and equivalence ratio conditions under which HCCI combustion was achieved. An alternator efficiency of 94% and a MICE two-stroke engine thermal efficiency of 16% on Jet-A fuel were achieved. Continuous efforts are needed to further improve the overall engine efficiency.

2.3. Microreactors

Another conventional approach for micro-power generation is combination of micro-reactors and energy conversion devices, such as thermoelectric, thermophotovoltaic and piezoelectric devices. Micro-power generation by micro-reactor is advantageous since it is free from friction losses by moving parts. Thermal management is
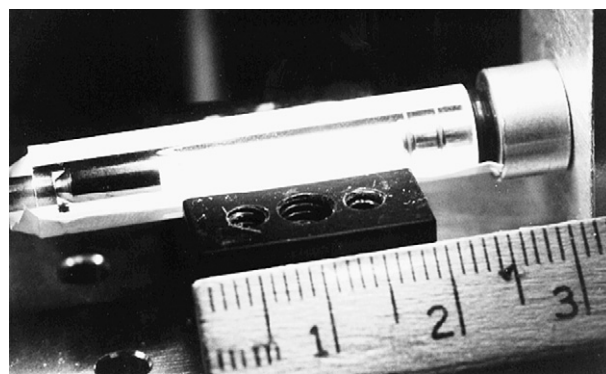

Fig. 12. The mesoscale free-piston "knock" engine using homogeneous charge compression ignition (HCCI) [76]. The piston is on the left and the end plug is on the right. The piston consists of a machined 3 mm steel gauge pin and the cylinder is a Pyrex tube having a nominal inner diameter of 3 mm.

Fig. 13. Free-piston/cylinder direct electrical power generator based on a ferromagnetic piston oscillating in a magnetic field [17]. The piston is on the left and the end plug is on the right. The piston consists of a machined 3 mm steel gauge pin and the cylinder is a Pyrex tube having a nominal inner diameter of 3 mm.
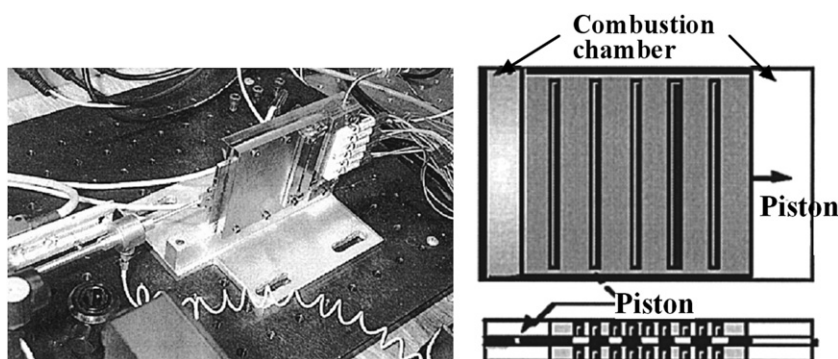
adopted for sustaining stable combustion at extremely small scale reactors. Heat recirculation or use of catalysis is common and effective thermal managements.

As a pioneer work, a combination of the Swiss-roll burner and the thermoelectric devices were attempted at the USC combustion physics laboratory. To maximize the system efficiency by minimizing heat loss from the system to the ambient, they proposed a toroidal three-dimensional configuration based on the original 2-D Swiss-roll burner which was originally suggested by Weinberg [25,78]. Fig. 15 shows a schematic of the U-shaped heat recirculation channel, configurations of 2-D Swiss-roll burner, macro- and mesoscale toroidal 3-D burners in which the heat generated by combustion is effectively returned to the incoming fresh mixture through channel dividing walls. For higher thermal efficiencies, a number of thermoelectric devices are embedded in all the diving walls of 2-D and 3-D burners [79] by developing a special fabrication technique. Despite the great efforts, fabrication of thermoelectric devices with high figure-of-merit in such complicated multi-dimensional configuration remains a difficult task. The maximum efficiency of energy conversion by thermoelectric devices that operate as part of the heat recycle in heat recycling burner is examined theoretically [80]. The 2-D Swiss-roll burner was successfully applied to hydrocarbon-fueled, thermally self-sustained, and single-chambered micro-SOFC by the same USC group [9] (Details not shown here). Flame dynamics in various combustors with heat recirculation [28] is discussed in detail in Section 3.1.2.

The use of catalysis is also an effective and promising approach for microreactors. By taking the advantage of high energy density of liquid hydrocarbon fuels, mesoscale catalytic combustors using electrosprayed liquid hydrocarbons to be coupled with energy conversion modules are developed by the group of Yale Center for Combustion Studies [33,81]. For dispersion of heavy liquid hydrocarbon fuels, thermal decomposition by hot surface is not always the best way, particularly for micro-scale application due to the fouling and plugging of the small channel. Thus, electrospray atomization, which relies on electric charging of liquid fuel with sufficient electric conductivity, was employed. Liquid fuel with sufficient electric conductivity is fed through a small nozzle, maintained at a few kilovolts relative to a ground electrode positioned at the downstream. Under the electric field, leading edge of the liquid jet at the outlet of the nozzle breaks up toward the downstream and atomized into a spray of fine, charged droplets. The electrospray is characterized by quasi-monodispersity of the droplets within the order of the 10% deviation from the relative standard droplet size and Coulombic repulsion of the charged droplets, which leads to the prevention of droplet coalescence and mixing enhancements with oxidizer stream. Fig. 16 shows a catalytic mesoscale burner [33] and the schematic of an electrospray injection system with catalytic screens which acts as a uniform and stable high temperature source for energy conversion modules [81]. After catalyst optimization through varying Pd/Pt ratio, and Ce and Ni doping for larger sulfur resistance, JP8 at flow rates of 10 ml/h which corresponds to 100 W (~6.7 MW/m^3 of volumetric power density at 15 cc of combustor volume) was achieved by the developed system. For higher energy density, miniaturization is conducted through the combination of microfabricated multiplexed electrospray system and catalytic meshes (See Fig. 17). And
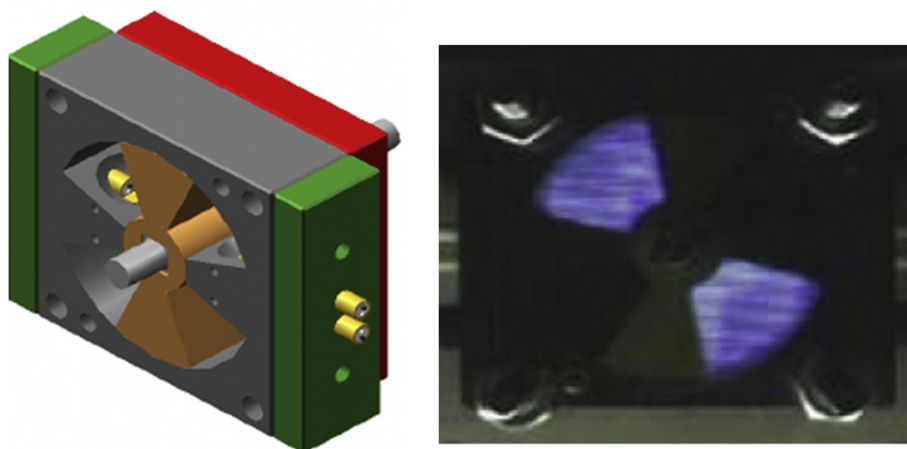

Fig. 14. Mesoscale internal combustion swing engine (MICSE) [18] showing non-cylindrical combustion chambers (*left*) and combustion visualization (*right*).
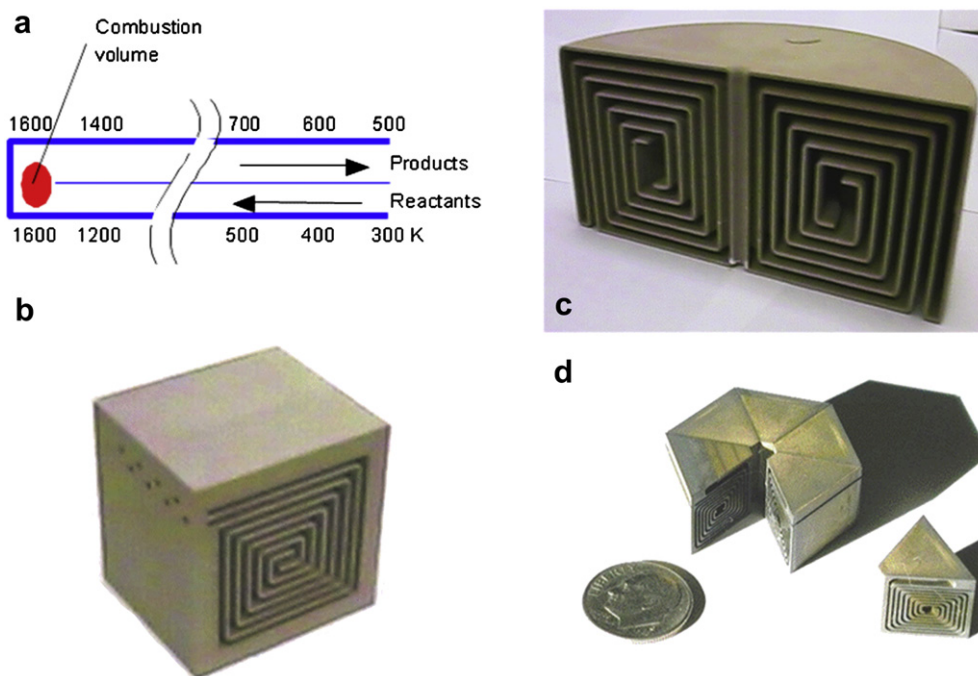
Fig. 15. Scheme of heat recirculating burners and burner prototypes fabricated at USC combustion physics laboratory [79]. (a) concept of heat recirculation in U-shaped channel, (b) 2-D Swiss-roll burner, (c) Macro- and (d) mesoscale, toroidal 3-D burners. Both macro- and mesoscale versions attained self-stabilized combustion.

it is established that the same order of thermal power at one or more order smaller combustor in overall volume which corresponds to total energy density up to 270 MW/m^3 [82]. This value is comparable to those of conventional macro-scale gas turbine engines operated at elevated pressures.

Disk-shaped Swiss-roll microcombustors for general purpose heat sources were developed by Tohoku group [83,84] as shown in Fig. 18. Several scales of prototype combustors of which outer diameters of 64, 45, 26 and 20 mm, and channel widths smaller than the ordinary quenching distance of given mixture were fabricated. By varying the ratio of channel width and height, the overall ratio of the heat transfer to the outside from top and bottom panels to the heat recirculated to the incoming mixture can be adjusted. For the larger prototypes (o.d. of 64 and 45 mm), the effects of some design parameters of combustion room, channels, and panels on the performance of the combustor are examined. Stability boundaries, heater panel temperature, exhaust gas composition and thermal efficiency as heaters were investigated. Results showed that 64 and 45 mm combustors exhibited wide turn-down ratio attained from 0.4 to 8.0 m/s of the averaged mixture velocity at the inlet of channel. Blow-off limit was not observed for those large combustors due to the high temperature limit of the employed material which is around 1100 K for the stainless steel. Established temperature range is from 400 to 1173 K within the experimental conditions. Temperature controllability of the heater panel is within 1 K from the target temperature when simple feedback control system is introduced. Total thermal efficiency as a heat source ranges from 60 to 85% which is 1.5–2 times
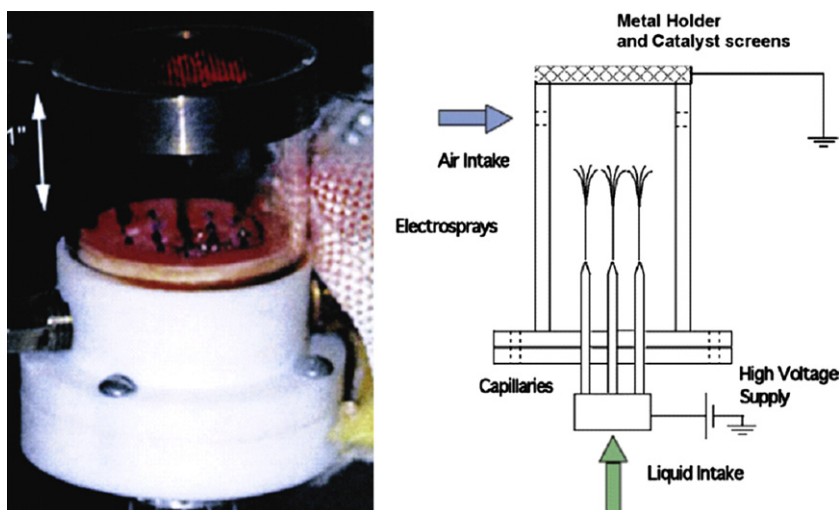

Fig. 16. A catalytic mesoscale burner (left) [33] and electrospray injection system (right) [81] with catalytic screens which act as a uniform and stable high temperature source for energy conversion modules.
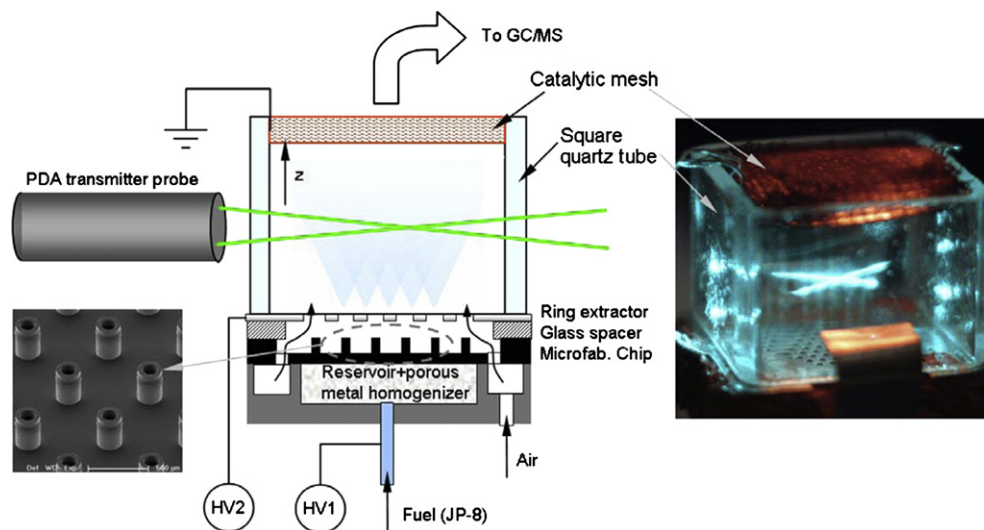
Fig. 17. (a) Scheme of micro-burner with microfabricated electrospray system [82]. An inset SEM micrograph shows some microfabricated nozzles. (b) Optically accessible miniaturized burner in operation.

larger than those of conventional resistive heating devices was attained. Simple analytical model with thermal coupling of gas-phase and combustor body was constructed to examine the effect of design parameters on combustion characteristics and to predict the possible smallest scale of self-sustaining Swiss-roll combustor. Coin-size Swiss-roll combustors with i.d. 26 and 20 mm were fabricated by EDM and their performances were investigated. Results showed that the model predictions agree well with measured performance of the Swiss-roll combustors by showing narrow stability boundaries which have both lower and blow-off limits as shown in Fig. 19. Those combustors are readily applicable for supplying thermal energy to appropriate energy conversion devices at required temperature level.

A small combustor having a stabilized annular flat flame of inner and outer diameter of 5 and 10.5 mm, which would fit the MIT micro-gas turbine was also fabricated by Yuasa et al. [85]. Flame stabilities and effect of design parameters on extinction limits in the developed combustor were examined for hydrogen/air and methane/air mixtures.

Demonstrations of power generation performance by the combinations of catalytic or non-catalytic combustion with thermoelectric and TPV devices were conducted. Integrated power generation system of hydrogen-fueled catalytic combustion on TiO_2 supported Pt with separated TE elements (Bi_2Te_3–Sb_2Te_3 for p-type and Bi_2Te_3–Bi_2Se_3 for n-type elements) recorded 184 mW output from 6.6 W chemical energy input which corresponds to the total
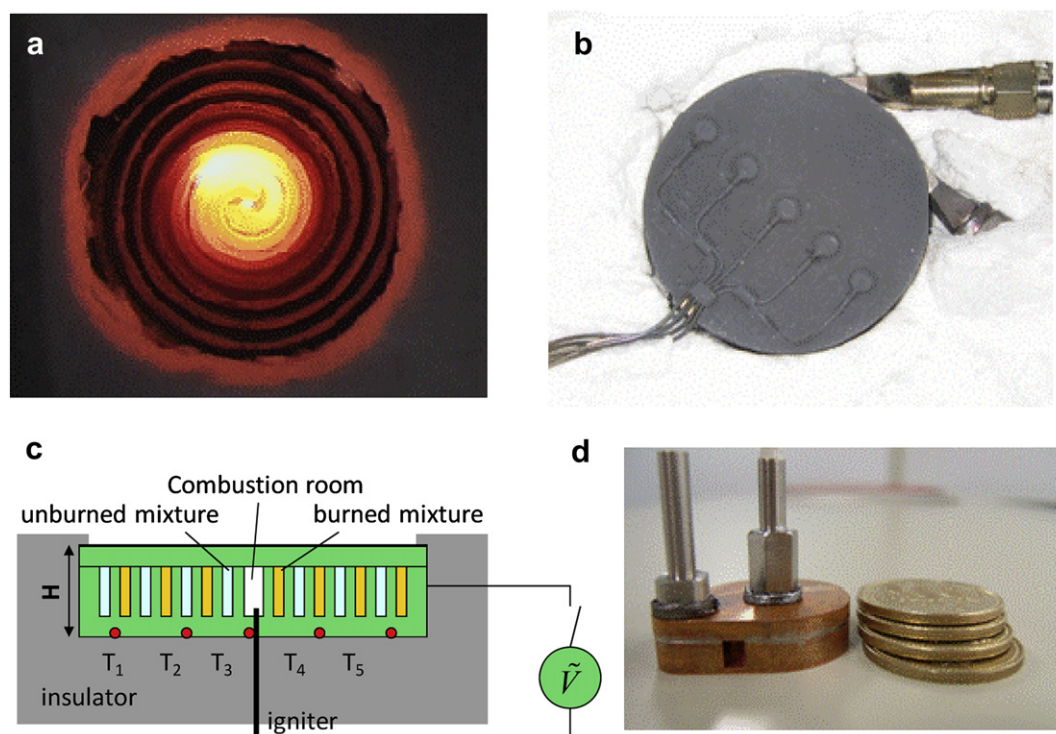

Fig. 18. Disk-shaped Swiss-roll combustors for general purpose heat sources [83,84]. (a) A Swiss-roll combustor in operation; its inside visualized by replacing a top panel with a quartz plate. (b) Cross-section of a Swiss-roll combustor. (c) 46 mm combustor (d) Coin-size combustor (26 mm, o.d.).
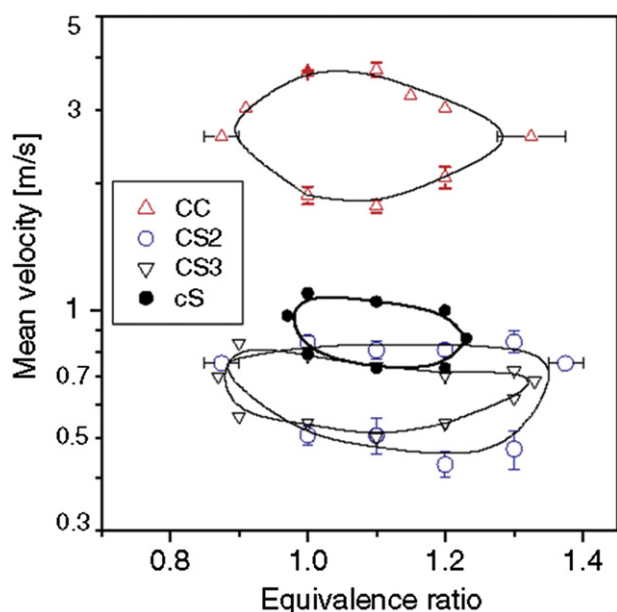
Fig. 19. Flame stabilization characteristics of coin-size Swiss-roll combustors; CC, CS and cS denote 26-mm combustors made of copper and stainless steel, and 20-mm combustor made of stainless steel, respectively. CS2 has slightly wider channel width than that of CS3 [84].

efficiency of 2.8% [86]. Meanwhile, it is reported that an identical system failed to be operated by butane which implies the requirements of further optimization of the combustor design. Catalytic microreactors with high-precision tape-casting method [87] applied for butane accomplished stable operation. Thermal energy density around $2-8 \times 10^8$ W/m^3 [88,89] are achieved for higher temperature application (1073–1173 K) such as TPV devices. Methanol-fueled catalytic micro-reactor system of Pt on anodized aluminum with commercial thermoelectric devices successfully produces 0.65 W electricity output which corresponds to the total efficiency 1.1% [90]. The combination of catalytic combustor and TE devices attained an overall thermal efficiency of converting chemical energy to electricity of $\sim 0.8\%$ with a thermoelectric efficiency of $\sim 3\%$ [91]. They pointed out that large disparity in thermal efficiencies between various works shows the importance of understanding key factors controlling the performance of integrated combustor-thermoelectric devices.

Liquid fuel-film combustors were developed [92–94]. The fuel is injected as a liquid film on the inner surface of cylindrical combustor and swirling airflow provides effective fuel vaporization. It enables reduction of heat losses by redirecting heat toward film vaporization and cools the combustor walls. Due to the large S/V ratio in small scale, large liquid surface area is expected for vaporization. It was shown that internally stabilized flame was attained for liquid fueled flames but not for gas-fueled flames.

A micro-TPV power generator system, consists of hydrogen-fueled cylindrical SiC micro-combustor (3 mm in diameter and 16 mm in length), a nine-layer dielectric filter, and a GaSb (gallium antimony) photovoltaic cell array, generated 1.02 W electricity output from 140.1 W chemical energy input which corresponds to 0.73% total efficiency [95]. Combination of reactor with fuel reformer for hydrogen production is also attempted [96,97]. Characteristics of co-current and countercurrent flow reactor reformer for NH$_3$ reforming on Ru are numerically examined [96]. Effect of heat recirculation on the performance of catalytic micro-combustor is also investigated using catalytic reactor with heat recirculating channel [98]. CFD results showed that the excess enthalpy effect is substantial only in the limit of low-conductivity walls, where there

is insufficient pre-heating of the reactants. Catalytic reactor as a heat source for micro endothermic reactor is fabricated using catalyst bed made from Isolite B5 coated with Pt by the incipient wetness method [99]. Liquid fuel-film combustion is also applied to TPV system [100].

Catalytic micro-reactors are applied also for the development of micro-thrusters [62,101]. Recently, an advanced chemical thruster is proposed for the post-launch propulsion system of small satellites or other micro-spacecrafts, in which the homogeneously catalytic decomposition of hydrogen peroxide (H$_2$O$_2$) is used [102].

3. Flame dynamics of micro-scale combustion

When combustion occurs in a small scale, the increase of surface area and the reduction of characteristic thermal inertia time of the combustor structure will significantly enrich the combustion phenomena via reduced mixing and enhanced wall heat loss, wall-flame thermal and kinetic couplings, and skin friction which lead to various new phenomena such as flameless combustion, weak flame propagation, flame street formation, kinetic extinction, pulsating and spinning instabilities. In this review, we first discuss premixed flame extinction, flame regimes, and instability induced by flame-wall thermal and kinetic coupling in micro-scale combustion. Then, we will present a summary of flame regimes and instability of non-premixed flames. Finally, the effects of catalytic combustion as well as the non-equilibrium transport on micro-scale combustion will be discussed.

3.1. Premixed combustion

A premixed flame is an exothermic self-propagating wave front in a premixture. The propagating speed of a premixed flame relative to the unburned mixture has a unique value and is a function of fuel oxidation chemistry, transport properties, adiabatic flame temperature, and heat and mass losses. Either a radical loss or a heat loss to the environment will slow down the flame speed or even quench the flame, leading to propagation limit. On the other hand, if an external energy is added to the flame, the maximum flame temperature and the flame propagation speed will increase. Therefore, flame with an excess enthalpy will make the flame stronger. For micro-scale combustion, the effects of heat and radical losses on the propagation of a premixed flame will become stronger because the total heat release of a small scale flame is relatively small. Furthermore, micro-scale combustion makes it possible that the heat loss from the flame to the structure can be fed back to the flame with a higher rate because of the reduced thermal inertia and a larger thermal diffusivity of the structure. This thermal feedback or heat recirculation will strongly change the burning regime and propagation limits of a conventional flame in a large scale. One of the most important things in micro-scale combustion is to understand how the flame structure thermal coupling will extend the classical flammability limit and render micro-scale combustion possible.

3.1.1. Flammability limit and quenching diameter

The so called standard flammability limit is defined as the lean and rich flame propagation limits of a one-dimensional, infinite, planar, and unstretched flame. The theoretical and experimental determination of flammability limits have been conducted for more than several decades [21,103–117]. It has been concluded that the radiation heat loss from the emitting species such as H$_2$O and CO$_2$ is the cause of the flammability limit. The mass burning rate (flame speed) normalized by the adiabatic mass burning rate (flame speed) as a function of normalized radiative heat loss, H, by the total chemical heat release can be given as,

$$U^2 \ln U^2 = -\beta H \qquad (1)$$

As shown in Fig. 20, with the increase of normalized heat loss (H) (i.e. the decrease of fuel concentration), the flame speed decreases. As the normalized heat loss increases to a critical value ($\beta H = e^{-1}$, where β is the Zeldovich number) and the normalized flame speed reaches a critical value ($e^{-1/2}$), beyond which (leaner or richer conditions) no flame is self-sustainable. This critical condition (fuel lean or fuel rich concentration) is the so called flammability limit.

For micro-scale combustion, the heat loss does not just come from the radiation heat loss, but mainly from the convection and conduction heat losses to the wall. From a simple normalization [40], the normalized convective heat loss of a flame in a cylindrical channel with an inner diameter of d by the chemical heat release can be given as,

$$H = \frac{\text{Heat loss to the wall}}{\text{Total chemical heat release}} = \frac{4\delta_f^2}{d^2} Nu \qquad (2)$$

For a fully developed laminar flow in a channel at a constant wall temperature, the Nusselt number can be assumed constant (Heat transfer book, e.g. Holman [118]). Therefore, the normalized heat loss from the flame to the wall is proportional to the square of the ratio of flame thickness to the channel diameter. If one assumes a constant flame thickness for a given mixture, the heat loss to the wall will be proportional to square of the inverse of the channel diameter. From Eq. (1), the flame speed will depend on the channel diameter as

$$U^2 \ln U^2 = -\beta \frac{4\delta_f^2}{d^2} Nu \qquad (3)$$

From Fig. 20, it is readily known that the propagation limit will be,

$$d_0 = 2\sqrt{e\beta Nu}\,\delta_f \qquad (4)$$

This limiting tube diameter, d_0, is called the quenching diameter below which a flame fails to propagate in a channel. If the Nusselt number for convective heat transfer in a laminar cylindrical flow takes a value between 3.66 and 4.36 and the Zeldovich number β is about 10, Eq. (4) shows that the quenching diameter is about 16 times that of the flame thickness. Since flame thickness depends on the thermal diffusivity and flame speed (i.e. fuel concentration and

flame temperature, the quenching diameter is a function of fuel concentration and the thermochemical properties of fuel.

The earliest measurement of quenching diameter was made by Davy [21,103]. Since the flame and the flow in a tube are not one-dimensional, the measured quenching diameter is a function of flow rate, ranging between $d/\delta_f = 10$ to 30. For example, for stoichiometric hydrogen, propane, and methane/air mixtures, the measured dimensional quenching diameters are between 2 mm and 5 mm, depending on the experimental conditions. Recently, flame propagation in a narrow channel has been computed numerically [36,38]. Fig. 21 [35] shows the dependence of the normalized flame propagation speed in a quiescent channel on the channel width (d) for various values of convective heat loss (k), which is proportional to the Nusselt number (Nu) in Eq. (3). It is seen that for an adiabatic wall ($k = 0$), there is no heat loss from the flame to the wall and the flame speed does not depend on channel width ($Nu = 0$ in Eq. (3)). With the increase of heat loss intensity, the flame speed decreases and there is a critical channel width (the smallest value of d), below which flame fails to propagate. This critical channel width is equivalent to the quenching diameter at a given heat loss. As the convective heat transfer rate becomes infinite ($k = \infty$), the wall temperature is always at room temperature, the result shows that flame extinguishes at $U = 0.6$ and the resulting quenching channel width is $2\delta_f/d_0 \approx 0.13$ or $d_0/\delta_f = 15$, which is consistent to the theoretical prediction (Eq. (3)) and the observed experimental results. The study further demonstrated that when the wall is cold, near wall-flame quenching occurs within a region of $6\delta_f$. Furthermore, it was also shown that the flow velocity and direction also affects quenching diameter. If the flow is directed from the unburned side to the burned side, flame is more vulnerable to heat losses. In particular, the quenching distance increases as the mean flow rate increases. All these findings from numerical simulations are in general agreement with experimentally reported values [119].

The effect of Lewis number on the flame geometry and flame speed for a flame propagating in a circular channel was computed by Kurdyumov et al. [120] by using a three-dimensional model. The results showed that when Le is less than unity, the flame speed is larger than that of the adiabatic flame (Fig. 22). In addition, if the tube diameter is sufficiently larger than the quenching diameter, flame structures become three-dimensional and flame speed changes dramatically. However, for a channel width close to the quenching diameter, the results showed that a two-dimensional analysis is appropriate to predict the quenching phenomena.
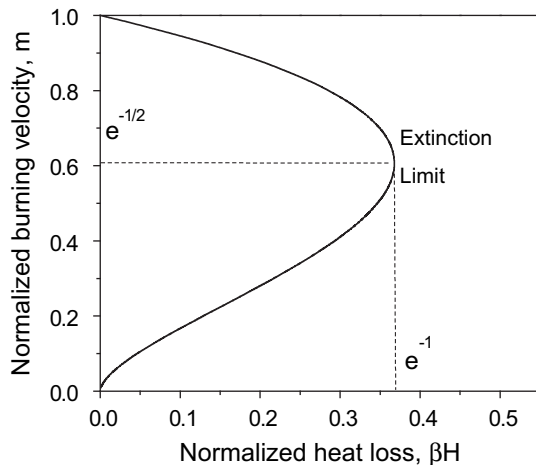

Fig. 20. The dependence of the normalized burning velocity on the normalized radiative heat loss of a one-dimensional planar flame.
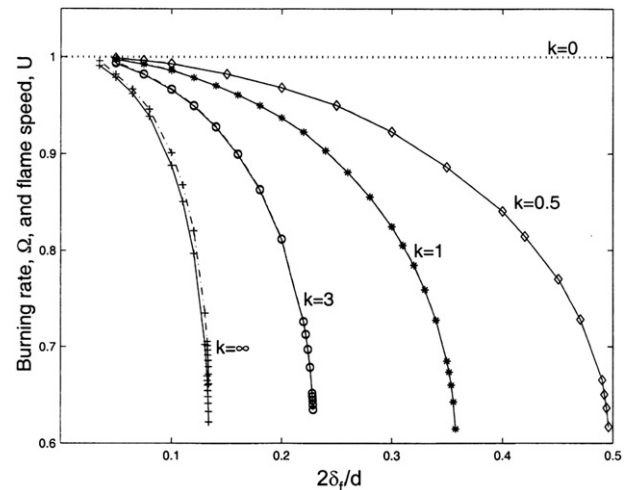

Fig. 21. Burning rate (solid line) and normalized flame propagation speed U (dash-dotted line) plotted against the ratio of flame thickness to channel width (d) for selected values of reduced heat transfer coefficient (k) with in a quiescent, two-dimensional channel flow [35].
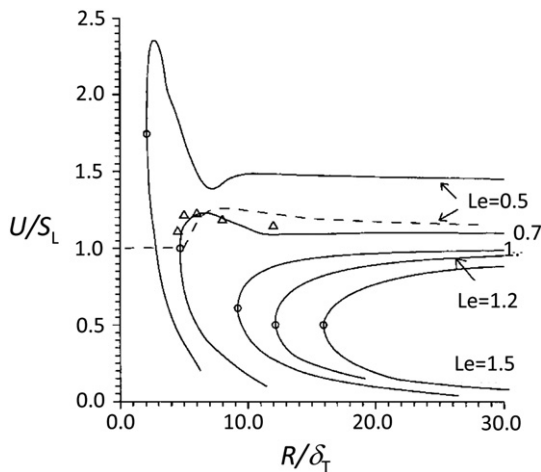
Fig. 22. Effect of Lewis number on flame geometry and flame speed [120].

For a quite long time, researchers believed that combustion in a scale below the "standard" quenching diameter (at cold wall conditions) was not possible. Fortunately, the idea of heat recirculation or excess enthalpy made the standard quenching diameter or flammability limit less relevant. Therefore, it is important to understand how significantly the heat recirculation from the burned gas to the unburned gas in a Swiss-roll will affect flame speeds.

3.1.2. Heat recirculation

Since the pioneering work of Weinberg and coworkers [24,25], (Fig. 23a, Weinberg), extensive experiments and numerical simulations [28,64,83,84,121,122] have been conducted to study the effect of heat recirculation on flame speeds and flammability limit.

As shown in Fig. 23a and b, the combustor chamber of the Swiss-roll burner is located in the center of the Swiss-roll. The cold unburned mixture flows into the combustion chamber tangentially. In parallel to the unburned mixture, the burned gas flows out tangentially from the combustion chamber. As a result, the burned gas will transfer its enthalpy to the unburned gas (Fig. 23c and d) and results in excess enthalpy combustion in the combustion chamber.

In order to understand the dynamics of flame with heat recirculation, Ronney [28] and Ju and Choi [29] conducted theoretical analyses independently by using simplified Swiss-roll models (Fig. 23c and d). In Ronney's analysis (Fig. 23c), a U-shaped combustion model is used. The model assumes that at the end of the U-shaped combustor, there is a well stirred reactor (WSR). The unburned mixture flows into the WSR and the burned hot gas flows out from the WSR, allowing heat transfer between the burned and unburned gases. To further simplify the problem, the model assumes that flame is always stabilized in the WSR, so that it is not necessary to consider flame propagation and heat transfer in flow direction. Emphasis can be paid on the effect of heat recirculation only. In fact, the flame location in a Swiss-roll is a dynamic balance between flame speed and flow speed. The flame location depends on the experimental condition and may not be in the center of the Swill-roll. In order to examine the dynamic effect of flame location and predict the flame speed as a function of flame location and heat recirculation, Ju and Choi [29] employed opposite propagating flame model (Fig. 23d). The unburned mixtures in two parallel channels flow in opposite direction, so that the burned gas in one channel will preheat the other. Since both flames are exactly the same, the mutual heat recirculation can be considered as self-heat recirculation. This model allows the flame to change both its location and to consider heat transfer both in streamwise direction and across the walls. Therefore, the flame speed and flame separation
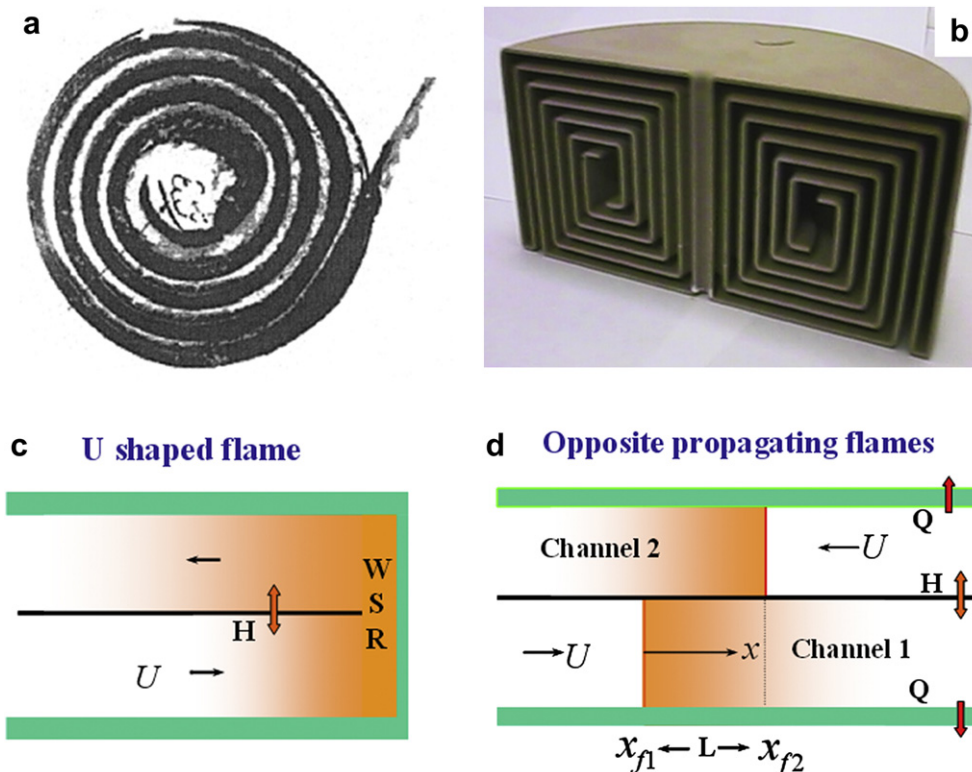

Fig. 23. Swiss-roll burners and simplified heat recirculation models: a. two-dimensional Swiss-roll by Weinberg et al. [24,25]; b. three-dimensional Swiss-roll by Ronney et al.; c. the U-shaped flame model by Ronney; and d. the opposite propagation flames by Ju and Choi [29].

distance between the two flames ($x_{f1} - x_{f2}$) will be an eigenvalue of the mixture concentration, heat transfer rates cross the wall, and heat losses (Q) to the environment. This model can mimic dynamically the flame dynamics in a Swiss-roll with heat recirculation.

Fig. 24 [28] shows the dependence of flame temperature at the WSR on the flow rate for finite reaction rates ($Da = 10^7$) with adiabatic flame temperature rise after complete combustion of $\Delta T = 1.5$ at various Biot number (B) and normalized heat loss coefficient (H). It is seen that for an adiabatic U-shaped reactor ($H = 0$) with an infinite reaction rate ($Da = \infty$), the flame temperature increases as the flow rate decreases. This is because of the increase of heat transfer rate of unit mass of flow at a smaller flow rate. However, for a finite Da, the results show that there is a maximum flow rate beyond which flame is not able to be stable at the WSR. Moreover, as heat loss appears, an extinction at low flow rate also occurs. This is because the heat loss from the unit mass of flow increases when the flow rate decreases. The results qualitatively support the experimental observation.

Fig. 25 [29] shows the dependence of flame speed on the factor of convective heat loss (H) for different convective heat transfer coefficient across the wall (χ). When there is heat recirculation (χ), extinction occurs at a critical value H_c. For heat loss less than H_c, there are two flame speeds, a fast mode and a slow mode. The existence of these two flame modes can also be seen in Fig. 25 (there are two different flame temperatures at a give flow rate). For heat loss larger than H_c, no flame can be held. However, by allowing heat recirculation ($\chi > 0$), it is seen that the critical heat loss to quench the flame increases significantly with the increase of heat recirculation. In addition, the flame speed increases dramatically, particularly at near adiabatic conditions. This figure clearly demonstrates the effectiveness of heat recirculation on sub-limit combustion, that is, flame can burn strongly and exist below the classical quenching diameter if heat recirculation is allowed.

To demonstrate the effect of heat recirculation on the extension of the lean flammability limit, Fig. 26 shows the dependence of the flame separation distance on the fuel mass fraction with a heat loss at $H = H_c$. Therefore, the fuel mass fraction at $\chi = 0$ defines the standard lean flammability limit without heat recirculation ($\varphi = 0.0365$). At the flammability limit, both flames can be located independently so that the flame separation distance is arbitrary. However, by allowing and increasing the heat recirculation strength ($\chi > 0$), the flame can be held in much leaner conditions, indicating the existence of sub-limit flames. Moreover, due to the
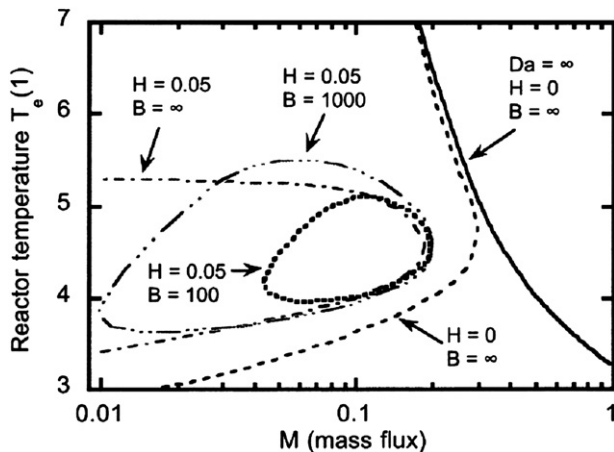

Fig. 25. The dependence of flame speed on the external heat loss at different intensity of heat recirculation for normalized fuel mass fraction of 0.0365 and flame separation distance of $L = 0$ [29].

need of heat recirculation for a sub-limit flame, the flame separation distance is finite and bound to a given region. As the heat recirculation intensity increases, the sub-limit flammable region is dramatically extended and the flame separation region becomes very narrow, which is close to the case of the WSR assumption in Fig. 23c. By using these analytical formulations, the flame speed and the extended flammability limit can be appropriately estimated assuming that appropriate parameters are employed.

3.1.3. Flame and structure coupling

The analysis of heat recirculation emphasizes the direct enthalpy transfer from the burned gas to the unburned cold mixture. There is another indirect enthalpy transfer from the burned gas to the unburned gas through the heat loss from flame to structure and then from structure to unburned gas (Fig. 27). Because the rate of heat recirculation depends on the rate of heat conduction in the structure, the indirect heat recirculation via combustor wall structure will cause a strong thermal coupling between flame and the wall. Fig. 27 schematically shows how the flame-wall structure thermal coupling affects the flame

Fig. 24. Effect of mass flux on WSR temperature in the countercurrent combustor for finite reaction rates at $Da = 10^7$ with $\Delta T = 1.5$. (B: Biot number, H: normalized heat loss coefficient) [28].
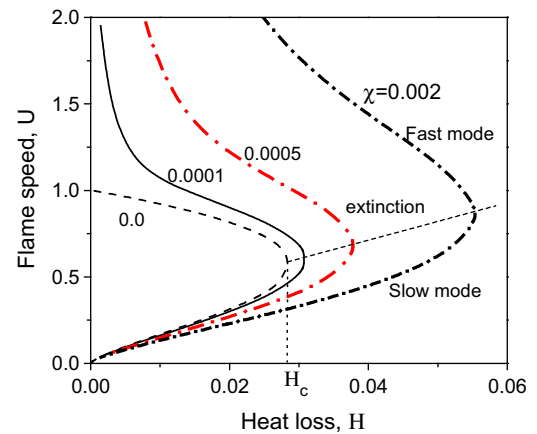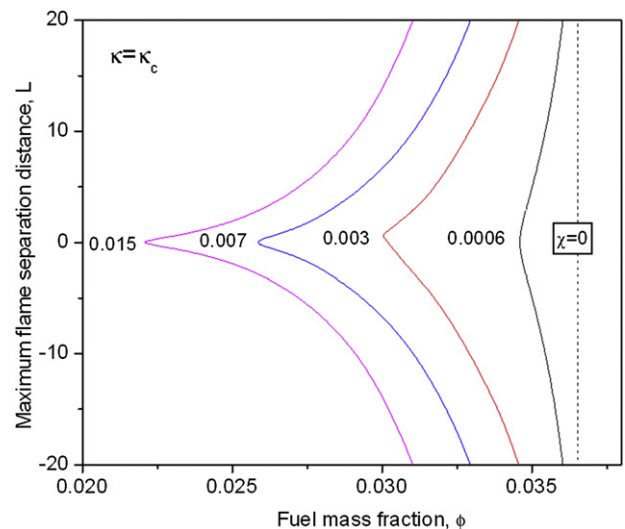

Fig. 26. The diagram of flammable region: dependence of maximum flame separation distance on fuel mass fraction [29].

propagation. When a flame propagates at a velocity of U_f relative to a channel with width of d and mean flow velocity of u, the burned gas loses energy to the wall structure at a rate coefficient of H. A fraction of the heat loss H will lose to the environment at a rate of H_0. The rest of it (Q) will be transferred upstream and given back to the unburned gas. Therefore, the heat recirculation strongly depends on the heat transfer rates of the inner and outer walls, the thermal diffusivity of wall structure, and the thermal heat capacity of the structure. In addition, the direction of heat condition in the solid phase is parallel to that the thermal diffusion of the gas-phase. As a result, the indirect heat recirculation will change the effective Lewis number and the flame dynamics accordingly.

To understand the flame dynamics with flame-wall structure coupling, a theoretical analysis was carried out by Ju et al. [40] by using a simplified model shown in Fig. 27. By assuming a constant wall temperature at far upstream (T_w), uniform flow velocity, constant properties, a thin flame model, and one-dimensional quasi-steady-state flame propagation, the normalized governing equations for energy of gas-phase, energy in solid phase, and the fuel mass fraction in the coordinate attached to the flame front can be rewritten as [40],

$$
\begin{aligned}
(u - U_f)\frac{d\theta}{dx} &= \frac{d^2\theta}{dx^2} - H(\theta - \theta_w) + \exp\left(\beta(\theta_f - 1)/2\right)\delta(x - x_f) \\
(u - U_f)\frac{dY_F}{dx} &= \frac{1}{Le}\frac{d^2Y_F}{dx^2} - \exp\left(\beta(\theta_f - 1)/2\right)\delta(x - x_f) \\
-U_f\frac{d\theta_w}{dx} &= \frac{d^2\theta_w}{dx^2}\frac{\alpha_w}{\alpha_g} + HC(\theta - \theta_w) - H_0C\theta_w/\beta
\end{aligned}
\tag{5}
$$

The boundary conditions are

$$
x \to -\infty,\ \theta = \theta_w = 0,\ Y_F = 1;\ x \to +\infty,\ \frac{d\theta}{dx} = \frac{d\theta_w}{dx} = 0,\ Y_F = 0 \tag{6}
$$

here, H and H_0 are the normalized convective heat transfer coefficients on the inner and outer walls of the channel, C the ratio of heat capacity of gas-phase to the solid structure, Le the Lewis number, α_g and α_w the thermal diffusivities of gas and solid structure, and β Zeldovich number, respectively. It will be shown that these parameters govern the flame regimes via flame-wall structure coupling.

By using method of the large activation energy analysis [123], the solution of flame speed ($m = u - U_f$) becomes,

$$
m = \exp\left(\frac{\beta(\theta_f - 1)}{2(1 + \sigma(\theta_f - 1))}\right),\quad \theta_f = \theta_f^0 + \theta_f^1/\beta \tag{7}
$$

where σ is the heat release parameter and θ_f^0, θ_f^1, A and B can be obtained from the following algebraic equations,

$$
-m = F(\lambda_3 - \lambda_1) + A(\lambda_1 - \lambda_2) - B\lambda_3 \tag{8-1}
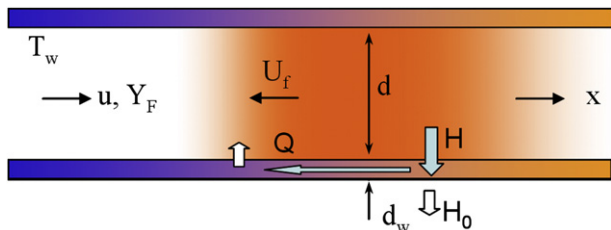$$

Fig. 27. Schematic of flame propagation in a mesoscale channel with indirect heat recirculation through flame-wall structure thermal coupling.

$$
F\left(\theta_f^0 - A\right) + DA = E\left(\theta_f^0 - B\right) + B \tag{8-2}
$$

$$
B = m/\left(m - U_f/C\right) \tag{8-3}
$$

$$
\theta_f^1 = -\frac{H_0}{m - U_f/C}\left[\frac{\beta(1 + \alpha_w/\alpha_gC)}{m - U_f/C} + \frac{F\left(\theta_f^0 - A\right)}{\lambda_1} + \frac{AD}{\lambda_2}\right] \tag{8-4}
$$

in which λ_1, λ_2, and λ_3 are, respectively, the eigen-function of the following third-order ordinary differential equations

$$
\begin{aligned}
&\frac{\alpha_w}{\alpha_gC}D^3 - \left(\frac{\alpha_w}{\alpha_gC}m + \frac{n}{C}\right)D^2 + \left(-\frac{\alpha_w}{\alpha_gC}H - H + \frac{nm}{C}\right)D \\
&\quad - \frac{U_f}{C}H + mH = 0
\end{aligned}
\tag{9}
$$

and D, E, and F are calculated from,

$$
D = 1 + \frac{m\lambda_2 - \lambda_2^2}{H},\ E = 1 + \frac{m\lambda_3 - \lambda_3^2}{H},\ F = 1 + \frac{m\lambda_1 - \lambda_1^2}{H} \tag{10}
$$

In the limit case of zero thermal conductivity of the wall ($\alpha_w = 0$), that is, the wall becomes a heat sink with no thermal conduction to allow heat recirculation, the problem reduces to the flame propagation in a particle laden mixture, in which particles have heat transfer with the gaseous flame but not between each other. Eqs. (7)–(10) become

$$
\ln m^2 = -\frac{\beta H(2m^2 + CH)}{(m^2 + CH)^2} \tag{11}
$$

which is exactly the same as the solution of the particle laden flame obtained by Joulin [124]. Eq. (11) shows that there is a maximum particle loading heat capacity (C) beyond which flame extinguishes.

In the limit of zero wall heat capacity ($C = 0$), Eq. (11) further reduces to

$$
m^2\ln m^2 = -2\beta H,\quad m = u - U_f \tag{12}
$$

which defines a quenching diameter in a channel with a mean flow velocity of u. For zero flow velocity, Eq. (12) becomes Eq. (1). A factor of two appears in Eq. (12) is because the heat loss to both walls of the channel in Fig. 27.

Fig. 28 [40] shows the effect of flow velocity on the flame propagation speed for relative wall heat capacity of $C = 0.01$ and thermal diffusivity ratio of $\alpha_w/\alpha_g = 0.1$. It is seen that at $u = 0$, the extinction curve is similar to Fig. 25. The extinction limit defines the quenching channel width or the burning limit of fuel concentration. However, when the flow speed is increased to $u = 0.1$, different from the results of zero flow rate, it is seen that there exist two steady-state flame solutions and two extinction limits. There is a new flame branch which has a flame velocity almost equal to the flow speed. This new flame regime is called the "weak flame" induced by strong flame-wall structure thermal coupling. At $u = 0.1$, the new flame regime has a quenching diameter larger than the standard quenching diameter of the normal flame. However, as the flow velocity further increases to $u = 0.2$, it is interesting to note that the weak flame regime extinguishes at a larger heat loss coefficient (H) than that of the normal flame, indicating that the weak flame regime can be stabilized at a combustor with a scale smaller than the standard quenching diameter. In addition, it is noted that with the increase of flow velocity, the normal flame extinction limit does not change. The flame transition from the normal flame to the weak flame is via extinction transition. As the flow speed increases to $u = 0.5$, it is seen that the extinction

quenching diameter of the weak flame further decreases (large H) and the flame transition from the normal flame to the weak flame is a smooth transition without extinction limit. It is also interesting to note that when the flow velocity is higher than the adiabatic flame speed ($u > 1$), the flame speed with flame-wall structure thermal coupling can be higher than the adiabatic flame speed. This theoretical result strongly suggests that micro-scale combustion is only possible when strong flame-wall combustion is enabled.

Fig. 29 [40] shows the dependence of the flame speed on the normalized heat loss coefficient for various wall thermal diffusivities. It is seen that the wall thermal diffusivity affects the flame speed dependence on heat loss significantly. At a small wall thermal diffusivity, there are two flame regimes and two extinction limits. However, at a high wall thermal diffusivity, the two flame regimes combine into a new flame branch, leading to a dramatic reduction of the quenching diameter. Therefore, when flame-wall thermal coupling is encouraged, materials with a higher thermal diffusivity has more extended flammability limit.

Experimental observation of the two different flame regimes and the increase of flame speed with flow velocity in a mesoscale ($d = 5$ mm) was also conducted. Fig. 30 [40] shows the measured time history of flame fronts at various equivalence ratios for C_3H_8-air mixtures. It is seen that flame location depends very linearly on time. At equivalence ratio of 0.73, the imbedded flame images show that there exist two different flame histories (regimes). One flame (upper, high speed camera image) propagates faster (3.5 cm/s relative to the channel wall) and the other weak flame (lower, CCD camera image) propagates only at a speed of less than 1 mm per second. These two flames correspond respectively to the fast and slow flame regimes predicted in Fig. 28.

The measured flame speed of methane-air mixtures as a function of equivalence ratio is shown in Fig. 31 for flow rates at 5.3, 5.69 and 6.09 cm³/s, respectively [38]. The results show the interesting transitions between the two flame regimes which was predicted by theory. The results show that there are two flame regimes and their transition depends on flow rate. For a low flow rate of 5.3 cm³/s, the transition from normal flame to weak flame is an extinction transition. However, for a high flow rate the transition is a smooth transition. In addition, it is seen that the flame speed of weak flames increases with the flow rate. The existence of different flame regimes was also observed by Maruta et al. [41]. Earlier experiments by Zamashchikov [125] also showed the existence of weak flames in a quartz tube at very low propagating velocities for nitrogen diluted methane flames, although the fundamental mechanism was not well understood.
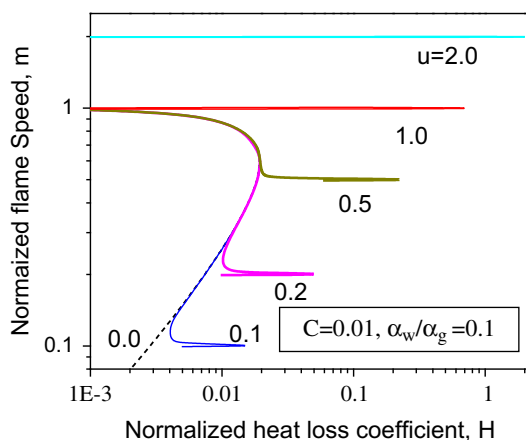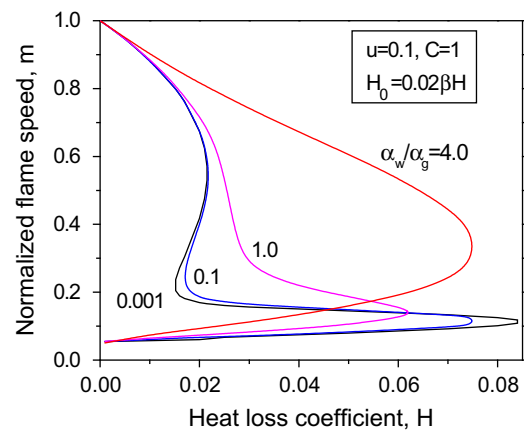

Fig. 29. The effect of flow velocity on flame speeds, flame regimes, flame regime transition, and extinction limits (quenching channel width) [40].

A one-dimensional numerical model for reacting flow in a micro-channel with flame structure thermal coupling has been developed by Leach et al. [43] to identify optimum configurations for micro-combustors. The model shows that as the size of a combustor is reduced, axial heat transfer through the structure from the post-flame to the pre-flame plays an increasingly important role in determining the combustor performance by broadening the reaction zone and increasing the burning rate. The model also shows that heat transfer from the structure to the environment places a lower limit on the combustor volume that tends to decrease with increasing pressure. The combustor design that maximizes power density generally does not maximize efficiency.

Two-dimensional modeling of the flame-wall thermal coupling was also conducted [38,50,126,127] to examine the effects of near wall-flame quenching and flame structure on the flame regimes and propagation speed. Fig. 32 [38] shows the dependence of flame speed on the fuel mass fraction for flame propagation in a two-dimensional channel with a parabolic flow distribution for methane-air mixtures. Constant thermal properties and one-step reaction model were employed. The channel width is 20 times that of flame thickness. It is seen that similar to the one-dimensional theory, two flame regimes and two different kinds of flame transitions also exist. In addition, the weak flame velocity increases
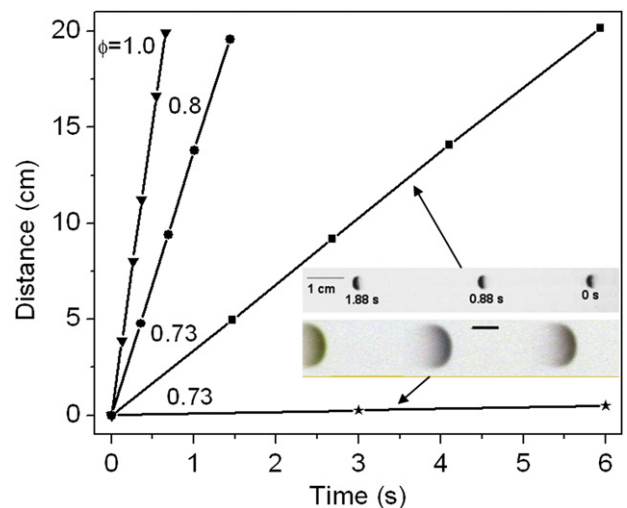

Fig. 28. The effect of flow velocity on flame speeds, flame regimes, flame regime transition, and extinction limits (quenching channel width) [40].

Fig. 30. Time history of flame location for various equivalence ratios and flame regimes for C_3H_8-air flame with $d_i = 5$ mm; upper image: fast flame recorded by high speed camera; lower image: slow flame recorded by CCD camera [40].
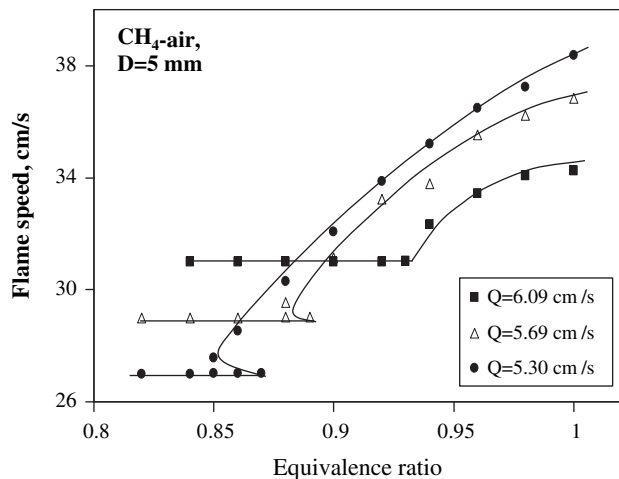
Fig. 31. Dependence of flame speed on equivalence ratio for CH$_4$-air flame with $d_i = 5$ mm [38].

with the flame rate. However, different from the one-dimensional theory and simulations, the normal flame speed decreases with the increase of flow velocity. Moreover, the flame speed of the weak flame is significantly lower than the mean flow velocity because of the flame curvature and near wall extinction. The results reproduce the experimental results in Fig. 31 qualitatively.

The comparison of flame structures (contours of temperature, reaction rate, and fuel mass fraction) without (left) and with (right) flame-wall thermal coupling for flame propagation in a channel with ($d/2 = 10\delta_f$) is shown in Fig. 33 [38]. It is seen that without flame-wall coupling, the wall temperature ($y > 10$) is held constant and flame quenching occurs near the wall surface. In addition, the flame surface is curved and has a smaller surface area than the cross-section area of the channel. This is why the normal flame speed is lower than the mean flow velocity (Fig. 32). For the flame-wall coupling case (Fig. 33, right), the temperature contours shows that the heat conduction in the wall structure is faster than that of thermal diffusion in the gas flow, leading to an indirect heat recirculation. This is the reason why the flame-wall thermal coupling can stabilize a weak flame at a fuel concentration or a channel width far below that of the normal flame.

Flame propagation in microchannels (around 100 μm) was also modeled by Vlachos and coworkers [128–131] using two-dimensional parabolic equations with detailed multi-component transport and gas-phase chemistry. The results showed that the near entrance heat and radical losses at the wall are key issues in controlling flame propagation.

More recently, multi-dimensional direct numerical simulations with detailed chemistry and transport for fuel lean ($\phi = 0.5$) hydrogen/air flames in planar microchannels with prescribed wall temperature was conducted [126,127]. Comprehensive flame responses including oscillating, chaotic and ignition/extinction flame dynamics are obtained. Details are discussed later in Section 3.4.1.

Various mesoscale combustors actively using indirect heat recirculation via structure conductive and radiative heat transfer to enhance combustion have been developed [92,132]. For example, Marbach and Agrawal [132] developed a mesoscale combustor by using porous inert media in an annular preheat zone around the combustor (Fig. 34). The methane fuel and air were injected into the pre-heating annulus at six equally spaced injection ports. The annulus measured 100 mm long with an inner diameter of 27 mm and an outer diameter of 34 mm.

Fuel and air were mixed and preheated in the annulus filled with an 80 mm long bed of packed stainless steel spheres of 3 mm diameter by heat conduction and radiation. The preheated fuel/air mixture entered the inner passage through four 12 mm diameter holes. Combustion was stabilized above the surface of the 25 mm long inner porous inert media, a monolithic SiC coated, carbon foam of 12 ppcm. The free space of the combustion chamber was 20 mm in diameter and 63 mm long. The combustor was insulated with 25 mm thick Insulfrax insulation. System performance for a range of operating conditions was determined experimentally using methane fuel. Preheat temperatures in excess of 600 K. The results showed that the product gas temperature in the mid-section at the combustor exit was higher than the adiabatic flame temperature of the incoming reactants, yielding superadiabatic combustion. Pre-heating of the reactants allowed very lean combustion, with equivalence ratio of about 0.40 at lean blow-off. The NOx and CO concentrations increased with increasing reactant flow rate and equivalence ratio.

3.1.4. Thermal and kinetic quenching

Due to strong flame-wall thermal coupling, the wall temperature increases as the size of combustor decreases. In addition, the diffusion time scale is proportional to the square of the combustor length scale,

$$t_D \propto d^2/D \qquad (13)$$

As the length scale of the combustor decreases, the diffusion time of chemical radicals from the flame zone to the wall will become comparable to the characteristic formation time of radicals, leading to a strong kinetic radical quenching on the wall surface. The radical quenching will be coupled with thermal quenching and render simulations of micro-scale combustion inapplicable without considering radical recombination in the wall [54], particularly at high wall temperatures.

Aghalayam et al. [54] studied the effect of radical wall quenching in flame stability and wall heat flux of hydrogen-air flames on a hot wall. The results showed that the quenching of radicals such as H and OH caused the delay of ignition and that the thermal feedback from the wall recombination of radicals rendered the flame more stable and led to a higher wall heat flux as a function of wall temperature compared to an inert surface under some conditions. Recently, high temperature micro-burners with radical
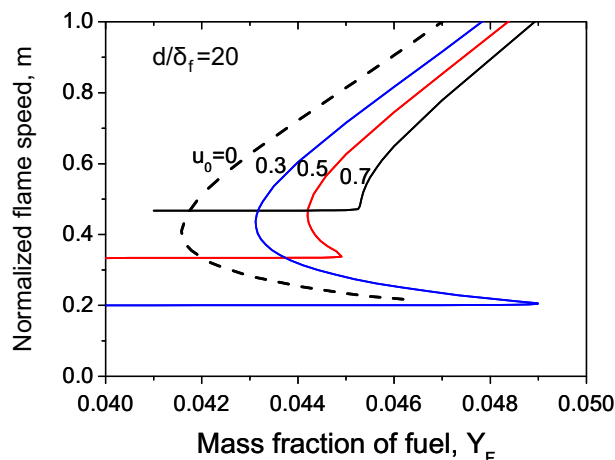

Fig. 32. Dependence of simulated flame speed on fuel concentration in a two-dimensional channel with a parabolic flow distribution, the channel width is 20 times that of flame thickness [38].
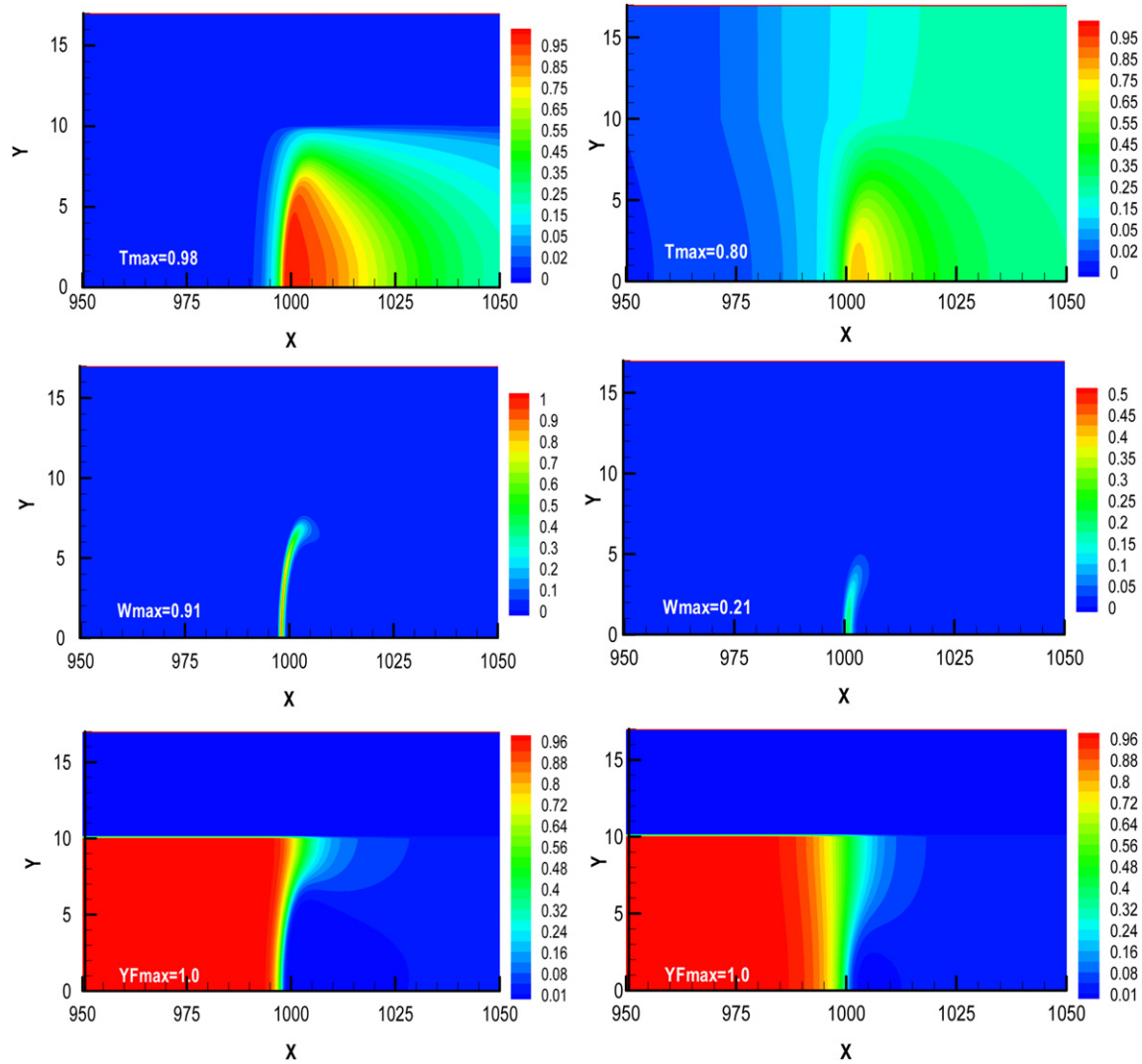
Fig. 33. The distributions of temperature(top) reaction rate (middle), and fuel concentration (bottom) of the normal flame (left) and the weak flame (right) at $Y_F = 0.044$ for $u = 0.3$, the half channel width is ten times of the flame thickness, $y = 0$ is the centerline and $y = 10$ is the wall surface of the channel, respectively [38].

quenching on the wall surface were modeled by Raimondeau et al. [128] and Norton and Vlachos [129]. Combustion of a stoichiometric mixture of methane in air at atmospheric pressure for a flow rate of 2 m/s in a cylindrical micro-channel with a radius of 100 μm and wall temperatures above 1200 K was simulated by considering some important radical quenching reactions listed in Table 5.

Fig. 35 [128] shows the computed distribution of mole fraction of methane (a) and dimensionless temperature (normalized by 1273.5 K) along the length of the reactor with wall quenching (solid lines) and without wall quenching (dashed lines). Fig. 35 shows that radical quenching can result in a lack of flame propagation. It was found that the rate of heat released by radical recombination at the wall is insufficient to compensate for the rate of heat loss through the wall. Therefore, the kinetic mechanism clearly dominates over the thermal one.

In order to understand qualitatively the impact of wall temperature, radical quenching, and radical transport on the flame propagation speed in a micro-channel with a parabolic flow, numerical computations were made by using a skeletal kinetic model [133],
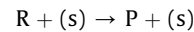
$$F \rightarrow R \qquad \qquad \text{(I)}$$
Initiation
$$R + F \rightarrow 2R \qquad \qquad \text{(II)}$$
Branching

$$R + R\,(+M) \rightarrow 2P\,(+M)\; +\; Q \qquad \qquad \text{(III)} \qquad (14)$$
Termination and radical quenching

$$R + (s) \rightarrow P + (s)$$

where F, R, and P represent reactants, radicals, and products and s denotes the surface sites. The chain initiation, branching, and termination reaction rates are given as,

$$\omega_I = \rho Y_F \exp\left[\frac{E_{aI}}{R_0}\left(\frac{1}{T_I} - \frac{1}{T}\right)\right]$$

$$\omega_{II} = \rho^2 Y_F Y_R \exp\left[\frac{E_{aB}}{R_0}\left(\frac{1}{T_B} - \frac{1}{T}\right)\right] \qquad (15)$$

$$\omega_{III} = \rho^2 Y_R Y_R$$

where the activation energies of the initiation and branching reactions are, respectively, $Ea_I = 90$ kcal/mol and $Ea_B = 30$ kcal/mol. The cross-over temperatures for initiation and branching reactions are, respectively, $T_I = 3000$ K and $T_B = 1100$ K. The radical quenching rate is simplified by using a radical quenching coefficient (γ_s) for the molecular collision flux on the wall,
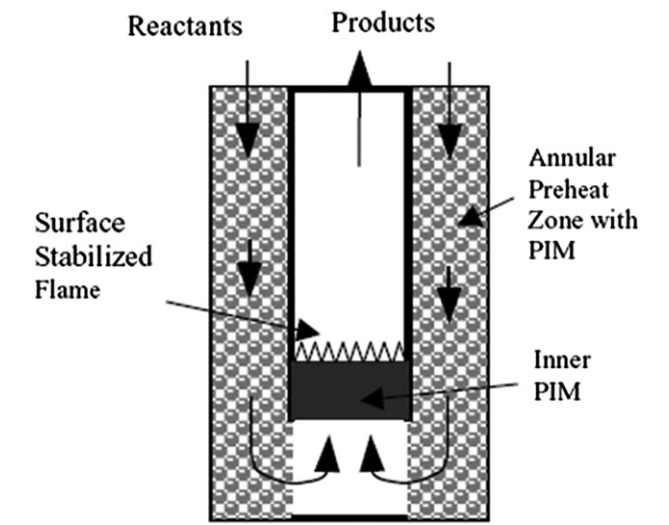
Fig. 34. Schematic of the proposed mesoscale, heat recirculating combustor [132].

$$\omega_S = \gamma_S n_R c_R / 4 \qquad (16)$$

where n_R is the radical number density and c_R is the radical mean molecular velocity. All calculations were made by assuming constant properties.

Fig. 36 shows the effect of wall temperature on the flame propagation speed normalized by the adiabatic flame speed for different channel width [133]. At a low temperature (500 K), which is far below the chain-branching cross-over temperature (1100K), the thermal quenching is dominant. However, as the wall temperature increases to 850 K, the radical quenching plays more important role to accelerate the flame quenching. This effect becomes more significant when the wall temperature approaches the chain-branching cross-over temperature.

Fig. 37 shows the effect of radical quenching coefficient on the normalized flame speed for different channel widths and radical Lewis numbers [133]. For a large channel width ($d/2 = 3.25$), flame speed decreases with the increase of radical quenching coefficient indicating that the decrease of flame speed is limited by the rate of radical recombination. However, when the channel width is small ($d/2 = 2.7$), the results show that the flame speed decreases with an initial increase of radical quenching coefficient, however, a further increase of radical quenching rate does not affect the flame speed. This implies that the radical quenching is limited by diffusion transport. Therefore, in micro-scale combustion, thermal quenching is dominant when the wall temperature is low. However, radical quenching plays an increasingly important role in affecting flame propagation as the wall temperature increases.
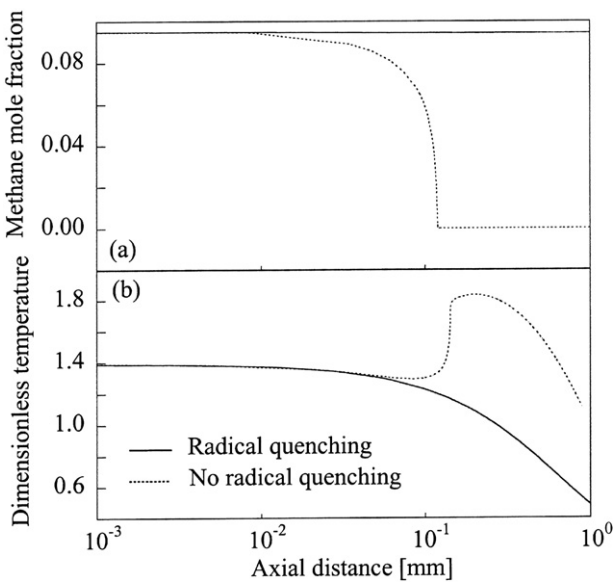

Fig. 35. Mole fraction of (a) methane and (b) dimensionless temperature along the length of the reactor for quenchless walls (solid lines) and quenching material (dashed lines) for stoichiometric methane-air flames, channel width is 100 μm, wall heating power is 4.187 W/m² K, a dimensionless inlet temperature of 1.5 (reference temperature is 1273.15K) [128].

In addition, radical quenching via surface recombination can be dominated by the diffusion process as the channel width decreases. Accurate modeling of micro-scale combustion at high temperatures needs to include rigorous models of radical quenching mechanism and radical diffusion transport.

Feasibility study of hydrocarbon combustion in a small burner was experimentally conducted by paying attention to thermal and radical quenching [20]. Several wall materials which are not expected to trap radicals are selected based on an earlier analysis [134]. Those wall materials are mounted on metal blocks to form small adjustable gap between them. A standard methane/oxygen torch was placed below the gap and the distance between the walls is reduced until flame quenching. The wall temperature was controlled by heating or cooling the blocks to maintain an inside wall temperature at constant. Results show that quenching distance did not depend on wall materials when the wall temperature is below 500 K whereas those at wall temperature near 1273 K are strongly dependent on the wall materials (Fig. 38) [20]. Therefore, it was concluded that the thermal quenching is dominant at low temperature wall while the radical quenching is dominant at high temperature wall.

Table 5
Radical quenching mechanism along with kinetic parameters [128].

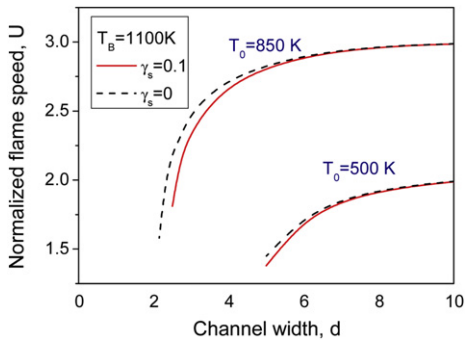| Reactions	Pre-Exponential (S^{-1}) or Sticking Coefficient
1. $CH_3 + * \rightarrow CH_3^*$	0–1
2. $H + * \rightarrow H^*$	0–1
3. $OH + * \rightarrow OH^*$	0–1
4. $O + * \rightarrow O^*$	0–1
5. $2CH_3^* \rightarrow C_2H_6 + 2^*$	10^{13}
6. $2H^* \rightarrow H_2 + 2^*$	10^{13}
7. $2OH^* \rightarrow H_2O + O^* + ^*$	10^{13}
8. $2O^* \rightarrow O_2 + 2^*$	10^{13}
9. $CH_3^* + H^* \rightarrow CH_4 + 2^*$	10^{13}
10. $OH^* + H^* \rightarrow H_2O + 2^*$	10^{13}

Fig. 36. Effect of wall temperature on flame speed in a micro-channel and the competition between thermal quenching and radical quenching [133].
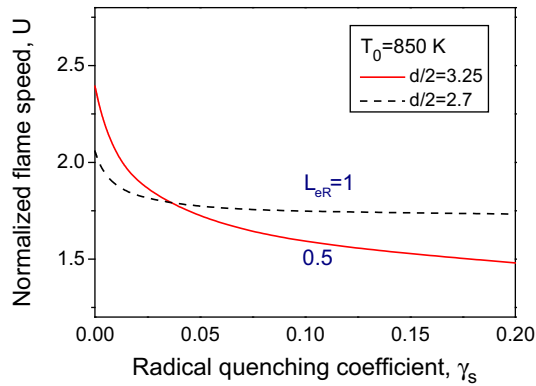
Fig. 37. Effect of radial quenching coefficient on flame speed in a micro-channel with different channel widths and radical Lewis numbers [133].

Effects of thermal and chemical surface–flame interaction on flame quenching are experimentally investigated also by KAIST group [135]. Reactive and inert test plates with three kinds of materials, such as stainless steel, alumina and quartz are chosen for the panels organizing narrow gap. Nearly identical quenching distances are demonstrated at wall temperature at 500 K regardless of wall material and pretreatment, while material and pretreatment sensitivities are confirmed at wall temperature at 1100 K. Trends of the measured quenching distance as a function of surface temperature is discussed in terms of competition between heterogeneous and homogeneous reactions which then affects dominance of radical quenching at the wall in each temperature region.

3.1.5. Weak flame regimes with temperature gradient

As described above, flame structure thermal coupling induces flame bifurcations which exhibits weak flames. Such flames are also observed under the gas-solid thermal coupling in particle laden flames and strained flames under the combined effects of radiation and unequal diffusive-thermal transport (Lewis number effect) in counterflow flames in microgravity. Temperature and reactivity of weak flames are thought to be low in general since they are stabilized
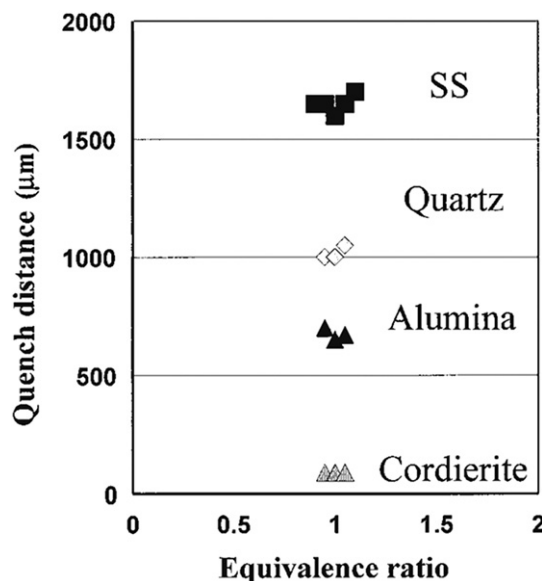

Fig. 38. Quenching distance for different wall materials at wall surface temperature near 1273 K [20].

at near-limit conditions or even beyond the limit due to the coupling effects. However, note that the weak flame can be "stronger" than the normal flames as the case discussed in Section 3.1.3.

Weak flames in micro-combustion systems exhibit various novel aspects since micro-combustion device is under the strong thermal coupling in nature. In this section, characteristics of weak flames in temperature gradient resulting from thermal coupling of flames with thermally thick wall (or wall with prescribed or controlled temperature profile by an external heat source) are reviewed.

Thermal coupling of flames with a micro-channel having prescribed temperature profile is investigated using a fine, straight quartz tube [41,44]. Stationary monotonic positive temperature gradient by an external heater is formed along the inner surface of the tube wall for investigating micro flame behavior under the well-defined temperature profiles at the flow channel. Measured flame responses to varying mean flow velocity at the tube inlet are shown in Fig. 39 [41]. The overall flame response for the same case is examined theoretically and shown to be an S-shaped response as will be shown in Fig. 65 in the Section 3.4.1, which has stable flames in high and low velocity regions and unstable flames in middle velocity region. Flames stabilized in the low velocity region are weak flames while those in the high and middle velocity branches respectively correspond to experimental normal flames and *Flames with repetitive extinction and ignition* (FREI) [41,44], where the latter will be discussed in detail in the Section 3.4.1 together with experimental observations for equivalent phenomena [45,46].

Since the tube wall temperature is prescribed by an external heater, weak flame extinction induced by heat loss due to its insufficient heat generation is not likely to occur. However, the lower limit of weak flame is identified experimentally at very low mixture flow velocity [136] of methane/air mixture. Although a weak flame at a mean flow velocity of 0.2 cm/s was observed, no flame was observed below that flow velocity even with long-exposure time. This result indicates the existence of a lower limit of weak flame, even with heat compensation by external heating. Thus, gas-phase and wall temperature measurements in such conditions are carefully conducted. The temperature difference between flame and tube wall at the flame position, i.e., temperature increase in weak flame, is shown in Fig. 40 [136]. Fig. 40 shows the gradual decrease of temperature difference with the decrease of the mean flow velocity and it is almost zero at mean flow velocity of 0.2 cm/s, where the wall temperature is around 1225 K regardless of mixture composition. Based on the two characteristics of weak flame, i.e., 1) small temperature increase and 2) flame location close to the ignition point, flame temperature at the lower limit of weak flame is considered to correspond to the ignition temperature of
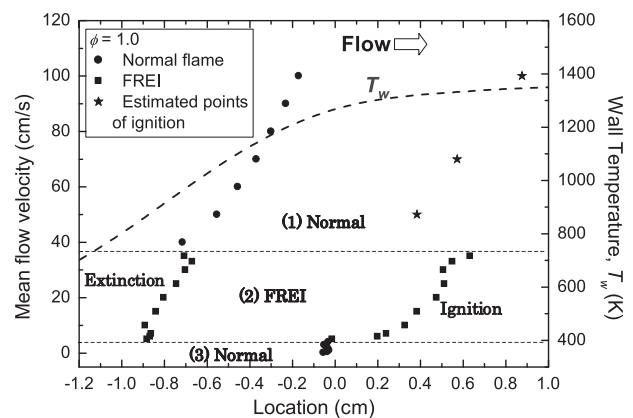

Fig. 39. Measured flame positions and extinction and ignition points of FREI for variable mean flow velocity at equivalence ratio of 1.0. Estimated ignition locations in upper normal flame regime are also indicated [41].

the given mixture. Although ignition and flame propagation have been considered to be separated phenomena in general, stationary propagating flame near the ignition point in weak flame is successfully established in the experiment. Hence, ignition and flame propagation would merge with each other at this extreme condition. This fact also indicates that the general ignition temperature of given mixture, which is independent of the experimental apparatus and methodology, can be expected to be identified with the position of the weakest flame by this methodology.

One-dimensional computations with detailed chemistry and transport properties are conducted for examining the mechanism of the lower weak flame limit [136]. A steady-state flame code [41] based on PREMIX with GRI-mech 3.0 is used. The energy equation, which has a convective heat transfer between gas and wall, is as follows:

$$\dot{M}\frac{dT}{dx} - \frac{1}{c_p}\frac{d}{dx}\left(\lambda A\frac{dT}{dx}\right) + \frac{A}{c_p}\sum_{k=1}^{K}\rho Y_k V_k c_{pk}\frac{dT}{dx}$$

$$+ \frac{A}{c_p}\sum_{k=1}^{K}\dot{\omega}_k h_k W_k - \frac{A}{c_p}\frac{4\lambda Nu}{d^2}(T_W - T) = 0 \qquad (17)$$

Because of the fully developed flow in a circular tube for the case between constant wall heat flux and constant wall temperature, *Nusselt number* of the inner wall surface is assumed to be constant ($Nu = 4$). Fig. 41 shows the computed flame response to the mean flow velocity at equivalence ratio $\phi = 1$. The location of the CH peak is considered to be the flame position. The dashed line with open circles in the figure is the wall temperature profile. The computational flame response showed an ϵ-shaped curve, which has an additional lower velocity branch with the S-shaped curve [41,44]. Based on the stability analysis for the S-shaped curve, the lowest velocity branch here is considered to be unstable. If this assumption is true, the existence of two stable and two unstable solutions in the four regimes can be inferred. Therefore, the existence of the lower limit of the experimental weak flame can be interpreted as the lower limit of the region (3) in Fig. 41 [136].

To further consider the experimental lower limit of the weak flames, variation of the computed temperature difference between the flame and the fixed inner wall surface temperature at the flame position is shown in Fig. 42 [136]. Flame temperature is defined as the temperature of gas at the CH peak. The computed temperature difference becomes smaller with the decrease of mean flow velocity, which agrees well with findings of the experiment. The temperature difference becomes almost zero (Tg − Tw < 1 K) at
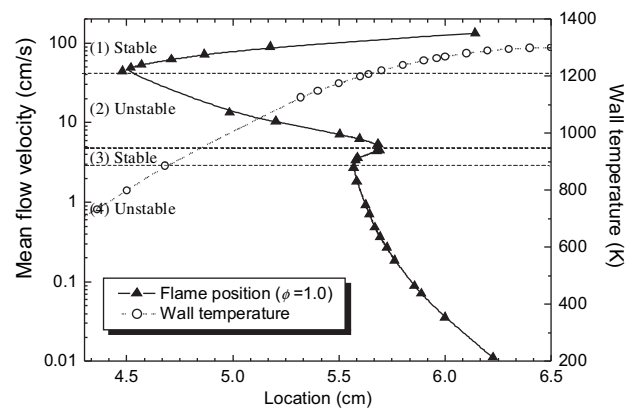

Fig. 41. Computed flame position with mean flow velocity ($\phi = 1.0$) [136].

mean flow velocity of 0.1 cm/s when wall temperature is 1230 K, which quantitatively agrees with the experimental results (1225 K). The lower limit of stable weak flame is considered to be at the midpoint of the lowest velocity branch (regime (4)) in Fig. 41. Since the boundary between the stable and unstable branches is unresolved, stability analysis should be conducted. It should be noted that the extremely small temperature increase does not directly correspond to flame quenching in the low velocity regime; however, the conventional reaction with intense heat release no longer occurs in regime (4), even though the heat loss from the flame zone is compensated by the external heating.

If thermal quenching does not occur at the lower limit of the stable weak flame, what is the possible mechanism for the extinction of weak flame? It was considered that the cause of such limit to be related to the dominance of diffusive mass dissipation over the convective mass transfer in the extremely low velocity regime. Based on this assumption, the effect of diffusion on the lower limit of weak flame is examined by comparing the convective and diffusive mass fluxes of OH in the case of high and low velocity regimes. OH is chosen because it is one of the key radicals for the initiation of chain-branching reactions as well as its high diffusivity. Mass transport by convection is dominant in the case of the high velocity regime (not shown), which is similar to the conventional flame. Meanwhile, diffusive mass flux is dominant at mean flow velocity of 1.82 cm/s in the low velocity region as shown in Fig. 43. This means that the effect of diffusion on total mass transport
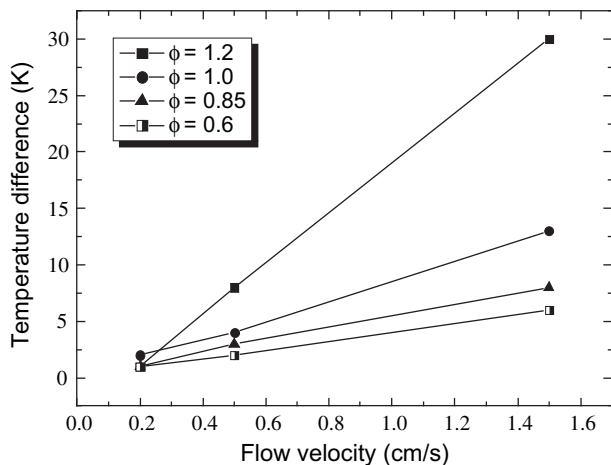

Fig. 40. Measured temperature difference between the flame and the inner surface of the tube wall at the flame position [136].
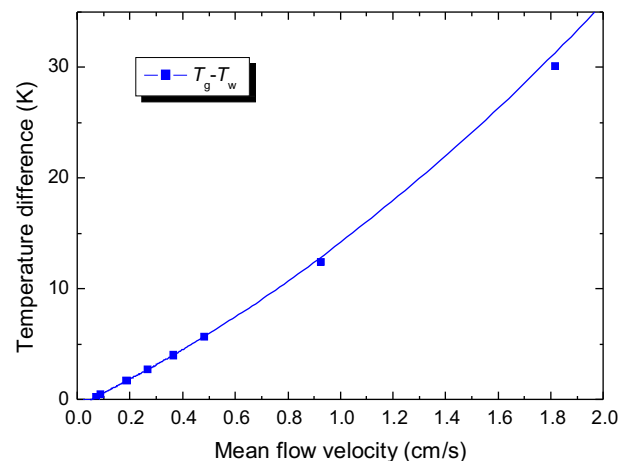

Fig. 42. Computed temperature difference between the flame and the inner surface of the tube wall at the flame position ($\phi = 1.0$) [136].
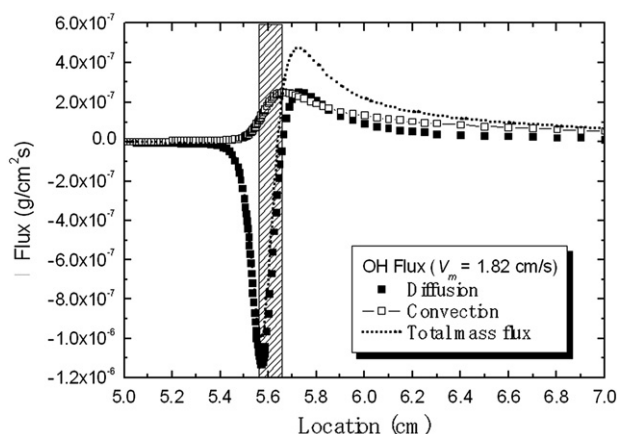
Fig. 43. Convective, diffusive and total mass flux of OH at mean flow velocity of 1.87 cm/s [136].

increases at the extremely low flow velocity. Furthermore, the contribution of negative total mass flux in the low velocity regime is larger than that in the high velocity regime, and the absolute value of the negative total mass flux is larger than that of the positive total mass flux in the same figure. Note that the negative value means that OH moves in the upstream direction. Since the radical species represented by OH, which is vital for the chain-branching reactions, diffuse out from the reaction zone in both the downstream and upstream directions, the number of collisions and the rate of production of chain carriers are both considered to be low. Thus, the flame temperature may become lower with the decrease of mean flow velocity. Existence of the weakest flame and its mechanism is also investigated by flames under the reduced pressure [136,137].

So far, weak flames in temperature gradient are found to be an effective way for identifying the lower limit of weak flames. More practically, it is equivalent to the lowest ignition temperature of given mixture at reactor pressure and given residence time. In fact, some studies are conducted for elucidating comprehensive ignition characteristics of other hydrocarbon fuels using weak flame regimes in the micro flow reactor with controlled temperature profile. Oshibe et al. [138] examined ignition and combustion characteristics of stoichiometric DME/air mixture using the micro-reactor and demonstrated that the existence of the steady double luminous flames in weak flame region as well as stable flames in high velocity region and unstable flames in middle velocity region. Based on gas sampling analysis and computation with detailed chemistry and transport, it was concluded that these double weak flames are separated multi-stage oxidations of the DME/air mixture (Fig. 44) [138]. Furthermore, the identical method was applied for n-heptane/air mixture and separated stationary triple weak flames were identified [139]. It is expected that these steady-state multiple flame phenomena can be utilized for examining general transient ignition process in modern compression ignition

engines since multi-stage oxidations in compression ignition can be visualized or converted to the stabilized multiple flames in the micro flow reactor.

3.2. Catalytic micro-combustion

Although the use of catalysis offers versatility to promote chemical reactions in various industrial purposes, catalytic combustion, i.e., catalytic exothermic reaction has not been a majority of them since thermal runaway is hard to control in ordinary large scale applications. In micro-scale applications, however, this weakness can be turned into one of the significant advantages for sustaining stable exothermic reactions with other advantages, such as immobile heat release zone, no quenching distance, moderate reaction temperature and clean emission.

In this section, some new fundamental aspects of catalytic combustion, design, operation, modeling and diagnosis which are newly highlighted for micro-combustion application purpose are reviewed.

3.2.1. Stability and flammability limits of catalytic combustion

Flame stability, flammability limit, ignition and extinction phenomena are typical fundamental subjects of combustion science. Being associated with those subjects, "flammability limit" of self-sustaining catalytic combustion are investigated in very wide range of physical parameters using spiral counterflow Swiss-roll burners by the USC combustion physics laboratory [140]. Their major findings are low temperature catalytic reaction and flammability limit boundaries which are unsymmetrical to the stoichiometric condition and extremely wide in fuel rich condition. A 3.5-turn square spiral counterflow Swiss-roll burner with $70 \times 70 \times 50$ mm tall having 3.5 mm channel width was constructed and bare platinum strips with approximately 30 cm^2 in total area were placed at the center of the burner. Propane-air mixture and other diluents were used and both catalytic and gas-phase combustion were tested in the experiments. Fig. 45 [140] shows the lean and rich extinction limit boundaries of catalytic and gas-phase combustion on Reynolds number − equivalence ratio plane, where Reynolds number (Re) is defined by the area-averaged inlet mixture velocity at the ambient condition. Notable feature in the figure is very wide self-sustained boundary of catalytic combustion, which has reached down to very small Re close to unity, being unsymmetrical to the stoichiometric condition. Its difference with that of gas-phase combustion is remarkable especially in low Re and fuel rich conditions. For example, gas-phase reaction cannot be sustained at $Re < 40$, while catalytic combustion with NH$_3$ conditioned catalysis can be sustained at $Re \simeq 1$, where maximum temperature record at the burner center is very low (it is 350 K at $Re = 1.2$). It is also noted that at $Re < 15$, lean extinction limit of catalytic combustion is at richer side of the stoichiometric condition. Rich limit of catalytic combustion was very rich, e.g., $\varphi_{lim} > 40$ at $Re = 15$. This fact suggests that catalytic flammability

Fig. 44. CH-filtered, long-exposure images of double weak flames (dashed circles) in a channel with an inner diameter of 2 mm for stoichiometric DME/air mixture at channel inlet velocity = 2 cm/s. Flow direction is from the left to the right. Channel wall temperature is increasing from the room temperature up to 1300 K in a flow direction. Dotted lines are inner surface of the channel wall. Dual weak flames are stabilized at the wall temperatures 1054 K and 1198 K. Gas sampling analysis confirms cool flame reaction starts further upstream of the first weak flame where the wall temperature is around 600−700 K. Bright luminescence in the downstream channel wall is radiation from the high temperature wall due to an external heat source [138].
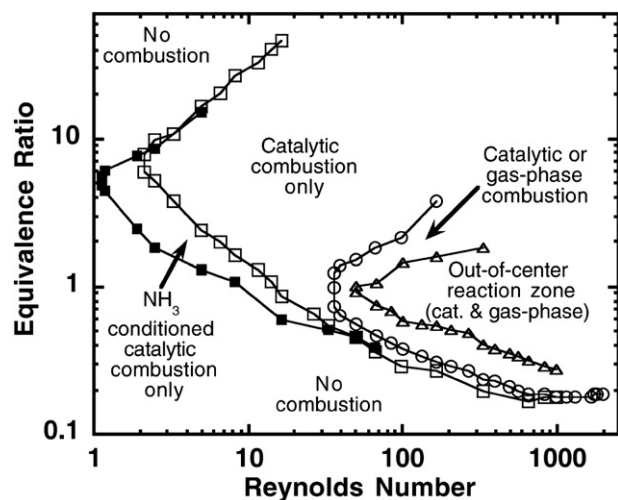
Fig. 45. Stability boundaries of catalytic and gas-phase combustion on Reynolds number - equivalence ratio plane. Reynolds number is defined by the area-averaged inlet mixture velocity at the standard state. Swiss-roll burner is made of Inconel [140].

limit is totally governed by the different mechanisms with that of gas-phase combustion which will be discussed later in this section.

Fig. 46 [140] shows maximum burner temperatures as a function of *Re*, which are recorded at the burner center along the extinction limits indicated in Fig. 45. For both catalytic and gas-phase combustion, the lowest temperatures for self-sustaining reaction increase with the increase of *Re*. It is noted that the lowest temperature for self-sustaining catalytic combustion is 350 K at *Re* = 1.2, when NH$_3$ conditioned catalysis was used. Meanwhile, the lowest temperatures for self-sustaining gas-phase reactions are far above 900 K. Here, it is emphasized again that those remarkably low self-sustaining temperatures for catalytic combustion at "lean" limits were accomplished at the rich side of the stoichiometry (See Fig. 45).

In fact, low temperature self-sustaining catalytic combustion at the rich side of stoichiometry has been reported earlier by using a simple catalytic channel [141]. The lowest self-sustaining temperature curve, which is discontinuous at stoichiometric condition and required temperature drops by almost half there, was demonstrated by varying fuel-to-oxygen ratio in a methane/nitrogen/oxygen mixture (Fig. 47). The figure shows extinction
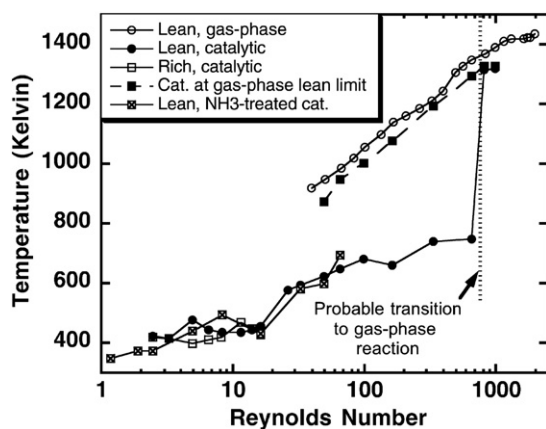
limits and required temperatures for self-sustaining reaction of N$_2$-diluted methane/oxygen mixtures in a non-adiabatic, 1 mm diameter catalytic channel at representative operating condition of mixture velocity = 0.06 m/s and heat transfer coefficient from the outside of the channel wall to the ambient is 5 W/(m^{2}K). Channel wall was assumed to be thermally thin. The limit temperatures are higher than 1200 K in fuel lean condition while those at fuel rich condition are lower than 800 K and decreasing down to 600 K as shown in the figure. This high/low limit temperature at fuel lean/rich side and its discontinuity at the stoichiometry is interpreted in terms of inhibition of methane absorption by O(s) surface coverage [142]. The surface of catalyst is covered by O(s) at low temperatures in CH$_4$/O$_2$ system due to the higher sticking probability of O$_2$ compared with CH$_4$. With the increase of surface temperature, catalyst reaches to a point at the adsorption/desorption equilibrium of oxygen shifts to desorption, resulting in bare surface where CH$_4$ can be absorbed. Abstraction of H atom leads to adsorbed C(s) and H(s) atoms which immediately react with O(s) atoms to form CO(s) and OH(s), eventually leading to relatively fast formation of H$_2$O and CO$_2$. In addition, immediate desorption of H$_2$O and CO$_2$ finally leads to larger numbers of bare surface sites available for further reactant absorptions. Therefore, inhibition of CH$_4$ adsorption is harder to occur under the fuel rich condition where O$_2$ is a deficient reactant. This was clearly shown by drastic change of surface coverage profiles of the stoichiometric (fuel/oxygen = 0.5) and slightly rich of the stoichiometric (fuel/oxygen = 0.52) as shown in Fig. 48 [141]. In case of fuel/oxygen = 0.5 (top), bare surface site, Pt(s) occupies catalyst surface in the region of significant reaction from 0.002 to 0.005 m where temperature is high and O(s) surface coverage changes inversely such that almost all sites are covered by either Pt(s) or O(s). For the slightly fuel rich case (fuel/oxygen = 0.52), Pt(s) at the leading edge of the catalyst (0.001 m) is nearly twice as high and the CO(s) rather than O(s) covers the surface because oxygen is deficient reactant in this case. CO(s) is less effective than O(s) at suppressing methane absorption [142] and allows self-sustaining catalytic combustion to proceed at lower temperatures than stoichiometric and lean mixture cases.

Additional advantage of fuel rich operation for limiting formation of metal oxides is discussed in [143]. Metal oxides are often volatile than the reduced metal and loss of Pt in the form of PtO$_2$ has a significant effect on catalyst deactivation under fuel lean operation. Under fuel rich conditions, however, volatility of the catalyst is not a significant deactivation mechanism, allowing long catalyst life and broad choice of catalyst materials, without constraints regarding oxide volatility.

Fig. 46. Maximum burner temperatures at the extinction limits recorded at the burner center. When NH$_3$-treated catalyst is used, self-sustaining catalytic combustion of 350 K at *Re* = 1.2 was attained [140].
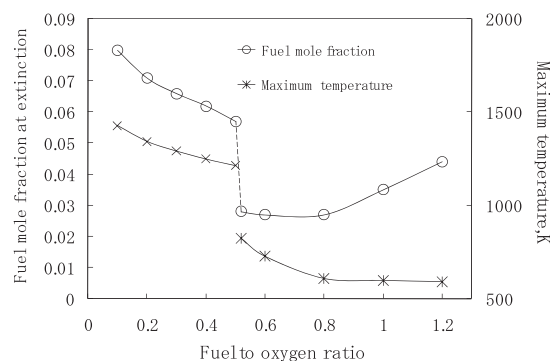

Fig. 47. Lower self-sustaining limits of fuel concentration and operation temperature for N2-diluted methane/oxygen mixtures in a Pt catalyst channel (1 mm in diameter) at the averaged inlet mixture velocity 0.06 m/s under heat loss condition. Heat transfer coefficient between outer wall to the ambient is 5 W/(m^2 K) [141].
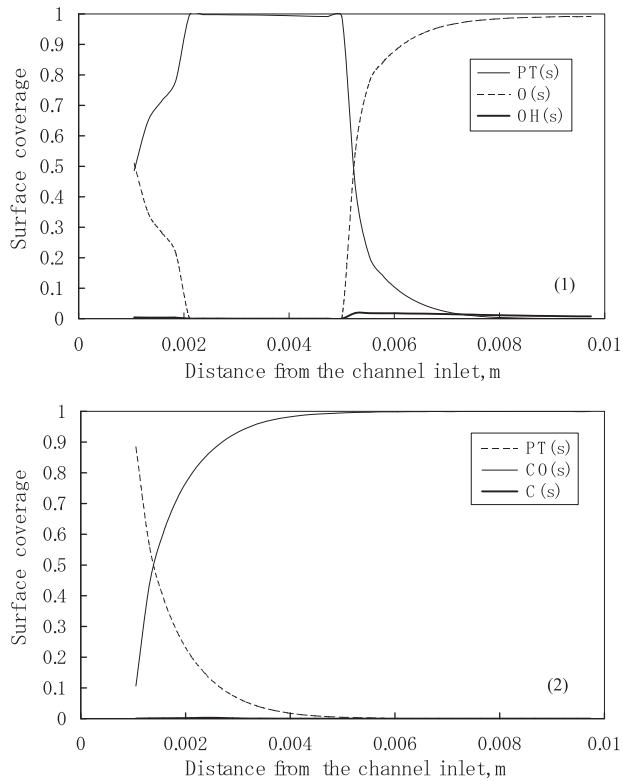
Fig. 48. Surface coverage profiles of the stoichiometric (upper figure: fuel/oxygen = 0.5) and slightly rich of the stoichiometric (lower figure: fuel/oxygen = 0.52) [141].

As often observed in gaseous combustion, dual-limit behavior, i.e., heat loss induced extinction limit at low mixture flow rate and blow-off limit at high mixture flow rate are reported for catalytic self-sustaining combustion of methane/air mixture in a 1-mm diameter Pt channel [141].

3.2.2. Interaction/transition between gas-phase and surface reactions

Another subject, which is also relevant to operation boundary of catalytic reaction, is interaction/transition between surface and gas-phase reactions (or it is termed hetero-/homogeneous reaction interaction). Although general stability characteristics including interaction and/or transition between them have not been fully elucidated, this subject has been addressed by several studies [144,145] for macro-scale applications of catalytic partial oxidation and NOx reduction. Schwiedernoch et al. [146] showed that inclusion of gas-phase reaction modeling is required for capturing reaction of a mixture close to stoichiometry while surface reaction modeling alone is enough to reproduce phenomena for fuel lean methane/air mixture in a macro-scale honeycomb monolith catalytic reactor. Norton et al. [147] fabricated a single-channel catalytic micro-burner and found that self-ignition, gas-phase combustion in parallel with catalytic combustion and audible "whistle" together with temperature bifurcation for hydrogen/air mixture.

Stability diagrams showing evident extension of stability limits due to gas-phase chemistry were presented for 10-mm-long, 1-mm height Pt-coated catalytic plane channel numerically [148]. A full-elliptic 2D code was used to model the interaction between gas-phase and surface reactions in the channel. Surface reaction scheme of Deutschmann et al. [149] and gas-phase C1 reaction scheme of Warnatz et al. [150] were employed. Heat conduction in the wall (wall thermal conductivity, k_s, and thickness, $\delta = 0.1$ mm),

heat loss from outer wall to the ambient (heat transfer coefficient, h), and inlet flow velocity, U_{in} were parameterized for methane/air mixture of $\phi = 0.4$ at inlet temperature 600 and 700 K. Fig. 49 [148] indicates stability diagram constructed by varying external heat transfer coefficient, h, and the inlet flow velocity, U_{in} when wall thermal conductivity, $k_s = 2$ W/mK. Blow-off limit at high inlet flow velocity due to insufficient residence time and heat loss induced lower limit at low flow velocity are observed. Note that blow-off limits obtained by considering gas-phase chemistry were extended both for $T_{in} = 600$ K and 700 K at 5 bar. These limit extensions are interpreted by gas-phase homogeneous reaction occurred along the center of the channel, at slightly downstream of the region of surface reaction as shown by streamwise profiles of methane conversions in gas-phase and at the catalyst surface in Fig. 50 [148]. Cases (a)–(d) in the figure respectively correspond to the points A–D designated in Fig. 49. For cases (a)–(c), methane conversion profiles by surface reaction gradually shift to the downstream with the increase of the heat transfer coefficient, h, which means gradual decrease in representative temperature and reaction rate. In these cases, local peak temperatures of the catalyst surface are 1460–1380 K in the high reaction rate regions (figure not shown) which are high enough to sustain gas-phase reactions in methane/air mixture. Thus, in all cases here, surface reaction occurred at the catalyst leading edge which is followed by gas-phase reactions at slightly downstream side. Effect of wall thermal conductivity is also investigated. For low thermal conductivities (<2 W/mK), the reduced upstream heat transfer hinders catalytic ignition and causes blow-off. Thus, stability limits at low thermal conductivities are narrower at higher inlet velocities. Meanwhile, at large thermal conductivities, the limits are heat loss induced and hence are wider at higher inlet velocities.

Another computational study reported phenomena with similar tendencies containing interaction between gas-phase and surface reactions for hydrogen/air mixture at ambient pressure and temperature [151]. Both gas-phase and surface reactions are computed in a 10-mm-long, 1-mm-diamter cylindrical Pt channel under the assumption of thermally thin channel wall. Gas-phase reaction mechanism consists of 9 species and 19 reactions, which are adopted from the mechanism presented by Miller and Bowman [152] and surface reaction mechanism by Deutschmann et al. [142] were employed. Convective and radiative heat losses from the outer

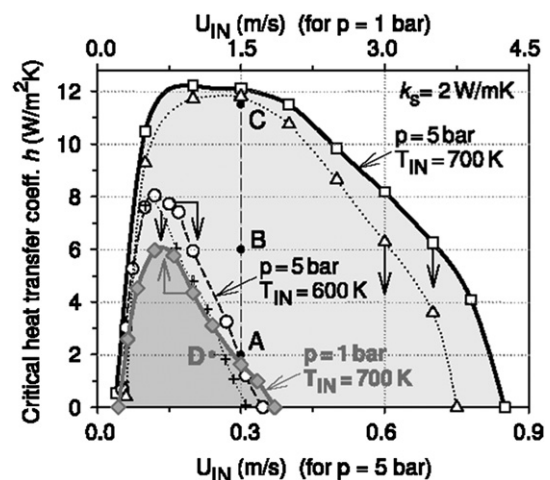**Fig. 49.** Stability diagrams of critical heat transfer coefficient and inlet velocity at $p = 5$ bar (squares: TIN = 700 K, triangles: TIN = 700 K without gas-phase chemistry, circles: TIN = 600 K, crosses: TIN = 600 K without gas-phase chemistry), and at $p = 1$ bar (filled diamonds: TIN = 700 K). The stable regimes for the 700 K cases are shown by the shaded areas [148].
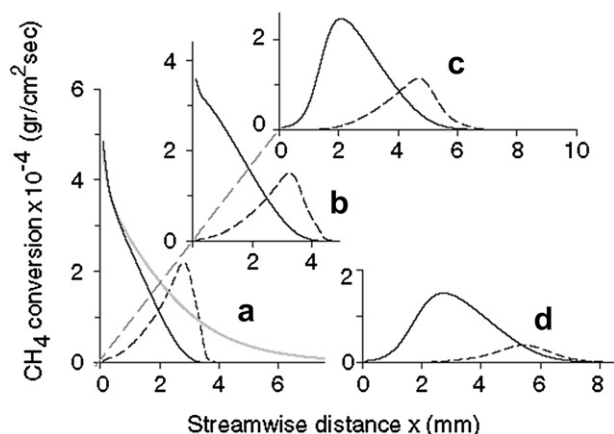
Fig. 50. Catalytic (solid lines) and gaseous (dashed lines) methane conversions for the four cases indicated in Fig. X5: Cases A, B, C ($p = 5$ bar, $T_{IN} = 700$ K, $U_{IN} = 0.3$ m/s) and Case D ($p = 1$ bar, $T_{IN} = 700$ K, $U_{IN} = 1.2$ m/s). The gray line in (a) refers to pure catalytic combustion [148].

wall surface to the ambient were considered by convective heat transfer coefficient of 20 W/m^{2}K and wall emissivity ϵ of 0.5, respectively. Three different reaction modes by different combinations of the gas-phase and surface reaction mechanisms were examined to clarify and highlight the effects of heterogeneous reaction. Fig. 51 [151] shows computed temperature and OH concentration distributions for stoichiometric hydrogen/air mixture at an inlet flow velocity of 2 m/s by three reaction modes: both gas-phase and surface reactions, gas-phase reaction-alone and surface reaction-alone. Due to highly reactive nature of hydrogen-air mixture, comparatively rapid temperature rises close to the channel inlet were attained in all cases. However, some differences were seen in those three cases. Most prompt temperature increase was seen in gas-phase reaction-alone case, not in both gas-phase and surface reaction case, which implies that gas-phase reaction is inhibited by catalyst. This tendency can be more evidently seen from the absence of OH in the vicinity of channel inlet, especially in a region close to catalyst wall for both gas-phase and surface-reaction case. OH concentration is higher at wall vicinity for surface reaction-alone case than that for both gas-phase and surface reaction case, and more significantly, OH are only seen in

the vicinity of catalyst wall for surface reaction-alone case because chemical reaction only occurs on the wall in this case. Fuel consumption and product formation also indicated that the inhibition of gas-phase reaction by catalyst (although figures not shown here) [151]. Note that reaction inhibition by catalyst is sensitive to thermal boundary condition at the wall.

Roles of gas-phase and surface reactions in Hydrogen reactions which are similar to that already indicated in Fig. 50 for methane/air mixture is confirmed in Fig. 52, where hydrogen mass fraction profiles along the channel central axis for different inlet velocities are shown [151]. For smaller inlet velocities, the fuel concentration sharply decreases close to the channel inlet due to the gas-phase reaction. At higher inlet velocities, for example at 6 and 10 m/s, the hydrogen consumption indicates two different slopes. The first slope is gradual since hydrogen is transported to the wall by diffusion where surface reaction is dominant in the region. Meanwhile, the second slope is steeper since intense gas-phase reaction occurs in the channel center region. Note that the case for inlet velocity of 12 m/s, where flow residence time is not enough for sustaining gas-phase reaction in the channel. This means gas-phase reaction is blown out from the tube if the inlet velocity exceeds 10 m/s, when sharp decrease in hydrogen conversion ratio is also observed. In fact, experimental and numerical study on catalytic combustion in a Platinum micro-channel is conducted by focusing the gas-phase combustion occurred at the exit of the channel [153]. Temperature and major species measurements with Raman scattering and LIF (O$_2$, N$_2$, H$_2$O, H$_2$ and OH) are made for examining transition between surface and gas-phase reactions. Regime diagram of surface and gas-phase reactions as well as suppression of surface reaction in smaller diameter catalyst channel (200 μm) is reported.

The effect of channel diameter is also essential to the interaction between gas-phase and surface reactions. Since characteristic diffusion time scale is proportional to the square of channel diameter, the decrease in channel diameter leads to weaker gas-phase reaction through the fuel comsumption by surface reactions. Hence, OH concentration along the center axis in gas-phase shifts upstream and sharply decreases with the decrease of tube diameter. On the contrary, blow out of gas-phase reaction is easy to occur when channel diameter is too large, where promotion of gas-phase reaction through high temperature and radicals produced by surface reaction is scarcely expected. Eventually, optimum channel

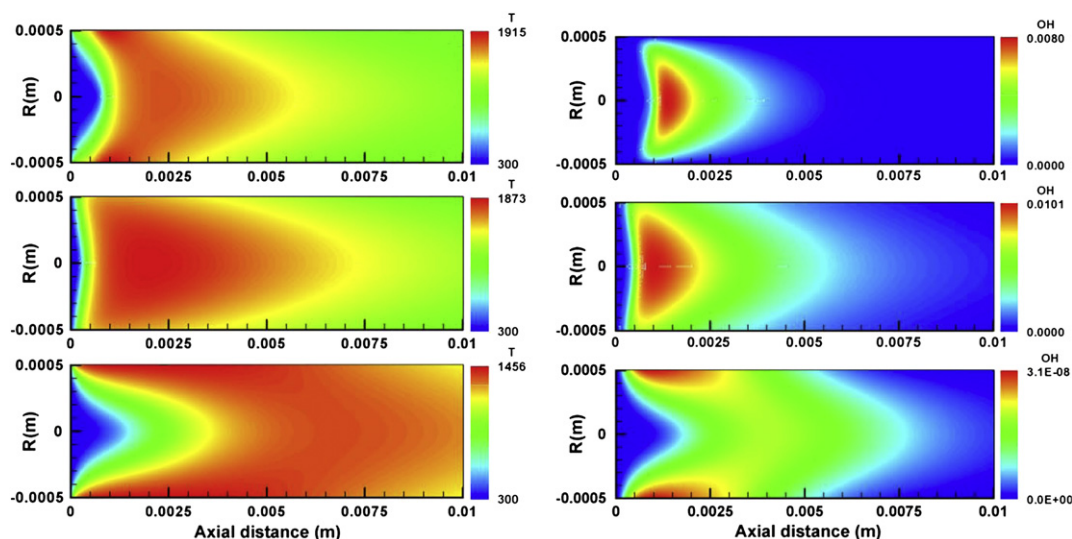

Fig. 51. The computed temperature and OH concentration distributions for three different reaction models; upper: both homogeneous and heterogeneous reactions, middle: homogeneous reaction-alone, and lower: heterogeneous reaction-alone [151].
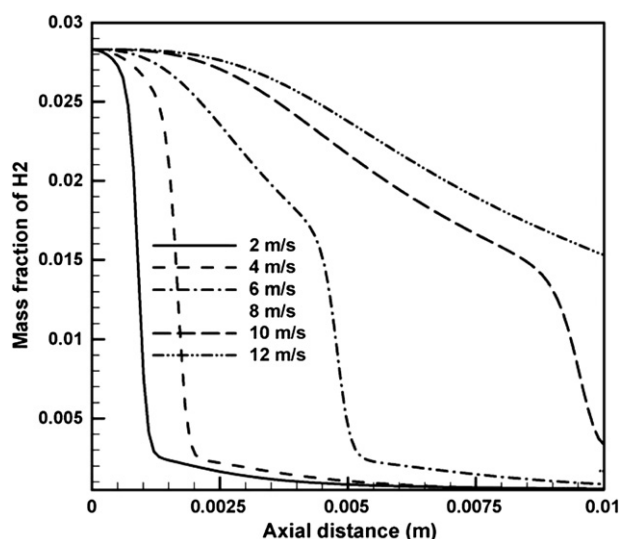
Fig. 52. Fuel (Hydrogen) mass fraction profiles along the central axis of 1-mm-diamter cylindrical Pt channel for different inlet velocities [151].

diameter exists for intense gas-phase reaction as shown by blow-off limits as a function of channel diameter [151] (not shown here). By summarizing the above discussion, overall picture of gas-phase and surface reaction interaction was divided into three types as shown in Fig. 53; type I where gas-phase reaction exceeds surface reaction, type II where gas-phase reaction is inhibited by surface reaction to some extent but they both coexist, and type III where surface reaction is dominant [151]. Those three types are indicated in the figure on the inlet flow velocity and channel diameter-plane as regions I, II and III. Line A in the figure corresponds to the blow-out limits of gas-phase reaction denoted above. Above the line B, gas-phase reaction is inhibited and has no effects on the phenomena. Since hydrogen/air mixture is led to light-off even at room temperature, no lower velocity limit exists in the figure. However, existence of upper limit of surface reaction for hydrogen/air mixture must be still open question although no remarks were made on this issue. On the other hand, for mixtures with moderate surface reaction rate, for example, methane/air mixture, have both lower and blow-off limits as discussed in the above [141,148]. For comprehensive understandings on the limit behavior of catalyst (or "flammability" of surface reactions) including its interaction with gas-phase reactions, further investigations at intermediate and lower catalyst temperatures are required, particularly for hydrocarbon fuels which are promising for micro-power generation purposes. Specific characteristics of catalytic combustion induced by discontinuous lowest self-sustaining temperature at the stoichiometry, complicated interaction of surface reaction with gas-phase reaction, different temperature levels, etc, will lead to wide variety of new fundamentals on reaction dynamics in this area.

3.2.3. Ignition of catalytic reaction

Ignition or light-off of catalytic reaction is another key subject of catalytic micro-combustion system. As the vital role of detailed reaction modeling for understanding gas-phase combustion, detailed surface reaction modeling, coupled with transport at gas–surface interface, plays significant role for understanding catalytic ignition. Significant role of adsorption-desorption on catalytic ignition was presented in one of the early numerical studies [142], though it was not addressed to the micro-power generation. They showed behaviors of catalytic ignition temperatures as functions of fuel concentrations for methane/oxygen/nitrogen and CO/air mixtures on Pt, and hydrogen/oxygen mixture

on Pd. To determine catalytic ignition temperature, mixture initially at room temperature is supplied to either a catalytic wire in a tube flow or a catalytic foil in a stagnation flow. Then, temperature of the catalyst is increased by a stepwise increase of electric current applied to the catalyst for resistive heating. When it reaches ignition temperature, catalyst temperature rapidly rises due to the heat release by surface reactions. Results for the three different mixtures clearly indicate two kinds of opposite tendencies of ignition temperatures. The ignition temperature decreases with increasing methane/oxygen ratio, while those for CO/air and hydrogen/oxygen mixtures increases with increasing fuel to oxidizer ratios. Those results are interpreted based on the surface coverage of the catalyst below and above the catalyst ignition temperature. For methane/oxygen/nitrogen mixture, oxygen, O(s), primarily covers catalyst surface below ignition temperature, since sticking coefficient of oxygen is larger than that of methane. However, adsorption/desorption equilibrium of oxygen shifts to desorption with the increase of temperature and then carbon monoxide, CO(s), becomes dominant surface species at fuel rich condition when the catalyst surface is above ignition temperature. On the other hand, dominant surface species are fuels, i.e., CO(s) and H(s) below ignition temperature respectively for CO/air and hydrogen/oxygen mixtures, and significant increase in bare catalyst surface site, Pt(s), are seen above ignition temperature. This explains the two kinds of opposite tendencies of ignition temperature since catalytic ignition is governed by the availability of sufficient uncovered surface sites. Notable low ignition temperatures are seen at extremely fuel rich methane/oxygen/nitrogen mixture and fuel lean CO/air and hydrogen/oxygen mixtures. Such characteristics might motivate various ignition strategies for catalytic micro-combustion systems as well as self-ignition of hydrogen/oxygen mixture at room temperature. In brief, fuel rich conditions for hydrocarbon fuels and fuel lean conditions for hydrogen are advantageous for low temperature ignition of catalytic reactions. Such phenomena can be seen in some studies [140,141] which were already overviewed. Detailed earlier studies on catalytic ignition were also conducted [154].

By taking the advantage of the capability of hydrogen addition for low temperature ignition, hydrogen assisted self-ignition of
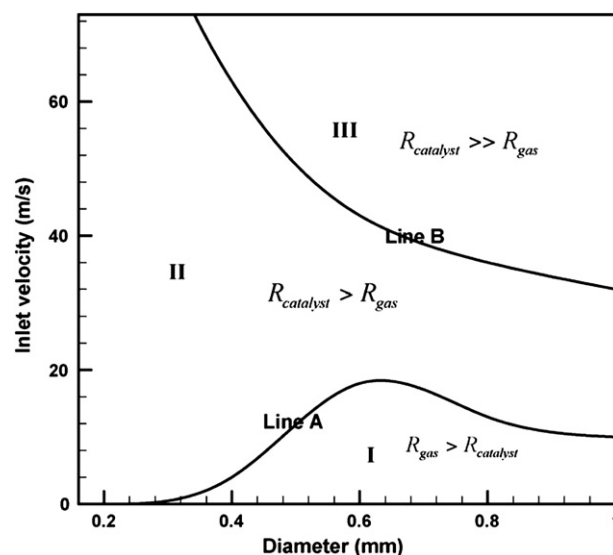

Fig. 53. Three regions showing overall picture of gas-phase and surface reaction interactions. Region I: gas-phase reaction dominant; Region II: gas-phase reaction inhibited by surface reaction but they both coexist, Region III: surface reaction dominant [151].

methane/air [149] and propane/air [155] mixtures were investigated. Norton and Vlachos [155] pointed out that concept of hydrogen assisted self-ignition of hydrocarbon can be applied to catalytic micro-scale devices without ignition sources. Propane/air mixture with hydrogen addition is supplied to rectangular channel (50 × 10 × 0.25 mm) with Pt deposited wall. Hydrogen mole fraction in the propane/air/hydrogen mixture is gradually increased by keeping both the propane/air equivalence ratio and total volumetric flow rate of the mixture at constant. Result indicates that very little hydrogen conversion is observed by GC measurement during low hydrogen content, and when hydrogen mole fraction exceeds 0.002, the temperature starts increasing (See Fig. 54). Then the reactor temperature gradually increases with increasing hydrogen mole fraction until around 0.03, and ignition occurs at 0.036 with an out-of-scale rapid increase in temperature. Nitrogen/air/hydrogen mixture was also used for examining interaction between propane and hydrogen by replacing propane in the mixture by nitrogen. As can be inferred from self-starting nature of hydrogen/air mixture at extremely fuel lean condition (not shown here), nearly complete conversion of hydrogen is confirmed from the small hydrogen mole fraction by GC, and significant temperature increase is seen in all cases as well. This clearly shows that propane plays inhibitory role on the hydrogen reactions at small hydrogen fraction, while sufficiently high hydrogen fraction leads to effective activation of catalytic reactions.

More practical approach is conducted to identify the effective ignition strategies for simple catalytic channel with heat conducting wall numerically [156]. Propane/air mixture is chosen. Three strategies such as pre-heating of feed mixture, resistive heating of the whole channel and local resistive heating are compared during transient and steady-state operations. Preheated feed temperature, supplied power for resistive heating and channel wall thermal conductivity are varied as essential parameters. Maximum wall temperature, axial profiles of gas-phase temperature, time required to reach steady-state, ignition time and total fuel leakage during heating-up phase are examined. Since the local catalytic reactivity is governed by local temperature, obtained results are clearly interpreted in a straightforward manner in terms of catalyst temperatures although complicated response is observed. Fig. 55 [156] is an example of temporal variation of gas-phase temperature profiles for three kinds of channel wall thermal conductivities; 2, 20 and 200 W/mK, which respectively model typical values for common materials such as ceramic, steel and copper. Temporal variations after the supply of preheated mixtures which are slightly (~5K) higher than the respective ignition temperature identified in advance (not shown), clearly demonstrate that back-end ignition and progressive movement of reaction zone to the upstream are observed for the low wall thermal conductivity case. Meanwhile,
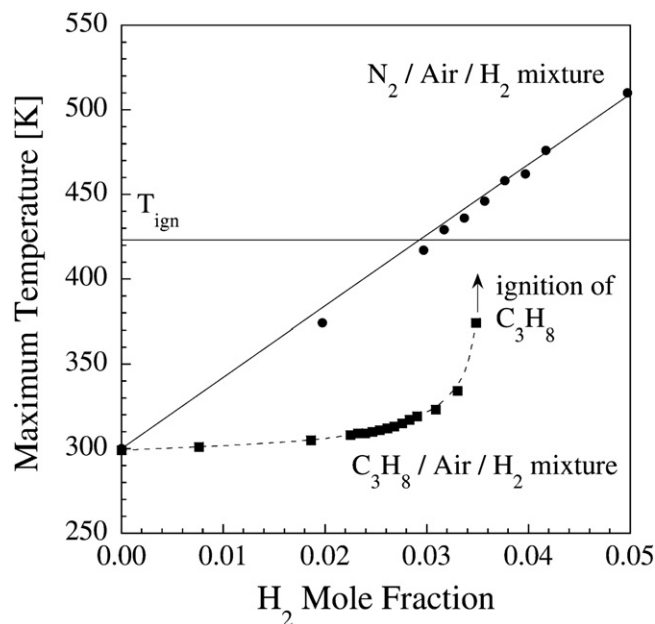

Fig. 54. Maximum reactor temperature of a propane/air mixture at $f = 0.77$ (squares) versus the hydrogen mole fraction, and a mixture where propane has been replaced with nitrogen (circles). The straight line is an overall energy balance fit to the data. The catalytic ignition temperature of propane/air of $f = 0.77$ is shown as a horizontal line [155].

uniform temperature distributions and their uniform increases are seen for the highly conducting materials. Required time to reach steady-state is longer for higher wall thermal conductivity cases because of larger total heat loss to the ambient through the wall with higher thermal conductivities. Electric resistive heating for whole channel as well as localized heating are examined for the same system. Note that the localized heating here denotes applying the equal amount of the electric power for the whole channel resistive heating into the 1/5 of the channel to attain higher localized temperature. The localized resistive heating at the front-end of catalytic section is found to be slightly effective for improving total leakage of supplied fuel than that of the whole channel heating. Although it is not explicitly mentioned in this literature, larger ratio of heating localization, for example, concentrated heating to the smallest possible fraction of catalyst must be very effective to initiate strong local reaction. Besides low temperature ignition, catalyst localization on better conversion performance is also conducted. Multi-segment catalyst disposition is numerically examined for hydrogen/air mixture in a 1-mm
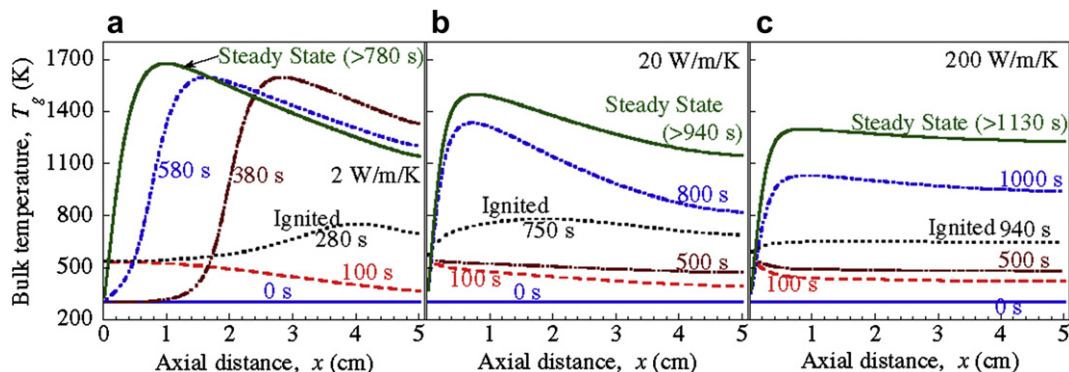

Fig. 55. Temporal evolution of bulk gas temperatures for the three cases with inlet temperatures (540, 555, and 582 K for 2, 20, and 200 W/m/K) exceeding the ignition temperatures by 5 K. Back-end ignition occurs for case (a), middle of the reactor ignition for case (b) and front-end ignition for case (c) [156].
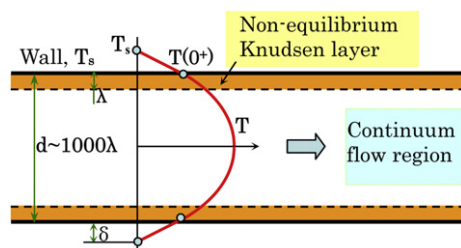
Fig. 56. Non-equilibrium model in slip regime.

height micro-channel [157]. By fixing total catalyst length at 10 mm in a 30 mm long reactor, 2, 5 and 10 segmentations are compared in terms of fuel conversions. Multi-segment catalyst showed better performance than the single catalyst by helping surface reactions to maintain a high wall temperature and by reducing the inhibition effect of the catalyst on gas-phase reaction between catalyst segments.

Effects of various parameters such as operating pressure, wall thermal properties, flow condition, gas-phase chemistry and radiation on start-up characteristics of catalytic microreactors were examined numerically [158].

Catalyst pretreatment is common strategies for achieving desirable catalyst ignition characteristics. Catalyst activation at lower temperatures for hydrocarbon fuels were attempted by using NH_3 pretreatment [140]. In fact, this technique is applied for low temperature catalytic "plastic" combustor system which produces electric power [159] with so called micro-heat engine [160]. This micro-heat engine converts thermal power to mechanical power through the expansion and compression of a two phase working fluid. Then the mechanical power is converted into electrical power through the use of a thin film piezoelectric generator [160]. Room temperature start at 293 K for DME in Platinum pellet catalytic reactor is also achieved by DME feed followed by mixture supply [161].

3.3. Non-equilibrium combustion

As the reactor and combustor scale further decreases and becomes comparable to a magnitude (e.g. the pore size in solid fuel cells is in the order of $1-10$ μm) of two orders of mean free path (approximately 0.1 μm for air at one atmospheric pressure), the

consider the non-equilibrium effects (Fig. 56). Flows in the micro chemical reactors fall mostly into this regime. Therefore, the slip effects in modeling heterogeneous reaction or combustion systems like catalytic reactors [155], solid oxide fuel cells [163], fuel reforming, and combustion synthesis of thin films become important especially at low pressures or small scales.

As shown in Fig. 56, when the length scale of the flow approaches 10^3 the gaseous mean free path, the wall temperature, $T(s)$, and the wall temperature outside of the Knudsen layer $T(0^+)$ are not equal $(T(0^+) \neq T(s))$. The Knudsen layer is called the slip regime $(Kn = 0.001-0.1)$. For example, a catalytic micro-reactor working at 1000 K and 1 atm, the Knudsen number of 10^{-3} approximately corresponds to 300 μm. In this regime, velocity, temperature, and species slips across the Knudsen layer have to be corrected in applications of existing continuum models. The existence of velocity and temperature slips in heat transfer systems has been extensively studied for the development of microfluidic systems in MEMS [164,165]. However, very limited work emphasizing non-equilibrium transport has been done in micro-scale reactive systems [128,155] especially for concentration slips [52,53]. In fact, the temperature slip in micro reactive systems will not only affect the temperature in reactants transported onto the surface but also change the rates of transport and the local species concentration.

A surface kinetic mechanism typically consists of three temperature-dependent process types: reactions of surface species with other surface species, surface species diffusion, and reactions of gas species with surface species. Sensitivity analysis has shown that the dissociative adsorption and abstraction reactions [53] play dominant role in catalytic fuel oxidation. However, for these reactions, a substantial fraction of the temperature dependence will come from the gas temperature at $T(0^+)$, which provides most of the energy required for a gas species to overcome a large activation energy barrier to reaction with the surface species. As such, the rates of these reactions have strong dependence on kinetic energy of the incident species at $T(0^+)$. For example, the reaction of dissociative adsorption of methane on platinum is the rate-limiting step in catalytic methane combustion [166] and has a strong dependence on the kinetic energy of methane (activation barrier of 27 kcal/mol [167]).

As a first order estimate of the rate change due to temperature slip, we assume that the rate of reaction of a gas-phase species G with a surface species S takes the form [168]:

$$R_G = \left(\begin{array}{c} \text{surface} \\ \text{flux of } G \end{array} \right) \cdot \left(\begin{array}{c} \text{reactive} \\ \text{site fraction} \end{array} \right) \cdot \left(\begin{array}{c} \text{sticking} \\ \text{coefficient} \end{array} \right) \cdot \left(\begin{array}{c} \text{fraction of } G \\ \text{with } E > E_A \end{array} \right)$$
$$= \frac{n_G \langle c \rangle_G}{4} \theta_S S_0 e^{-E_A/RT} = S_0 X_G \frac{n \langle c \rangle_G}{4} \theta_S e^{-E_A/RT} S_0 X_G P \theta_S \left(\frac{1}{2kT\pi m_G} \right)^{1/2} e^{-E_A/RT}$$

(18)

diffusion transport becomes non-equilibrium, i.e. the near wall molecular collisions are not sufficient enough (less than 10^3 collisions) to be modeled by using a continuous model such as the Navier–Stokes equations. In this case, the rarefied gas effect [162] becomes significant. The flow near the solid wall cannot reach thermodynamic equilibrium with the wall, yielding large slips of thermodynamic properties between the wall and the gas in the near wall boundary. In the slip flow regime ($10^{-3} <$ Kn < 0.1), the flow outside of the Knudsen layer can still be governed by the Navier–Stokes equations. However, corrections of non-continuum boundary conditions for discontinuities in macroscopic variables such as velocity, temperature and concentrations are needed to

where T is the gas temperature, $T = T(0^+)$, θ_S is the surface coverage of species S, n and n_G are the total number density and the number density of species G, $\langle c \rangle_G$ is the mean thermal speed of species G, X_G is the mole fraction of species G, and S_0 is the sticking coefficient for this reaction.

By assuming a constant pressure process, and neglecting the temperature dependence of X_G and θ_S, we can estimate the effect of the gas temperature T on R_G as $R_G \sim T^{-1/2} e^{-EA/RT}$. Fig. 57 shows the normalized reaction rate, $R_G/R_{G,NO \ SLIP}$, at 1000 K for the case of a reaction with $E_A = 27$ kcal/mol for different temperature jumps $T(0^+)-T(s)$. It is seen that a temperature slip of only 6% leads to nearly a factor of two difference between the actual reaction rate and that
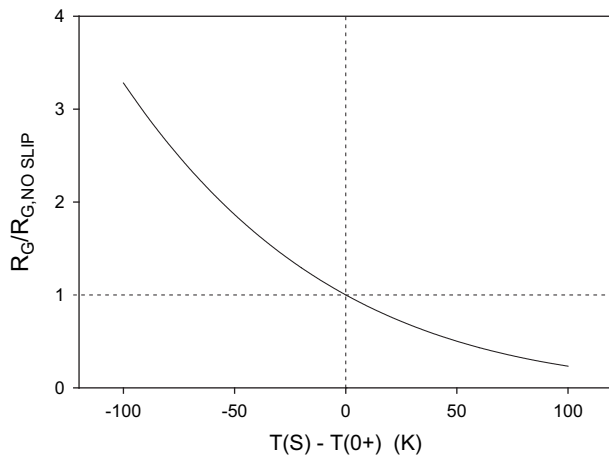
Fig. 57. The actual reaction rate constant R_G, normalized by the rate for the case without temperature slip, for a gas/surface reaction with $E_A = 27$ kcal/mol on a 1000 K surface, as a function of temperature slip.

calculated with the assumption that $T(s) = T(0^+)$. For reactions with larger activation energies or larger temperature gradients [169], it was observed that the near wall temperature change could be as high as 10 K per micrometer. At temperature above 1000 K, the Knudsen number was close to 0.1. Therefore, including non-equilibrium transport in micro-scale combustion is necessary to predict the reaction rates correctly.

The effect of temperature slip in low pressure catalytic combustion systems were investigated experimentally [170] by using low pressure combustion systems. The results showed that the temperature jump was 34 K at a pressure of 2.5 Torr, and had a very significant effect on the methane oxidation. Numerical modeling of temperature discontinuity in a 100 μm micro-combustor at one atmospheric pressure was conducted by Raimondeau et al. [128]. The results showed that the temperature slip at the wall was negligible.

In addition to the temperature slip, the mole fraction gradients of gas species near the wall will also yield a concentration slip. The phenomenon of composition slip has been detected in simulations of gas mixtures by Bird [162], Papadopoulos and Rosner [171,172]. More detailed reviews of the concentration slip were made by Scott et al. [173] and Gupta et al. [174]. Recently, Rosner and Papadopoulos [175] derived a simple expression for concentration slip based on the similarity between the transport of mass and energy. More recently, Xu and Ju [52,53] derived a more general expression to consider concentration slip in a non-equilibrium flow based on the gas kinetic theory,

$$\left(\frac{n_{i,s}}{n_{i,0+}}\right)\left(\frac{T_s}{T_{0+}}\right)^{1/2} = \left\{ 1 + \frac{4}{3\pi\bar{v}}\lambda\left(\frac{\partial u}{\partial y}\right)_{0+} \right.$$
$$\left. + \frac{\alpha_{i,m}-2}{\alpha_{i,m}}\lambda\left(\frac{\partial \ln(X_i)}{\partial y}\right)_{0+} \right\} \quad (19)$$

where n is the concentration, u the velocity, T the temperature, α the surface accommodation coefficient, and X_i the mole fraction. Note that when the macro velocity compared to the thermal acoustic velocity at the boundary layer is small, the contribution of velocity slip to temperature and concentration slip is negligible.

Eq. (19) shows that the concentration slip is coupled with the temperature slip. Unfortunately, in most of the previous work, the coupling of concentration slips with temperature and velocity slips was not examined. Fig. 58 shows the slip effect on the surface

reaction rate at different reduced Damköhler numbers defined by the ratio of diffusion time to the catalytic reaction time [52]. The results show that the slip effect becomes increasingly significant when Damköhler number is larger than unity. When the Damköhler number is large, the reaction process is diffusion controlled and a faster surface reaction will cause a larger concentration gradient and thus a larger slip effect. On the other hand, if the Damköhler number is small, the problem becomes reaction controlled. As a result, the relatively faster diffusion process yields a more uniform distribution of temperature and species near the reaction surface. Therefore, the slip effect becomes smaller at small Damköhler numbers. In practical applications, depending on the reactors working condition, the system Damköhler number can be either greater or less than unity. As the Damköhler number is increased from 0.1 to 5, Fig. 58 shows that both the slip model and the non-slip model show a monotonic increase of the reaction rates. However, if the Damköhler number is increased to 10, the reaction rate will be dominated by diffusion transport. It is seen that a non-monotonic distribution of the reaction rate appears near the entrance of the reaction channel. This phenomenon is caused by the competition between chemical reaction and species diffusion represented by the Damköhler number. It is also seen that because the coupling between temperature and concentration slips, it is not accurate to predict surface reaction rate by only considering temperature slip.

Numerical simulations included both temperature and concentration slips were also conducted by using detailed chemical mechanisms [53]. The results show that the concentration slip is proportional to the product of the Knudsen number and the species Damköhler number. It is also shown that non-equilibrium process has a dramatic effect on the radical reaction rates and mass fractions at a large Damköhler number and Knudsen number. It is demonstrated that at the leading edge of the micro-channel, the temperature slip has a greater effect on the fuel oxidation rate. However, as the reaction proceeds, the effect of concentration slip on radicals dominates. In addition, as shown in Fig. 59, the concentration slip has a larger effect on the reaction rates and mass fractions of OH, H and O radicals than on those of the reactants. Therefore, the non-equilibrium concentration slip and temperature slip are important issues in micro-scale combustion and need to be addressed.

3.4. Flame instability

The large heat loss and strong flame-wall structure thermal and kinetic coupling of micro-scale and mesoscale combustion result in
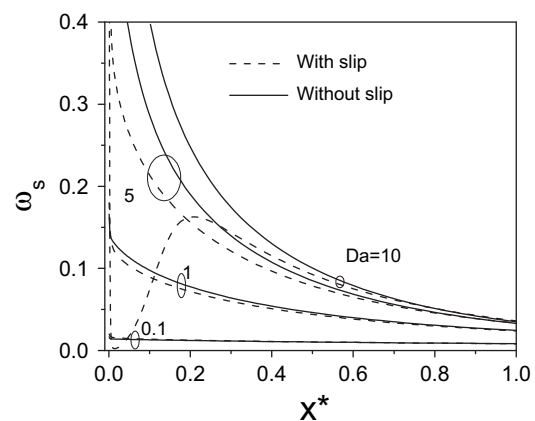

Fig. 58. Surface reaction rate at different Damköhler numbers along the channel ($T_{in} = 600$K, $Kn = 0.1$) [52].
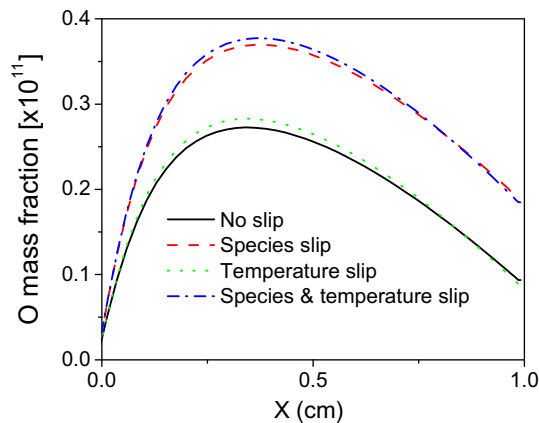
Fig. 59. The distribution of O on the surface along the streamwise direction (T_{in} = 300K, T_w = 1000 K).

Fig. 60. Schematic of repetitive ignition and extinction of mesoscale combustion.

rich phenomena of various flame instability such as the repetitive ignition and extinction [41,44–46,176], spinning combustion [47] and spiral and other flame patterns. These phenomena are inherent for micro-scale combustion and have been rarely observed in combustion of large scale.

3.4.1. Repetitive extinction and reignition instability

When the local wall temperature of a mesoscale channel is increased above the auto-ignition temperature by either via flame-wall thermal coupling or by an external heat source, ignition will occur and the resulting flame may propagate upstream (Fig. 60). If the wall temperature in upstream is reduced or the upstream channel width is below the quenching diameter of the normal propagating flame (Figs. 28 and 29), extinction will occur at upstream. Since the downstream wall remains hot, when the mixture after flame extinction reaches a location where the wall temperature is higher than the ignition temperature, auto-ignition will occur again. This cycle repeats and forms a repetitive ignition and extinction instability.

The experiments to observe ignition and extinction instability was conducted by Maruta and coworkers [41,44], by Kyritsis and coworkers [45,46] and by Fan et al. [177]. As shown in Fig. 61 (left), a cylindrical quartz glass tube with an inner diameter of 2 mm was employed as a model channel. The inner diameter of the channel was slightly smaller than the standard quenching diameter of the employed methane/air or propane/air mixtures at an equivalence ratio of 0.85. The channel was set between two parallel plate-heaters. A temperature gradient was formed in the middle of the tube. The measured wall temperature is shown in Fig. 61 (right). After being ignited, the flame was stabilized at a certain location with in the temperature gradient. The average mixture velocities were varied up to 100 cm/s.
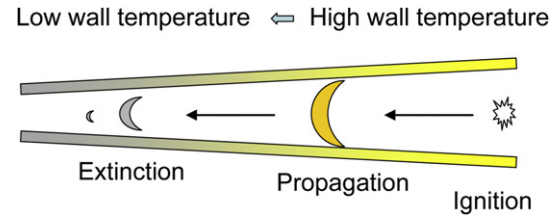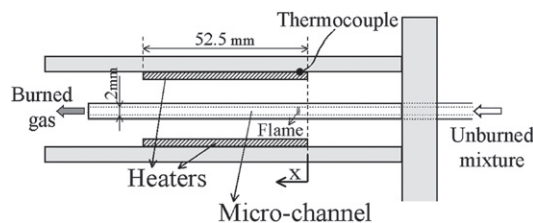
Fig. 62 shows direct photographs of the two different flames, a stable flame at a high flow rate (A) and a repetitive extinction and ignition flame at a low flow rate (B). The existence of a stable flame at high flow rate is because the flame speed with a high wall temperature is balanced by the high flow rate. The existence of the repetitive extinction and ignition flame is due to the mechanism shown in Fig. 60. Similar observations of the two different flame regimes were also made by Kyritsis and coworkers [45,46] (Fig. 63) in a curved channel.

The histories of the locations of the stable and unstable flames are shown in Fig. 64. It is seen that the flame location of the stable flame (Fig. 64A) does not change. Fig. 64B shows the temporal motion of the reaction zone obtained from those images. These flames were called flames with repetitive extinction and ignition (FREI) by its nature. The frequency of this oscillating flame is about 150 Hz. In addition to the two kinds of combustion modes, other flame modes that exhibit different dynamics were also observed (Fig. 64C and D). The so called 1D pulsating flame (Fig. 64C) exhibited regular periodical motions with almost constant lumi-nescence. Furthermore, flames that possess the characteristics of both pulsating flame and FREI were also observed (Fig. 64D). These flames are a combination of the periodical motions of pulsating flame with small amplitude and repetitive ignition and extinction with large amplitude. The intrinsic mechanism for the occurrence of different flame modes is due to the existence of multiple flame regimes and extinction limits [Fig. 62].

These non-stationary flame behaviors are described analytically by proposing one-dimensional nonlinear evolutionary equation of flame front which considers flame front acceleration and rate of flame temperature variation [176]. Fig. 65 indicates that derived amplitude of flame oscillations, i.e., length between upstream and downstream turning points during FREI together with S-shaped steady-state solutions which show flame location depending on the mixture flow velocity. Length of the flame brush during FREI shortens when mixture flow velocity decreased toward the tran-sition point from FREI regime (middle branch of steady-state solution) to weak flame regime (lower branch). This implies that weak flames are stabilized on or very close to ignition point of the given mixture.
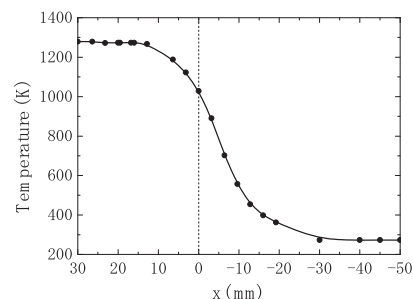

Fig. 61. Left: Experimental setup for flame propagation in a preheated mesoscale channel; right: wall temperature distribution of the channel [41].
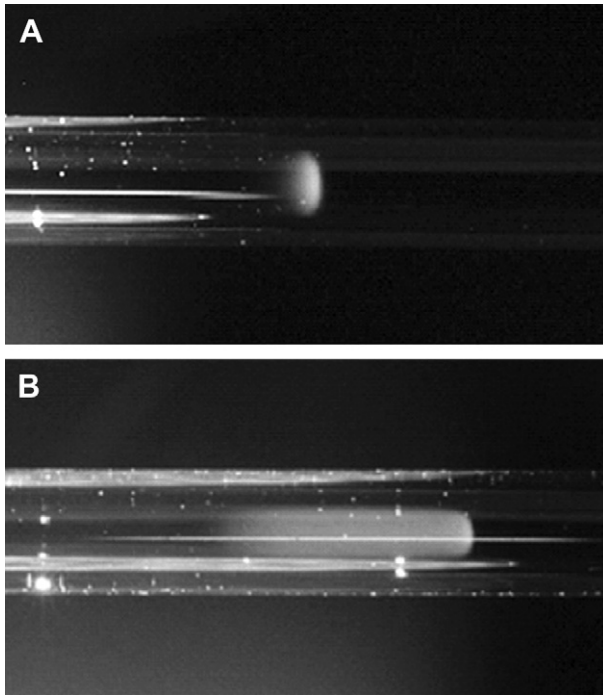
Fig. 62. Direct images of a stable flame and a repetitive extinction and ignition flame [41].

Numerical simulations of oscillating flames in small scale combustors were modeled by Norton et al. [129], Jackson et al. [50] and Kessler and Short [178]. Fig. 66 [129] shows the limit cycle of self-sustained oscillations in cases of a high heat loss of micro-scale combustor and the temperature evolution as a function of time. The results showed that the stationary flames became unstable in cases
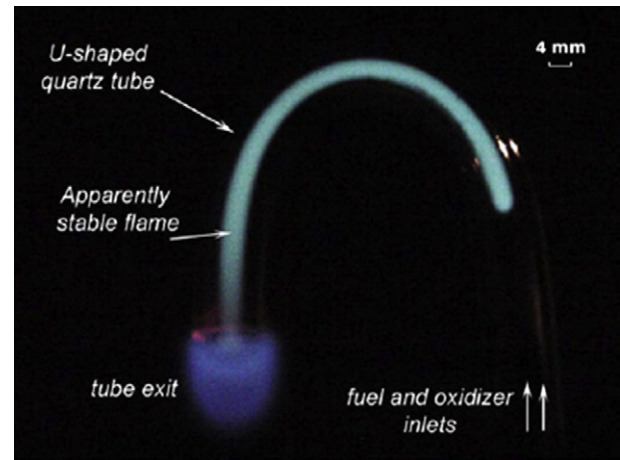

Fig. 63. An oscillating flame in a curved tube [45].

of high heat loss. The limit cycle frequency is about 1000 Hz. Regular flame oscillations and repetitive quenching and reignition instabilities were observed.

Two-dimensional direct numerical simulation with detailed chemistry and transport for fuel lean ($\phi = 0.5$) hydrogen/air flames in planar microchannels with prescribed wall temperature [126,127] successfully captured the details of the repetitive ignition/extinction phenomena. When the inlet mixture velocity U_{IN} increases from 0.8 to 0.9 cm/s, weak flame shifted to periodical ignition/extinction mode. Fig. 67 [127] shows the details of ignition/extinction behavior of (a, b) temporal variations of maximum temperature inside the channel, and two-dimensional distributions of OH (c−e) and H_2 (f−g) fractions at time instants $t_1 − t_3$, for $U_{\text{IN}} = 1$ cm/s. Incoming fresh mixture is heated by the hot walls and

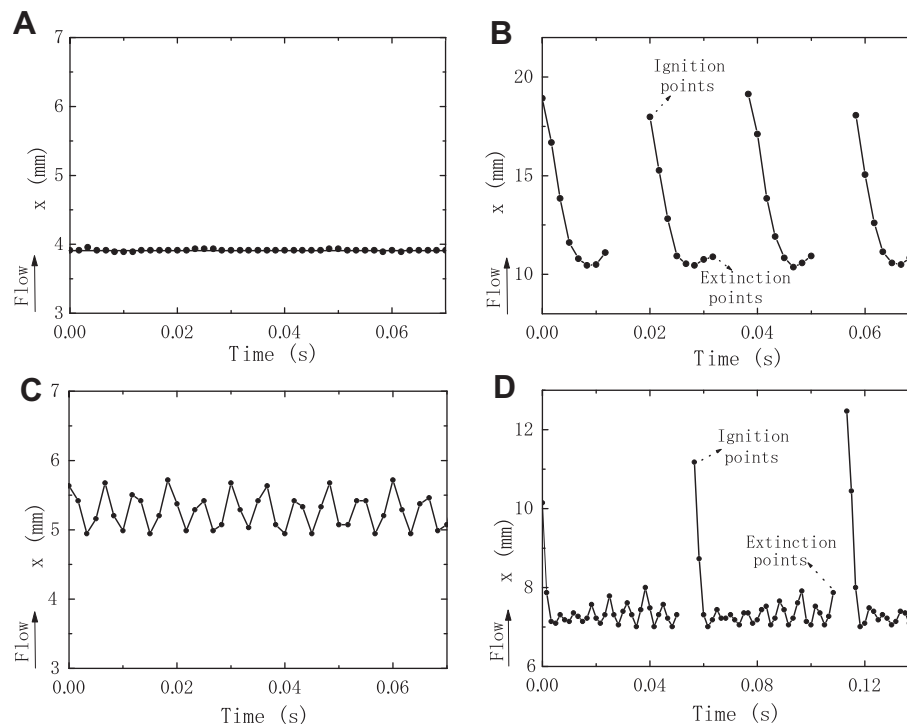

Fig. 64. Temporal motions of various flames of propane/air mixtures at an average mixture velocity of 30 cm/s and an equivalence ratio of 0.5; (A) stable flame in the case of maximum wall temperature, Tc = 1320 K, (B) flame with repetitive extinction and ignition, Tc = 1130 K, (C) pulsating flame, Tc = 1270 K, and (D) flame with a combination of pulsating flame and FREI, Tc = 1200 K [41].
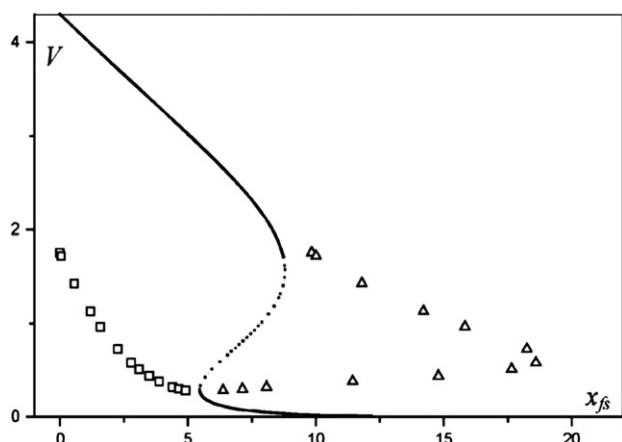
Fig. 65. S-shaped steady-state solutions depending on mixture flow velocity and amplitude of flame oscillation indicated by the upstream and downstream turning points of flames during FREI. Open triangles and squares are upstream and downstream turning points, respectively [176].

when the mixture was ignited at the tube exit, a propagating flame is formed in D section and propagates into C section. Fig. 69 shows the flame trajectory histories of transitions from a propagating flame to either a stabilized planar flame at equivalence ratio $\varphi = 1.5$ and flow rate $Q = 3$ cm^3/s (left) and a spinning flame at $\varphi = 1.5$ and $Q = 5$ cm^3/s (right). As shown in Fig. 69, the flame propagation has three stages. First, as the flame propagates in the section of the constant cross-section area, the flame speed is almost constant. Second, as the flame enters the convergent section, the decrease of tube diameter resulted in an increase of the local flow velocity and thus a decrease of flame propagation speed relative to the wall. Third, as the flame further moves upstream, it is stabilized in the convergent section around $t = 500$ ms (Fig. 69, left). However, with an increase of flow rate (Fig. 69 right), the propagating flame slows down first in the convergent section and then slowly transforms to a spinning flame around $t = 400$ ms at the same location with a constant spinning frequency. This slow flame transition process indicates that the onset of flame spin requires a certain time to initiate flame-wall coupling. Interestingly, it was also found that the

ignites at a certain downstream location. Then, the confined flame propagates horizontally both upstream and downstream. The upstream propagating flame changes its configuration from curved to nearly flat flame and extinguishes in the upstream. The downstream propagating flame keeps its initial configuration in the remaining fresh mixture and extinguishes, finally.

Further detailed experiments using rectangular quartz microchannel heated by infrared lamp are conducted [177]. Extinction and reignition phenomena are also observed and PLIF measurements for CH* and OH* are conducted. Movements of these excited species during extinction and reignition are successfully captured for the first time.

A closed end flame acceleration in a mesoscale channel was modeled by Gamezo and Oran [179]. The results showed that due to the boundary layer effect, the flame surfaces increased significantly as the flame propagated from the end wall toward the end with an open exit. The rapid increase of flame surface area led to a strong flame self-acceleration.

3.4.2. Spinning instability

When there is a thermal coupling between the flame and the wall, the thermal transport in flame structure augments the enthalpy transport in the flame via the indirect heat recirculation and leads to a multi-dimensional spinning instability in mesoscale combustion.

The spinning instability was observed by Xu and Ju [47] in a convergent and divergent channel (Fig. 68). The channel was vertically mounted and had two equal constant-area Sections A and D, a converging Section B, and a, diverging Section C. The inner diameter of the constant-area sections was 10 mm and that of at the throat was 4 mm. The wall thickness was 1 mm. The lengths of the diverging and converging parts were 50 mm and that of the D section was 600 mm ($L/d > 60$) to ensure a fully developed flow entering Section C. The convergent and divergent angles were all 6.9°. A mesh grid was placed near the inlet of the tube to eliminate any flow disturbance. The divergent cross-section was introduced to ensure that the final stabilization flame was always in the weak flame regime with a strong flame-wall coupling. The flame propagation history was recorded by a high speed camera at 500 frames per second.

In the experiments, four different flame modes, the propagating flame, a self-extinguished flame, the stabilized planar flame, and the spinning flame, were observed. For a given equivalence ratio,
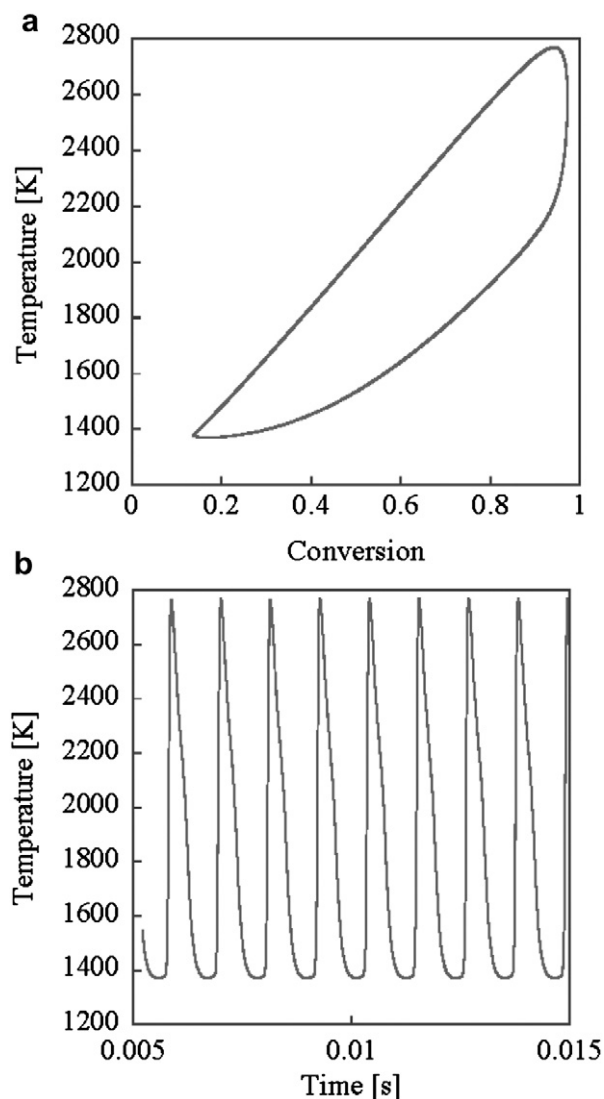

Fig. 66. (a) Limit cycle for a point on the centerline, indicating self-sustained oscillations in cases of high heat losses near extinction. (b) The temperature of this point vs. time. The oscillations occur with a period of 1 ms. The channel width and wall thickness are 600 μm and 200 μm, respectively [129].
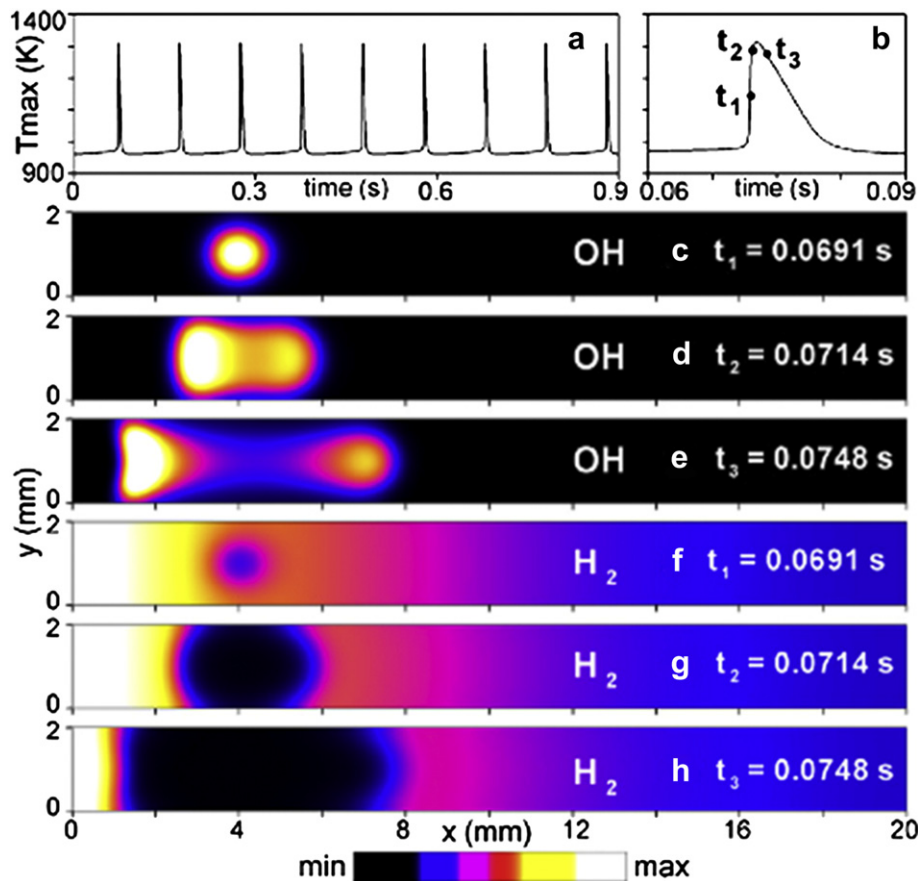
Fig. 67. Ignition/extinction mode at $U_{IN} = 1$ cm/s in the $h = 2$ mm channel: (a) temporal variation of the maximum temperature inside the channel; (b) expanded detail of (a); (c–e) and (f–h) 2-D maps of the Y_{OH} and Y_{H2}, respectively, at the three times t_1 to t_3 marked in (b). The minimum in the color-coded bar corresponds to zero for Y_{OH} and Y_{H2}, while the maximum to $Y_{OH} = 7.1 \times 10^{-4}$, 1.0×10^{-3}, and 6.0×10^{-4}, in (c–e), respectively, and to 5.14×10^{-3} for Y_{H2} [127].

transitions between spinning flames and stabilized planar flames can be controlled by varying the flame-wall coupling externally via external cooling or heating of the wall. For an example, if the wall is cooled, the spinning flame will stop and become a stable flame. This observation further confirmed that the flame instability is controlled by flame-wall thermal coupling. In addition, spinning flames were observed for both methane and propane flames at lean and rich conditions with both $Le > 1$ and $Le < 1$. This spinning irrelevance with the Lewis number contradicts with the classical theory of spinning combustion [106]. Moreover, the flame spin direction was randomly selected with equal probability in clockwise and counter-clockwise directions. The random selection of spinning direction implies that the instability is not governed by flow motion but by the thermal diffusion process. Furthermore, the spinning flame was also confirmed in tubes with only one divergent section and observed when the tube was set horizontally or upside down. Therefore, it was concluded that this spinning flame is not produced by buoyancy and is governed by the flame-wall thermal coupling.

It was also found that when the flow rate was decreased, the propagating flame transformed to a stabilized planar flame at a smaller diameter where the flow velocity balanced with the flame speed. If the flow rate was further reduced, the propagating flame would either extinguish at a smaller tube diameter or pass through the throat. Fig. 70 shows the different flame regimes for self-extinguished flames, stabilized planar flames and spinning flames. It is seen that for both methane-air (left) and propane-air (right) flames, there is a critical flow rate, above which spinning flame

exists and below which flame is stable. For methane flames, there is a quenching limit at low flow rates. For propane flames, the quenching limit exists for lean and rich mixtures at low flow rates. At near stoichiometric conditions and low flow rates, propane flames will pass the throat area without extinction.

The spinning frequencies of methane-air flames at different equivalence ratios and flow rates are shown in Fig. 71. Experiments were made by varying flow velocity at a given mixture concentration. It is seen that the spin frequency is roughly proportional to the average flame speed and only slightly affected by the flow rate.

In addition, the experiments showed that although the onset of flame spin was not governed by the mixture Lewis number, the mixture Lewis number effect had a strong effect on the shape of the spinning flame. Depending on Le, two different spinning flame shapes, an "L" shaped flame (flame tail is open) and an "S" shaped flame (flame tail closed), were observed for both methane and propane flames. In the conventional theory of thermal diffusion instability, the onset of spinning combustion only happens for a mixture Lewis number larger than a critical value, $\beta(Le - 1) > 11$
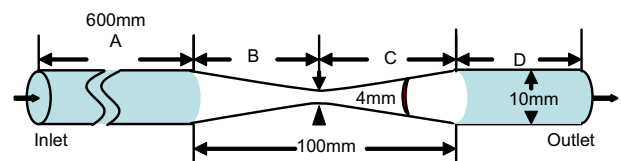

Fig. 68. Schematic of convergent and divergent mesoscale combustor [47].
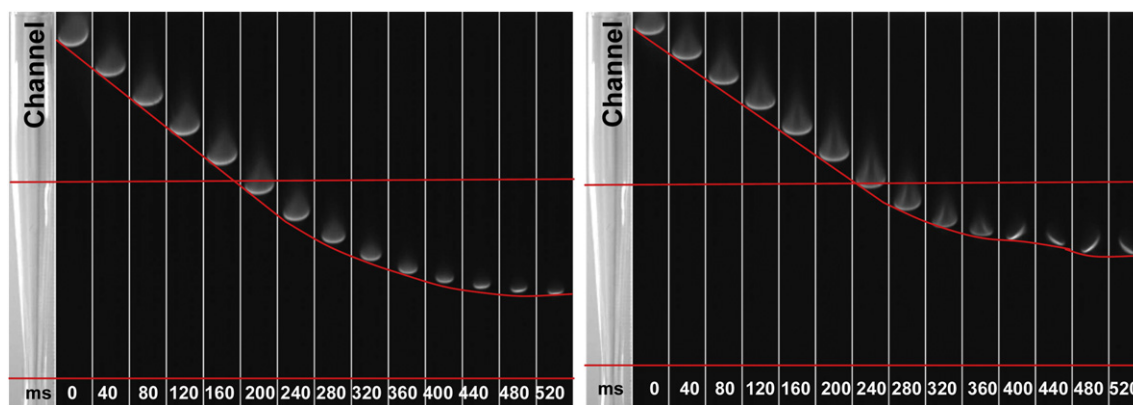
Fig. 69. Flame evolution histories for C_3H_8-air flames. (left) $\varphi = 1.5$, $Q = 3$ cm^3/s; (right) $\varphi = 1.5$, $Q = 5$ cm^3/s [47].

[123]. However, in small scale combustion, the enthalpy is also transported in the solid phase although the mass diffusion only happens in gas-phase. In order to understand the onset of flame instability, the estimation of an effective Lewis number for flame propagation in a small scale combustion with flame-wall thermal coupling is necessary. Since for the same boundary condition, the laminar flame speed is a function of Lewis number, the effective Lewis number can be simply extracted by comparing the flame speed calculated from Eq. (7) with heat recirculation with that obtained from Eq. (9) without heat recirculation. The calculated effective Lewis number is shown in Fig. 72. It is seen that the effective Lewis number increases as the diameter decreases. In particular, when the flame starts to couple with the wall, the effective Lewis number increases dramatically. In addition, the increase of flow rate results in an increase of the effective Lewis number at the same tube diameter. For methane-air flames that have Lewis number around unity, the effective Lewis number with flame-wall coupling can be as high as 1.5. If the Zeldovich number is around $\beta = 10$, the reduced Lewis number $\beta(Le - 1)$ will be larger than the critical value (11) for onset of spinning flames. This explains why the flow rate is important to cause the onset of the spinning flame.

Recently, spinning flames in a heated channel was identified by three-dimensional DNS for hydrogen/air flames [180].

3.4.3. Spiral flames and pattern formations

Spiral and other patterns, commonly observed in excitable media, were reported in combustion systems [181–183]. In this section, recent observations on pattern formations in micro flames are introduced. Repetitive extinction and ignition instability in a straight tube with an external heat source exhibits various instability and oscillatory phenomena such as regular cyclic

oscillation, pulsation and other chaotic oscillations that described in Section 3.1.1. While these phenomena occurred in a spatially one-dimensional geometry, studies on two-dimensional radial-flow system recently demonstrated other rich varieties of chaotic instabilities and pattern formations. Here, such phenomena observed in radial micro-channel [184–186] and rectangular channel between two parallel plates [126,127] both with external heat sources are described.

A straight tube with an external heat source which is modeled as one-dimensional plug flow geometry was extended to spatially two-dimensional radial-flow system, i.e., radial micro-channel between two circular plates with temperature gradient as shown in Fig. 73. An external heater for establishing a positive temperature gradient in radial direction from room temperature to around 850 K was employed. Repetitive extinction and ignition instability in a system with additional degree of freedom in angular direction is likely to occur in the radial-flow system. In fact, various flame patterns are observed and each pattern can be transformed one to another with the variations of parameters such as mixture flow rate, equivalence ratio and gap between two plates as shown in Fig. 74 [184]. One can expect stable circular flame in radial micro-channel from the steady normal flame in a straight tube. As expected, most probable flame pattern in the regime diagram is stable circular flame when the gap between two plates is 2 mm as shown in the figure. However, single or double separated flames rotating around the center of the channel, which are termed as pelton (wheel)-like flames [187], are also observed at fuel lean and rich conditions. At the region between those for circular stable flames and pelton (wheel)-like flames, circular flames, which are termed traveling flame, is observed. Traveling flame is a circular flame, which is divided into some fractions where each fraction exhibits tangential movement [188]. At higher inlet mixture
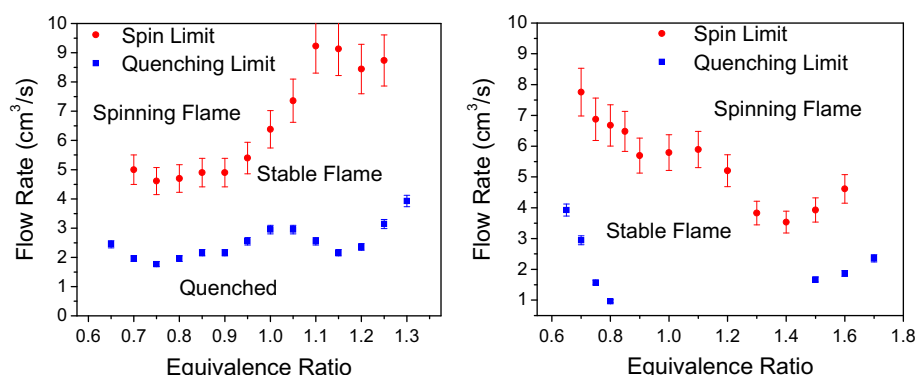

Fig. 70. Flame regime diagram for different flow rates equivalence ratios. (left: Methane-air mixture; Right: Propane-air mixtures) [47].
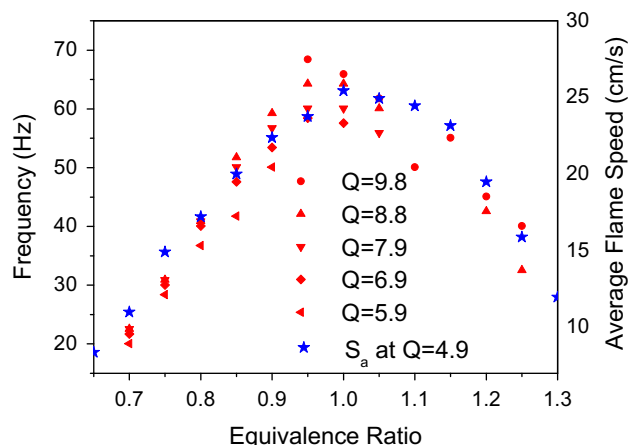
Fig. 71. Frequencies of methane and propane spin flames at different equivalence ratios for methane-air flames [47].

velocity and near stoichiometric conditions, unstable circular flames and rotating triple flames which have three branches are observed. It is noted that observed flame patterns are sensitive, particularly to the gap between two plates. For instance, no stable circular flames are observed when the gap is equal to 1.5 mm. Instead, traveling and pelton wheel-like flames occupy 80 and 20% of regime diagram, respectively.

This implies that small scale combustion chamber with radial-flow geometry is likely to be suffered from these combustion instabilities. Accordingly, combustion completeness in the radial channel during the pattern formation is examined [185]. Combustion efficiencies estimated from the burned gas composition are 0.82−0.88 for double pelton flames whereas 0.48 to 0.82 for single pelton flame. Significant amount of unburned fuel and CO are flowing out without completing combustion in low combustion efficiency conditions. One can imagine the difficulties in completing combustion at small scale combustor with two-dimensional geometries, such as MEMS micro-gas turbines.

Besides the above flame patterns, spiral flames are observed at high velocity region at the gap between two plates larger than 2 mm [184,186]. Fig. 75 [186] shows spiral flame evolution recorded by high speed camera with 2 ms time interval at mean flow velocity of 5.5 m/s in 4 mm i.d. delivery tube, $\phi = 1.25$ and plate distance of 2 mm. Target patterns are also observed in the vicinity of pattern transition from stable flame to bifurcated structure.

Mechanisms of pattern formations are investigated and few aspects are clarified to date. Inner and outer edges of the pelton and
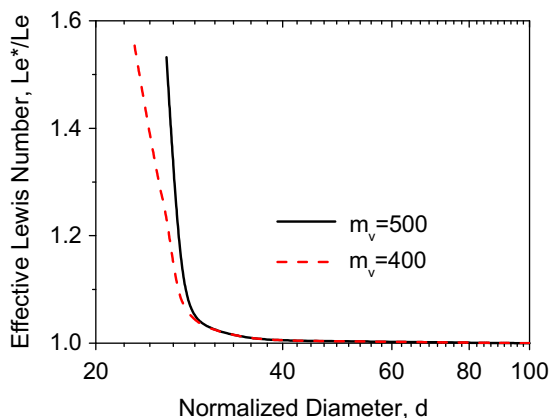

Fig. 72. The effective Lewis number calculated from theoretical analysis by matching the flame speeds with and without heat recirculation for methane-air mixture [47].
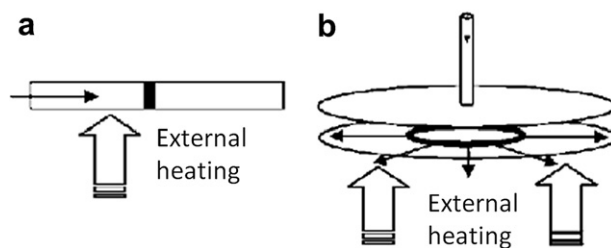

Fig. 73. Combustion systems in a straight tube (a), and in a radial channel (b): the bold curve indicates the flame position; the arrows show the gas-flow direction.

traveling flames are correlated with the locations of ignition and extinction of FREI phenomena based on experimental results [189]. Single/double pelton flames and spiral flames are reproduced with two-dimensional transient computations [189] and their structure are examined. Clarifications of pattern formation mechanism and those flame structures are, however, difficult task in general.

Detail of reignition in FREI phenomena is examined numerically and experimentally [190,191]. Splitting flames, which have dual reaction fronts, one propagating to upstream and another to downstream directions, are observed. This is due to the fact that reignition of FREI starts not at the edge of recharging fresh mixture but at a certain point with small distance from the edge of the fresh mixture. It is reported that splitting flame behavior is playing key role for pattern formations [189]. Splitting flame behavior is also identified independently [127] for hydrogen-air mixture by 2-dimensional DNS as shown in Fig. 67.

Two-dimensional direct numerical simulation with detailed chemistry and transport is conducted for hydrogen/air flames at atmospheric pressure in a rectangular channel between two parallel plates [126,127]. Temperature gradient along the flow direction which ramps smoothly via a hyperbolic tangent function from 300 K to 960 K is given to the channel wall as a boundary condition. Three kinds of channel heights, 2, 4 and 7 mm cases are examined for wide range of inlet mixture velocities from 0.3 up to 1100 cm/s. Because of this wide velocity range and wider channel height compared with the ordinary quenching distance of hydrogen/air mixture, rich varieties of flame patterns are obtained as well as comprehensive results which cover the conditions that are addressed by the existing experimental studies [41,45]. Fig. 76 shows four new kinds of flame regime, i.e., open steady symmetric flames, oscillating, asymmetric and chaotic flames are predicted at $U_{IN} > 75$ cm/s in addition to the three flame regime, weak flames, ignition/extinction and closed steady symmetric flames at $U_{IN} < 75$ cm/s h_{Tmax} in the figure is the transverse distance of the maximum flame temperature location from the lower wall normalized by the channel height. The latter three flames are essentially equivalent to the stable normal and weak flames and non-stationary ignition/extinction instability (FREI) which are identified in the relevant experiment [41].

Temporal variation of the integrated heat release rate and OH fraction contour of oscillating flame at $U_{IN} = 300$ cm/s are shown in Fig. 77. The oscillation of the integrated heat release rate is somehow periodic while oscillating flame at $U_{IN} = 100$ cm/s exhibits chaotic oscillatory behavior (not shown). Two separated flames in Fig. 77 appear to be resulted from the interaction of the steady open symmetric flame with the chaotic cellular flame.

3.5. Non-premixed combustion

As combustor size decreases, the flow Reynolds number becomes very low (1−100) [2]. Therefore, the molecular diffusion is the dominant mechanism for viscous flow and fuel-air mixing
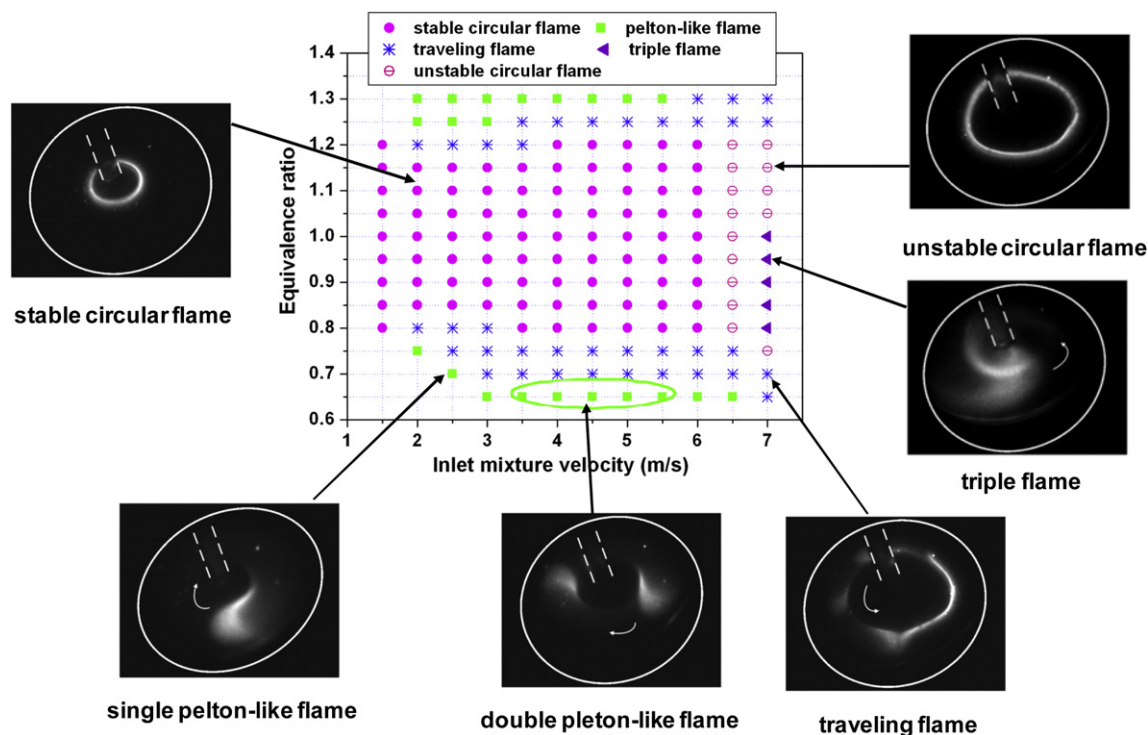
Fig. 74. Flame patterns observed in radial micro-channel and their regime diagram for methane/air mixtures at the gap between two plates is 2 mm [184].

[192–194]. When the wall heat loss increases, the limited fuel/air mixing due to molecular diffusion will dramatically change the flame dynamics, leading to flame instability [48], flame streets, and unsteady flame propagation [49]. For liquid fuel combustion, the vaporization of liquid fuel and mixing with air create new challenges to micro-scale combustion [92].

3.5.1. Mixing, liquid fuel vaporization

To study the diffusion limited combustion phenomena, the characteristics of micro-scale hydrogen diffusion flames produced from sub-millimeter diameter (d = 0.2 and 0.48 mm) tubes were investigated using non-intrusive UV Raman scattering coupled with LIPF technique [193]. Simultaneous, temporally and spatially resolved point measurements of temperature, major species concentrations (O_2, N_2, H_2O, and H_2), and absolute hydroxyl radical concentration (OH) were made in the micro flames. The OH imaging result indicated that a spherical flame was formed with a radius of about 1 mm as the tube diameter was reduced to 0.2 mm. The coupled effect of ambient air leakage and pre-heating enhanced thermal diffusion of H_2 leads to lean burn conditions for the flame. The results confirmed that at low Peclet numbers, the flames were in the convection−diffusion controlled regime.

To investigate the limiting mixing rate by molecular diffusion, a simple scaling analysis was made by Dellimore and Cadou [192] for various Reynolds numbers associated with fuel-air mixing in a micro-power system as a function of its overall size and power
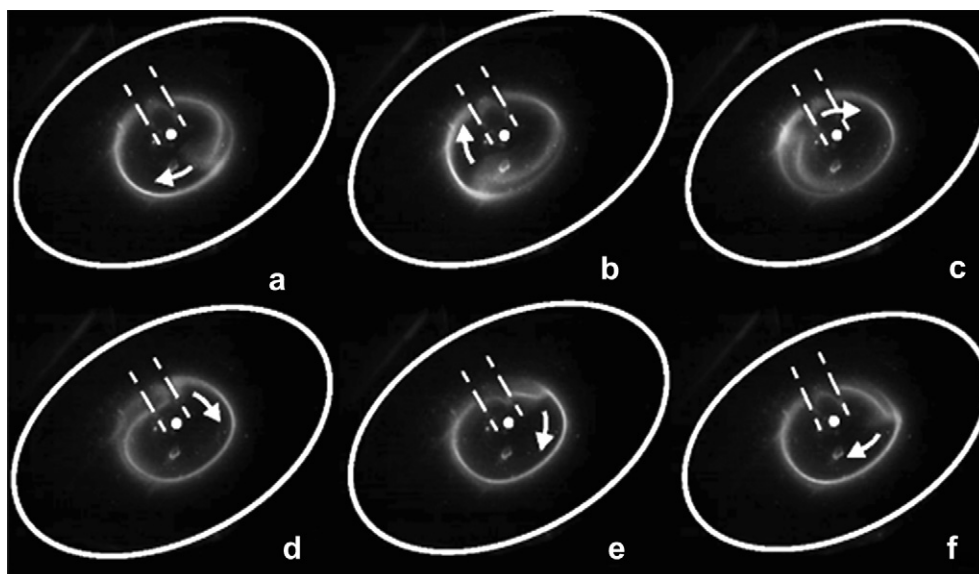

Fig. 75. Evolution of Spiral flames in 2 ms time interval. Mean flow velocity at i.d. 4 mm delivery tube (white dashed line) of 5.5 m/s, ϕ = 1.25 and plate distance of 2 mm [186].
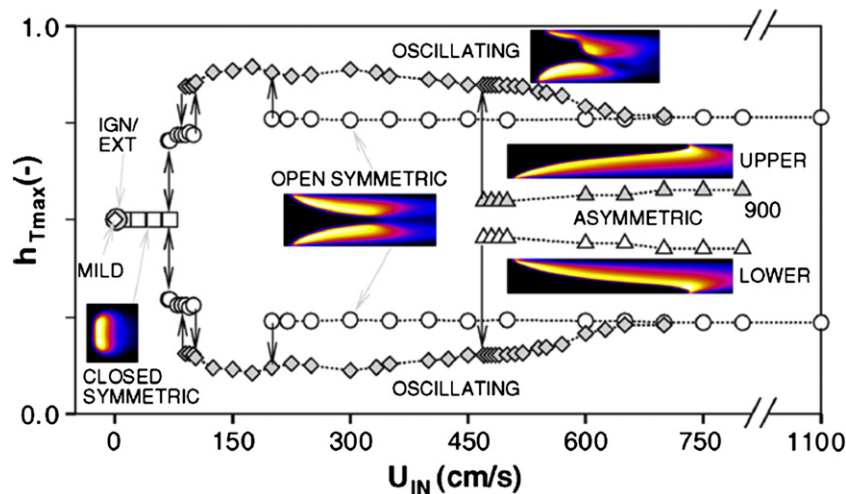
Fig. 76. Flame stability diagram for the channel height = 4 mm. The images are OH mass fraction in the channel [127].

output. The analysis showed that flows in micro-power systems can vary widely with Reynolds numbers spanning laminar, transitional, and fully turbulent regimes. In general, however, the Reynolds numbers associated with micro-power systems are much smaller than in their conventional-scale counterparts suggesting that achieving adequate fuel-air mixing will be more difficult than in conventional-scale power systems. A survey of the literature was made and indicated that there is an absence of experimental data in the appropriate Reynolds number range for micro-scale combustion, rendering the prediction of the performance of micro-scale mixers difficult. Designs of micro-combustors by ulatrosonic microwave system or using flow instabilities to enhance fuel-air mixing is necessary.

To establish non-premixed mesoscale combustion using liquid fuels, Siriganano et al. [92] developed a cylindrical direct-injection liquid-fueled combustors (Fig. 78). A portion of the liquid fuel is injected onto the wall to simultaneously cool the combustor walls and to expose the fuel for vaporization as a liquid film. As shown in Fig. 78 (left), a syringe pump delivers the liquid fuel and eight 1 mm diameter inlet tubes were attached (offset from the centerline) to provide approximately uniform filming over the interior of the 1 cm diameter and 4 cm long combustor tube. The swirler at the base of

the tube is a sheet-metal butterfly. The estimated swirl number was about 2 at the conditions of the combustion tests. The combustor takes advantage of the fact that a surface area advantage of film combustion over spray combustion occurs for small volumes as the surface to volume ratio of the combustor increases. A simple analysis was conducted and indicated that if a combustor of this type were part of a miniature engine, power levels from 10 W to 10 kW would be achievable with combustor volumes varying from a few hundred cubic millimeters to a few cubic centimeters and fuel flow rates varying from about 1 mg/s to 1 g/s. Experimentally, it was shown that an internal flame could not be maintained for the pure-gas-fuel flame with weak swirl, but was sustainable for liquid/gas and pure-liquid flames. Fig. 78 (right) shows a pure heptane/air flame burning in the miniature combustor. The liquid-heptane-fueled metal combustor exhibits a wide range of flame characteristics depending on the airflow rate through the system. Fig. 78 shows this range as the airflow increases from 4.5 to 8 L/min while holding the liquid fuel flow rate constant at 63.7 cc/h (an equivalence ratio range from 1.6 to 0.9, respectively for complete). Fig. 78a shows the lowest airflow case and the large external diffusion flame that results. As the airflow rate increases (Fig. 78b), the swirl contribution grows and some internal fuel-air mixing
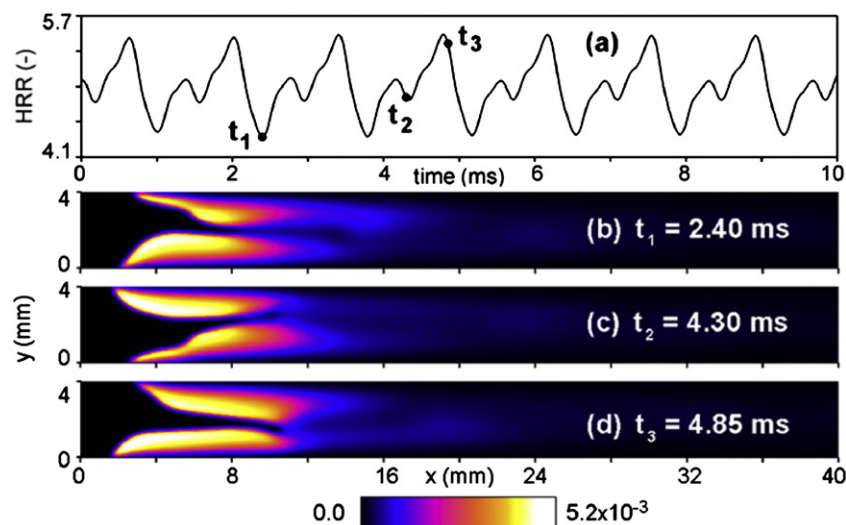

Fig. 77. Oscillating flames at inlet mixture velocity at 300 cm/s in the 4 mm height channel; (a) time history of integrated heat release rate and (b)-(d) OH fractions at the time instants t_1 to t_3 [127].
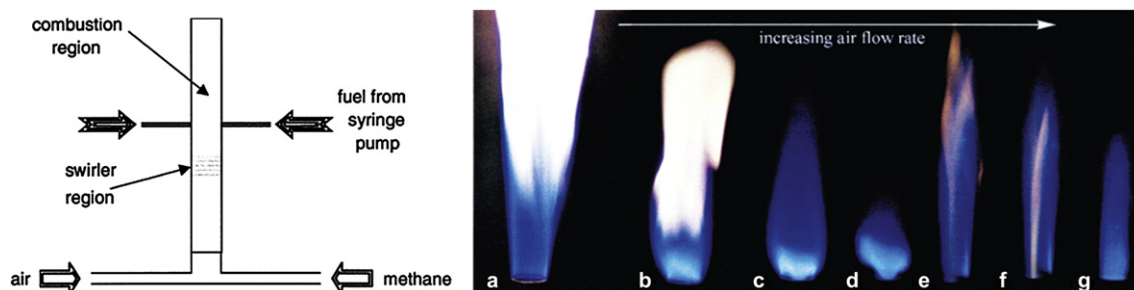
Fig. 78. Left: Experimental apparatus for demonstrating the film combustion concept. Right: heptane burning in the liquid film combustor at different airflow rates with a fixed liquid-fuel flow rate (63.4 cc/h). Image (g) corresponds to the stoichiometric fuel/air condition [92].

occurs. With further airflow increase (Fig. 78c and d), the system behaves like a prevaporizing-premixing combustor. Finally, in Fig. 78g (very close to the stoichiometric condition), the internal flame appears uniformly mixed. Further air increase beyond this condition blows the flame out. These differences in flame behavior show that the fluid dynamic structure, fuel-air mixing, and heat loss played an important role in changing the flame characteristics.

3.5.2. Formation of diffusion flame cells and flame streets in meso and micro-scale combustion

The joint effect of diffusion limited combustion and the wall heat loss also create new flame regimes for non-premixed flames. Cellular instabilities of laminar non-premixed diffusion flames were observed in a polycrystalline alumina micro-burner with a channel wall gap of dimension 0.75 mm [48]. The burner consists of an inverted Y-shaped geometry having fuel and oxidizer supply legs (Fig. 79), with a rectangular combustion channel of length 30 mm and cross-section 0.75 mm $\times$ 5 mm situated above the splitter plate. The top of the burner is open to atmospheric air, so that exhaust gases and unreacted material may exit. Changes in the flame structure were observed as a function of the fuel type (H$_2$, CH$_4$, and C$_3$H$_8$) and diluent. As shown in Fig. 79 (right), multiple isolated reaction zones or flame cells were observed. In addition, the number of flame cells observed inside the burner was dependent on the initial supply flow rates and stoichiometry, and varied between one and four for the length of the burners considered here.

By analyzing the mixture Lewis numbers (at low Lewis numbers), it was concluded that these cells were resulted from a cellular instability of the underlying diffusion flame, but one that occurred along the length of the combustion channel and aligned with the flow direction.

To further understand the combined effect of molecular diffusion and wall heat loss and friction, the non-premixed flame dynamics in a fuel-air mixing layer of a mesoscale channel was experimentally and analytically studied by Xu and Ju [49] by using methane and propane-air mixtures. The effects of channel width, wall temperature, and flow rate on the flame regimes and propagation speeds of non-premixed flames in a mesoscale combustor were studied. A flame street structure (Fig. 80) which consists of multiple triple flamelets in the mixing layer of the reactants was observed experimentally for both methane-air and propane-air mixtures. In addition, the results shown that the number of flame cells depends on the wall heat loss. By raising the wall temperature, Fig. 80 shows that the flame cells moves upstream and form a single triple flame when the temperature is 500 °C. Different from the observation in [48], the experiments showed that the existence of multiple flame cells or a flame street is not affected by the mixture Lewis number, but by the competition between diffusion and heat loss quenching. A scale analytical model was developed and the results qualitatively explained the mechanism of flame streets and reproduced the flame separation distance.
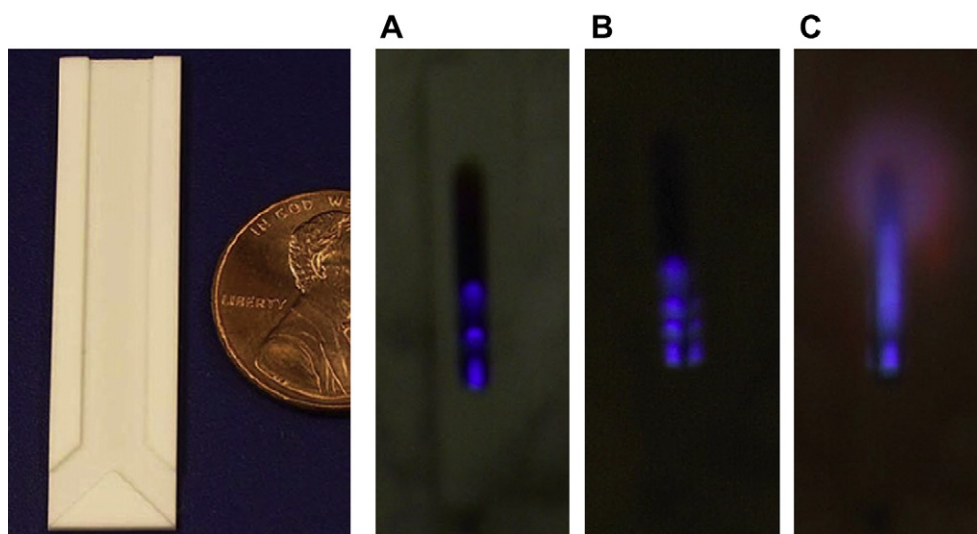
Fig. 79. Left: A photograph of one section of the Y-shaped alumina burner. Right: Chemiluminescent images: (A) Three flame cells formed with 100 sccm CH$_4$/200 sccm O$_2$. The flame cell closest to the top of the burner is the one at the top of the image. The bottom cell is slightly elongated due to the strained flow from the angled burner inlets. (B) Four flame cells for 100 sccm CH$_4$/130 sccm O$_2$. (C) A laminar diffusion flame atop a single cell (the exclamation mark flame) for 65 sccm CH$_4$/150 sccm O$_2$. A methane/air diffusion flame can also be observed at the exit to the burner [48].
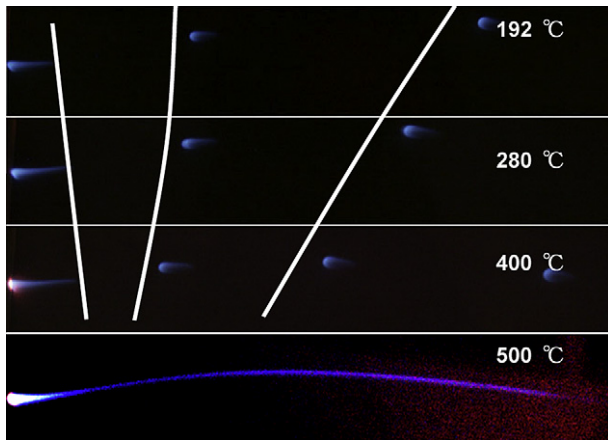
Fig. 80. The flame street formed in the methane-air at different flow and wall conditions (U_{air} = 26 cm/s, U_{CH4} = 12 cm/s) [49].

As the wall heat loss increases, an unsteady bimodal flame regime was observed (Fig. 81). Initially, there was only a single stable triple flamelet "A" formed in the upstream of the mixing layer. Then, a new triple flamelet "B" was formed at the downstream and propagated upstream. Both its size and flame speed decreased as it moved upstream. Due to the triple flame interaction between "A" and "B", the triple flamelet "B" decelerated and finally stabilized in the product wake of the triple flame "A". At t = 0.16s, triple flamelet "A" extinguished and this change in the product dilution due to the extinction of triple flame "A" reached triple flamelet "B" at t = 0.4 s. Therefore, at t = 0.48 s, triple flamelet "B" grew in size and accelerated again as a propagating flamelets. It then stabilized at the same location as flamelet "A" and extinguished due to the heat loss. The extinction, reignition, and unsteady propagation processes repeated, resulting in the unsteady bimodal flame regime. It was found that the separation distance of the flamelets increased due to the dilution effect of the products and that the size of the flamelets was proportional to the width of the mixing layer. The propagation speed of the mesocale non-premixed flame cell was measured. It was found that the edge

flame speed was significantly faster than that of the conventional triple flame, suggesting a strong effect of wall friction on flame propagation. Further studies are needed to understand how viscous flow in a confined mesoscale combustion affect edge flame propagation.

Structures of micro-diffusion flames from a sub-millimeter tube at low Peclet numbers were also investigated by Matta et al. [194], Cheng et al. [193] and Kuwana et al. [195]. In the experiments of Cheng et al., the characteristics of micro-scale hydrogen flames from 0.2 mm to 0.48 mm were measured by using UV Raman scattering and laser induced fluorescence for temperature, major species, and OH concentrations. A spherical flame with a radius about 1 mm was observed. The results showed that the quenching of the flame base near the nozzle exit caused air leakage and the pre-heating by the micro flame enhanced the effect of thermal diffusion of hydrogen, leading to lean burn conditions for the flame. An theoretical analysis of the extinction limit of micro-diffusion flames was conducted by Kuwana et al. by using the classical Burke–Schumann theory. The results showed that extinction occurs when the mixture-fraction gradient at the flame tip is greater than a critical value.

4. Future research of micro-combustion

With the recent concerns of energy security and climate change, micro-scale combustion can be a new platform for new concept research and development on efficient energy conversion systems.

4.1. Low temperature mesoscale combustion for advanced engines

Not only for power generation applications, future unmanned aerial vehicles (UAVs) require small, efficient, and lean burn engines for propulsion. Thus, further developments of scale-down engines such as micro-gas turbines, spark ignition- and compression ignition-type reciprocating engines, Wankel engines, and free-piston engines are still encouraged.

For instance, the small gasoline engines (10–50 cc) used for UAVs suffer significant heat and radical losses to the engine wall. Ignition and complete combustion in fuel lean conditions becomes difficult. Therefore, knowledge gained in micro-scale combustion to reduce thermal and radical losses by using heat recirculation and catalytic reactions can be used in optimizing the engine design. Moreover, with the implementation of stringent US-2010 regulations [196], there is an increasing interest in developing advanced compression ignition engines to achieve higher fuel efficiency and reduced emissions for ground transportation. These technologies include homogeneous charge compression ignition (HCCI) engines [197–199] for gasoline fuels and low temperature combustion (LTC) engines [200–203] for diesel fuels. In order to avoid early ignition, knocking, and control the heat release rate at high loads, strong thermal and concentration stratifications are employed [204]. As such, similar to micro-scale combustors, combustion and partial mixing of LTC that occur in a small and confined space will involve different burning regimes because of the large thermal stratification and coupling with wall structures, acoustic waves, species concentration gradient in the mixing-controlled process [205], low temperature and high temperature ignitions, ignition to detonation transition, and flame quenching and reignition at high levels of dilution. The new combustion regimes identified in meso and micro-scale combustion can be applied to developed advanced HCCI, spark assisted HCCI, and low temperature combustion engines [139,206].
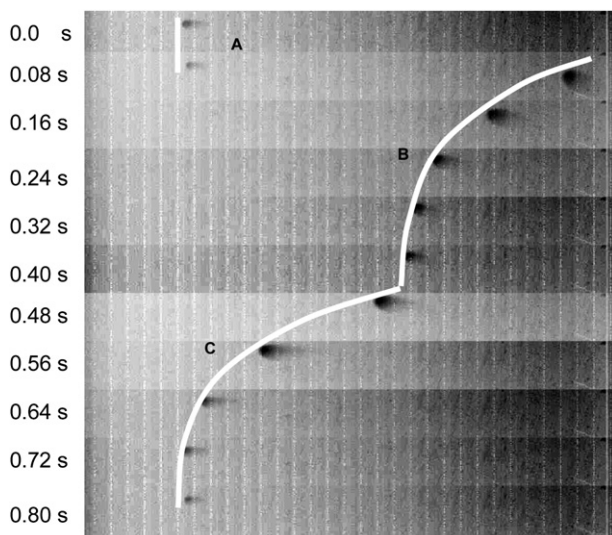

Fig. 81. Flame propagation history at heating power 160 W, U_{CH4} = 11 cm/s, U_{air} = 29 cm/s: the bimodal unsteady propagating flamelets [49].

4.2. Microreactors for fuel reforming

Combinations of combustors/reactors with energy conversion devices for realizing micro-power generation as well as fuel reforming [207,208] and synthesis from biomass at extreme combustion conditions with higher efficiencies are drawing more and more attention. A catalytic combustor with commercial thermoelectric devices recently reached 3.0% total conversion efficiency which exceeds the typical value of batteries [209].

Microreactors for fuel reforming are also promising. The recent development of synthetic liquid fuels for transportation from alternative resources to mitigate climate change and foreign oil dependence has led to extensive research on microreactors for fuel reforming. Many miniaturized methanol reformers with Cu/ZnO/Al$_2$O$_3$ catalyst-based micro-reactor suitable for the supply of hydrogen for a small methanol proton exchange membrane fuel cell (PEMFC) have been designed and fabricated using micro-fabrication techniques [210–212]. A micro-reactor (25 × 17 × 1.3 mm^3) [210] was constructed from glass and silicon substrates to form a serpentine catalyst-coated micro-channel of 333 mm in length and cross-section of 0.4 × 0.6 mm^2. Experiments with the Pt–Sn/Al$_2$O$_3$ coated micro-channel combustor [211] showed that the micro-reactor was active enough to initiate hydrogen combustion at room temperature and able to increase reactor temperature up to 800 °C by hydrogen combustion uniformly. The micro-channel methanol reformer generated enough hydrogen for power output of 26 W as fuel cell. With the interests of synfuels, future research of micro-channel reactors will pay more attention to butanol and other large hydrocarbon synfuel productions from cellulosic biomass and coal/biomass derived syngas. Recently, a micro-channel reactor has been developed to synthesize liquid fuels for transportation from synthetic gas by using a rhodium catalyst on Al$_2$O$_3$ or CeO$_2$ [212].

4.3. Microreactors for boundary layer flow control

Microreactors can also be used for aerodynamic control of flow separation and mixing of aircrafts to reduce drag, noise, and increase fuel efficiency. Recently, various plasma assisted microreactors have been developed to control flow separation on the surface of high speed wings and jet noise of engines [213,214]. A plasma generator on wing surface can provide fast production of micro vortexes to change the velocity profile in the boundary layer and to delay the flow separation. An experimental investigation of separation control using steady and pulsed plasma actuators was carried out on an Eppler E338 airfoil at typical micro-air vehicle Reynolds numbers ($20{,}000 \leq Re \leq 140{,}000$) [214]. The results showed that at conventional low Reynolds numbers ($Re > 100{,}000$), asymmetric single phase plasma assisted actuators can have a detrimental effect on airfoil performance due to the introduction of low momentum fluid into the boundary layer. An effective separation control was observed at a power input on the order of 5 mW per centimeter. Plasma assisted microcombustors can also provide opportunities for fast control of mixing and shock/combustion interactions in a supersonic ramjet engines.

4.4. Micro-combustion launching new concept fundamentals

New concept fundamentals attributed to nature of a small scale system, such as weak flame, specific instabilities/dynamics in micro-scale system, pattern formations, non-equilibrium effects, homogeneous and heterogeneous reaction interaction, are just on the horizon. Effects of wall/flame and thermal/chemical interactions play an important role due to the large surface/volume ratio. Exploration in other scaling issues in fluid dynamics, heat transfer, thermodynamics, and chemical reaction/combustion may lead to

new fundamentals and developments. Recently, Manesh et al. [215], examined reaction of multilayer thin nano-films of dense Metastable Intermolecular Composite (MIC) materials, and found that the flame speeds in MIC is affected by heat dissipation in substrates in sub-micron thickness. Studies on such nano-scale energetic materials are also collecting increasing attentions [216, 217]. By establishing well-defined experimental conditions, micro flow reactor with temperature gradient is started to be used for general ignition/combustion study by examining and validating the chemical kinetics for alternative fuels [138,139]. Such trial was conducted using weak flames in a micro-channel with prescribed wall temperature profile. Since weak flames in a heated channel are on the ignition branch, ordinary multi-stage ignitions of given mixture are converted into the stabilized stationary multiple weak flames by the methodology. Collaborations of micro-combustion studies with cutting-edge interdisciplinary research areas, such as nano- and bio-materials, visualization and diagnostics technologies are also encouraged since a variety of new physical-chemical phenomena being observed in micro and mesoscale systems can be further enriched by the synergetic effects.

References

[1] Dunn-Rankin D, Leal EM, Walther DC. Personal power systems. Progress in Energy and Combustion Science 2005;31(5–6):422–65.

[2] Fernandez-Pello AC. Micropower generation using combustion: issues and approaches. Proceedings of the Combustion Institute 2002;29:883–99.

[3] Kang K, Meng YS, Breger J, Grey CP, Ceder G. Electrodes with high power and high capacity for rechargeable lithium batteries. Science 2006;311(5763): 977–80.

[4] Yetter RA, Yang V, Wu MH, Wang Y, Milius D, Aksay IA, et al. Combustion issues and approaches for chemical microthrusters. In: Kuo KK, de Dios Rivera J, editors. Advancements in energetic materials and chemical propulsion. Begell House; 2007.

[5] Sutton GP, Biblarz O. Rocket propulsion elements. 7th ed. John Wiley & Sons; 2001. p. 751.

[6] Chigier N and Gemci T. A review of micro propulsion technology, 41st aerospace sciences meeting and exhibit, AIAA-2003-670; 2003.

[7] Annen KD, Stickler DB and Woodroffe J. Glow plug-assisted HCCI combustion in a miniature internal combustion engine (MICE) generator, 44th AIAA aerospace sciences meeting and exhibit, AIAA-2006-1349; 2006.

[8] Srinivasan R, Hsing IM, Berger PE, Jensen KF, Firebaugh SL, Schmidt MA, et al. Micromachined reactors for catalytic partial oxidation reactions. AIChE Journal 1997;43(11):3059–69.

[9] Shao Z, Haile SM, Ahn J, Ronney PD, Zhan Z, Barnett SA. A thermally self-sustained micro solid-oxide fuel-cell stack with high power density. Nature 2005;435(7043):795–8.

[10] Wu MH, Yetter RA and Yang V. Development and characterization of ceramic micro chemical propulsion and combustion systems, 46th AIAA aerospace sciences meeting and exhibit, AIAA-2008-966; 2008.

[11] Zhang K, Chou S, Ang S. MEMS-Based solid propellant microthruster design, simulation, fabrication, and testing. Journal of Microelectromechanical Systems 2004;13(2):165–75.

[12] London A, Ayon A, Epstein A, Spearing S, Harrison T, Peles Y, et al. Microfabrication of a high pressure bipropellant rocket engine. Sensors and Actuators A-Physical 2001;92(1–3):351–7.

[13] Lewis D, Janson S, Cohen R, Antonsson E. Digital micropropulsion. Sensor and Actuators A-physical 2000;80(2):143–54.

[14] Mehra A, Zhang X, Ayon AA, Waitz IA, Schmidt MA, Spadaccini CM. A six-wafer combustion system for a silicon micro gas turbine engine. Journal of Microelectromechanical Systems 2000;9:517–27.

[15] Epstein AH, Senturia SD, Al-Midani O, Anathasuresh G, Ayon, A, Breuer K, et al. Micro-heat engines, gas turbines, and rocket engines – the MIT microengine project, 28th Fluid Dynamics Conference, AIAA-1997-1773; 1997.

[16] Yang W. MEMS free-piston knock engine. Poster presentation, 28th international symposium on combustion; 2000.

[17] Aichlmayr HT, Kittelson DB, Zachariah MR. Miniature free-piston homogeneous charge compression ignition engine-compressor concept Part I: performance estimation and design considerations unique to small dimensions. Chemical Engineering Science 2002;57:4161–71.

[18] Dahm WA, Ni J, Mayor R, Qiao G, Dyer S, Benjamin A, et al. Micro internal combustion swing engine (MICSE) for portable power generation systems, 40th AIAA aerospace sciences meeting and exhibit, AIAA-2002-722; 2002.

[19] Annen KD, Stickler DB and Kebabian PL. Miniature generator, US Patent 664250; 2002.

[20] Miesse CM, Masel RI, Jensen CD, Shannon MA, Short M. Submillimeter-scale combustion. AIChE Journal 2004;50(12):3206–14.
[21] Davy H. Some researches on flame. Philosophical Transactions of the Royal Society of London; 1817:45–76.
[22] Zhang K, Chou S, Ang S. Development of a low-temperature co-fired ceramic solid propellant microthruster. Journal of Micromechanics and Micro-engineering 2005;15(5):944–52.
[23] Galie P, Xu B and Ju Y. Kinetic enhancement of mesoscale combustion by using a novel nested doll combustor, 45th AIAA aerospace sciences meeting and exhibit, AIAA-2007-576; 2007.
[24] Weinberg FJ. The first half-million years of combustion research and today's burning problems. Symposium (International) on combustion 1975;15(1):1–17.
[25] Lloyd SA, Weinberg FJ. A burner for mixtures of very low heat content. Nature 1974;251(5470):47–9.
[26] Jones AR, Lloyd SA, Weinberg FJ. Combustion in heat exchangers. Proceedings of the Royal Society of London A 1978;360:97–115.
[27] Takeno T, Sato K. An excess enthalpy flame theory. Combustion Science and Technology 1979;20(1–2):73–84.
[28] Ronney PD. Analysis of non-adiabatic heat-recirculating combustors. Combustion and Flame 2003;135(4):421–39.
[29] Ju Y, Choi CW. An analysis of sub-limit flame dynamics using opposite propagating flames in mesoscale channels. Combustion and Flame 2003; 133(4):483–93.
[30] Vican J, Gajdeczko BF, Dryer FL, Milius DL, Aksay IA, Yetter RA. Development of a microreactor as a thermal source for microelectromechanical systems power generation. Proceedings of the Combustion Institute 2002;29(1): 909–16.
[31] Sitzki L, Borer K, Wussow S, Schuster E, Maruta K, Ronney PD, et al. Combustion in microscale heat-recirculating burners, 39th aerospace sciences meeting and exhibit, AIAA-2001-1087; 2001.
[32] Maruta K, Takeda K, Sitzki L, Borer K, Ronney PD, Wussow S, et al. Catalytic combustion in microchannel for MEMS power generation. The third Asia-Pacific conference on combustion; 2001. pp. 219–22.
[33] Kyritsis DC, Guerrero-Arias I, Roychoudhury S, Gomez A. Mesoscale power generation by a catalytic combustor using electrosprayed liquid hydrocarbons. Proceedings of the Combustion Institute 2002;29:965–71.
[34] Miller F, Struk P, Dietrich D, T'ien J, Mellish B and Johnston M. Upstream catalytic flame propagation in a platinum channel: a comparison of model and experiment. In: Proceedings of 5th US combustion meeting; 2007. pp. 3265–77.
[35] Daou J, Matalon M. Influence of conductive heat-losses on the propagation of premixed flames in channels. Combustion and Flame 2002;128(4):321–39.
[36] Daou J, Matalon M. Flame propagation in Poiseuille flow under adiabatic conditions. Combustion and Flame 2001;124(3):337–49.
[37] Daou J, Dold J, Matalon M. The thick flame asymptotic limit and Damköhler's hypothesis. Combustion Theory and Modelling 2002;6(1):141–53.
[38] Ju Y, Xu B. Effects of channel width and Lewis number on the multiple flame regimes and propagation limits in mesoscale. Combustion Science and Technology 2006;178(10–11):1723–53.
[39] Ju Y, Minaev S. Dynamics and flammability limit of stretched premixed flames stabilized by a hot wall. Proceedings of the Combustion Institute 2002;29:949–56.
[40] Ju Y, Xu B. Theoretical and experimental studies on mesoscale flame propagation and extinction. Proceedings of the Combustion Institute 2005;30(2): 2445–53.
[41] Maruta K, Kataoka T, Kim NI, Minaev S, Fursenko R. Characteristics of combustion in a narrow channel with a temperature gradient. Proceedings of the Combustion Institute 2005;30(2):2429–36.
[42] Nakamura H, Fan A, Minamizono H, Maruta K, Kobayashi H, Niioka T. Bifurcations of stretched premixed flame stabilized by a hot wall. Proceedings of the Combustion Institute 2009;32(1):1367–74.
[43] Leach TT, Cadou CP. The role of structural heat exchange and heat loss in the design of efficient silicon micro-combustors. Proceedings of the Combustion Institute 2005;30:2437–44.
[44] Maruta K, Park JK, Oh KC, Fujimori T, Minaev SS, Fursenko RV. Characteristics of microscale combustion in a narrow heated channel. Combustion. Explosion and Shock Waves 2004;40(5):516–23.
[45] Richecoeur F, Kyritsis DC. Experimental study of flame stabilization in low Reynolds and Dean number flows in curved mesoscale ducts. Proceedings of the Combustion Institute 2005;30(2):2419–27.
[46] Evans CJ, Kyritsis DC. Operational regimes of rich methane and propane/oxygen flames in mesoscale non-adiabatic ducts. Proceedings of the Combustion Institute 2009;32(2):3107–14.
[47] Xu B, Ju Y. Experimental study of spinning combustion in a mesoscale divergent channel. Proceedings of the Combustion Institute 2007;31(2): 3285–92.
[48] Miesse C, Masel RI, Short M, Shannon MA. Diffusion flame instabilities in a 0.75 mm non-premixed microburner. Proceedings of the Combustion Institute 2005;30(2):2499–507.
[49] Xu B, Ju Y. Studies on non-premixed flame streets in a mesoscale channel. Proceedings of the Combustion Institute 2009;32(1):1375–82.
[50] Jackson TL, Buckmaster J, Lu Z, Kyritsis DC, Massa L. Flames in narrow circular tubes. Proceedings of the Combustion Institute 2007;31(1):955–62.
[51] Chen C-H, Ronney PD. Three-dimensional effects in counterflow heat-recirculating combustors. Proceedings of the Combustion Institute 2011;33(2): 3285–91.
[52] Xu B, Ju Y. Concentration slip and its impact on heterogeneous combustion in a micro scale chemical reactor. Chemical Engineering Science 2005;60(13): 3561–72.
[53] Xu B, Ju Y. Theoretical and numerical studies of non-equilibrium slip effects on a catalytic surface. Combustion Theory and Modelling 2006;10(6): 961–79.
[54] Aghalayam P, Bui PA, Vlachos DG. The role of radical wall quenching in flame stability and wall heat flux: hydrogen-air mixtures. Combustion Theory and Modelling 1998;2(4):515–30.
[55] Whitehead JC, Dittman MD and Ledebuhr AG. Progress toward hydrogen peroxide micropropulsion. 13th annual American Institute of Aeronautics and Astronautics, UCRL-JC-135319; 1999.
[56] Janson SW, Helvajian H, Breuer K. MEMS, microengineering and aerospace systems. 30th AIAA fluid dynamics conference, AIAA-1999-3802; 1999.
[57] Epstein A. Millimeter-scale, micro-electro-mechanical systems gas turbine engines. Journal of Engineering for Gas Turbines and Power-Transactions of the ASME 2004;126(2):205–26.
[58] Chia LC, Feng B. The development of a micropower (micro-thermophoto-voltaic) device. Journal of Power Sources 2007;165(1):455–80.
[59] Ohadi MM, Buckley SG. High temperature heat exchangers and microscale combustion systems: applications to thermal system miniaturization. Experimental Thermal and Fluid Science 2001;25(5):207–17.
[60] Wu M, Wang Y, Yang V, Yetter R. Combustion in meso-scale vortex chambers. Proceedings of the Combustion Institute 2007;31:3235–42.
[61] McCrink M, Plumlee DG, Moll AJ and Steciak J. Fabrication of a mono-propellant micro-nozzle using Low temperature co-fired ceramics. IMAPS/ACerS international conference and exhibition on ceramic interconnect and ceramic microsystems technologies (CICMT); 2006.
[62] Volchko SJ, Sung CJ, Huang Y, Schneider SJ. Catalytic combustion of rich methane/oxygen mixtures for micropropulsion applications. Journal of Propulsion and Power 2006;22(3):684–93.
[63] Younger DW, Lu ST, Choueiri E, Neidert JB, Black III RE, Graham KJ, et al. MEMS mega-pixel micro-thruster arrays for small satellite stationkeeping. in Proceedings of the 14th annual/USU conference on small satellites, SSC00-X-2; 2000.
[64] Yetter RA, Yang V, Wang Z, Wang Y, Milius D, Peluse M, et al. Development of meso and micro scale liquid propellant thrusters, 41st aerospace sciences meeting and exhibit, AIAA-2003-676; 2003.
[65] Moll AJ. Microsystems and microfluidics: why not LTCC?, IMAPS/ACerS 3rd international conference and exhibition on ceramic interconnect and ceramic microsystems technologies (CICMT); 2007.
[66] Epstein AH, Senturia SD, Anathasuresh G, Ayon A, Breuer K, Chen KS, et al. Power MEMS and microengines, TRANSDUCERS '97, 1997 international conference on solid state sensors and actuators; 1997. pp. 753–6.
[67] Mehra A, Waitz IA. Development of a hydrogen combustor for a micro-fabricated gas turbine engine. Hilton head island, South Carolina: Solid-State Sensor and Actuator Workshop; Jun. 8–11 1998.
[68] Spadaccini CM, Zhang X, Cadou CP, Miki N, Waitz IA. Preliminary development of a hydrocarbon-fueled catalytic micro-combustor. Sensors and Actuators, A: Physical 2003;103(1–2):219–24.
[69] Isomura K, Tanaka S, Togo S-i, Esashi M. Development of high-speed micro-gas bearings for three-dimensional micro-turbo machines. Journal of Micromechanics and Microengineering 2005;15(9):S222–7.
[70] Tanaka S, Hikichi K, Togo S, Murayama M, Hirose T, Sakurai T, et al., World's smallest gas turbine establishing Brayton cycle, the 7th international workshop on micro and nanotechnology for power generation and energy conversion applications (Power MEMS 2007); 2007. pp. 359–62.
[71] Fu K, Knobloch AJ, Martinez FC, Walther DC, Fernandez-Pello C, Pisano AP, et al. Design and experimental results of small-scale rotary engines. American Society of Mechanical Engineers, Micro-Electromechanical Systems Division Publication (MEMS); 2001.
[72] Fu K, Knobloch, Cooley BA, Walther DC, Fernandez-Pello C, Liepmann D, et al. Microscale combustion research for applications to MEMS rotary IC engine. In: Proceedings of the national heat transfer conference; 2001.
[73] Fu K, Walther DC, Fernandez-Pello AC, Liepmann D, Miyasaka K. Preliminary investigation of a small-scale rotary internal combustion engine. Western States Section/Combustion Institute; 1999. 1999 fall meeting.
[74] Fu K, Knobloch AJ, Martinez FC, Walther DC, Fernandez-Pello C, Pisano AP, et al. Design and fabrication of a silicon-based MEMS rotary engine. In: Proceedings of 2001 ASME international mechanical engineering congress and exposition, MEMS-23925; 2001.
[75] Hege JB. The Wankel rotary engine; a history. McFarland & Co; 2006.
[76] Aichlmayr H, Kittelson D, Zachariah M. Micro-HCCI combustion: experimental characterization and development of a detailed chemical kinetic model with coupled piston motion. Combustion and Flame 2003;135(3): 227–48.
[77] Gu Y, Mayor JR and Dahm WJA. Turbulence-augmented minimization of combustion time in mesoscale internal combustion engines, 44th AIAA aerospace sciences meeting and exhibit, AIAA-2006-1350; 2006.
[78] Weinberg FJ. Combustion temperatures: the future? Nature 1971; 233(September 24):239–41.

[79] Cohen AL, Ronney PD, Frodis U, Sitzki L, Meiburg EH and Wussow S. Microcombustor and combustion-based thermoelectric microgenerator; 2003, US patent. 6613972.

[80] Weinberg FJ, Rowe DM, Min G, Ronney PD. On thermoelectric power conversion from heat recirculating combustion systems. Proceedings of the Combustion Institute 2002;29:941–7.

[81] Kyritsis DC, Coriton B, Faure F, Roychoudhury S, Gomez A. Optimization of a catalytic combustor using electrosprayed liquid hydrocarbons for mesoscale power generation. Combustion and Flame 2004;139(1–2): 77–89.

[82] Deng WW, Klemic JF, Li XH, Reed MA, Gomez A. Liquid fuel microcombustor using microfabricated multiplexed electrospray sources. Proceedings of the Combustion Institute 2007;31:2239–46.

[83] Kim NI, Kato S, Kataoka T, Yokomori T, Maruyama S, Fujimori T, et al. Flame stabilization and emission of small Swiss-roll combustors as heaters. Combustion and Flame 2005;141(3):229–40.

[84] Kim NI, Aizumi S, Yokomori T, Kato S, Fujimori T, Maruta K. Development and scale effects of small Swiss-roll combustors. Proceedings of the Combustion Institute 2007;31:3243–50.

[85] Yuasa S, Oshimi K, Nose H, Tennichi Y. Concept and combustion characteristics of ultra-micro combustors with premixed flame. Proceedings of the Combustion Institute 2005;30:2455–62.

[86] Yoshida K, Tanaka S, Tomonari S, Satoh D, Esashi M. High-energy density miniature thermoelectric generator using catalytic combustion. Journal of Microelectromechanical Systems 2006;15(1):195–203.

[87] Okamasa T, Lee GG, Suzuki Y, Kasagi N, Matsuda S. Development of a micro catalytic combustor using high-precision ceramic tape casting. Journal of Micromechanics and Microengineering 2006;16(9):S198–205.

[88] Suzuki Y, Horii Y, Kasagi N and Matsuda S. Micro catalytic combustor with tailored porous alumina. In: Proceedings of the IEEE international conference on micro electro mechanical systems (MEMS); 2004. pp. 312–5.

[89] Kamijo T, Suzuki Y, Kasagi N, Okamasa T. High-temperature micro catalytic combustor with Pd/nano-porous alumina. Proceedings of the Combustion Institute 2009;32(2):3019–26.

[90] Karim AM, Federici JA, Vlachos DG. Portable power production from methanol in an integrated thermoeletric/microreactor system. Journal of Power Sources 2008;179(1):113–20.

[91] Federici JA, Norton DG, Brueggemann T, Voit KW, Wetzel ED, Vlachos DG. Catalytic microcombustors with integrated thermoelectric elements for portable power production. Journal of Power Sources 2006;161(2): 1469–78.

[92] Sirignano WA, Pham TK, Dunn-Rankin D. Miniature-scale liquid-fuel-film combustor. Proceedings of the Combustion Institute 2002;29(1):925–31.

[93] Pham TK, Dunn-Rankin D, Sirignano WA. Flame structure in small-scale liquid film combustors. Proceedings of the Combustion Institute 2007;31(2): 3269–75.

[94] Li YH, Chao YC, Amade NS, Dunn-Rankin D. Progress in miniature liquid film combustors: double chamber and central porous fuel inlet designs. Experimental Thermal and Fluid Science 2008;32(5):1118–31.

[95] Yang WM, Chou SK, Shu C, Li ZW, Xue H. A prototype microthermophotovoltaic power generator. Applied Physics Letters 2004;84(19): 3864–6.

[96] Deshmukh SR, Vlachos DG. Effect of flow configuration on the operation of coupled combustor/reformer microdevices for hydrogen production. Chemical Engineering Science 2005;60(21):5718–28.

[97] Yoshida K, Tanaka S, Hiraki H, Esashi M. A micro fuel reformer integrated with a combustor and a microchannel evaporator. Journal of Micromechanics and Microengineering 2006;16(9):S191–7.

[98] Federici JA, Wetzel ED, Geil BR, Vlachos DG. Single channel and heat recirculation catalytic microburners: an experimental and computational fluid dynamics study. Proceedings of the Combustion Institute 2009;32:3011–8.

[99] Kim C, Jin J, Kwon S. Micro catalytic combustor as a heat source for micro endothermic reactors. Diffusion and Defect Data Pt. B Solid State Phenomena 2007;119:223–6.

[100] Li YH, Lien YS, Chao YC, Dunn-Rankin D. Performance of a mesoscale liquid fuel-film combustion-driven TPV power system. Progress in Photovoltaics Research and Applications 2009;17(5):327–36.

[101] Boyarko GA, Sung C-J, Schneider SJ. Catalyzed combustion of hydrogen-oxygen in platinum tubes for micro-propulsion applications. Proceedings of the Combustion Institute 2005;30(2):2481–8.

[102] Chen X, Li Y, Zhou Z, Fan R. A homogeneously catalyzed micro-chemical thruster. Sensors and Actuators A-Physical 2003;108(1–3):149–54.

[103] Lewis B, Von Elbe G. Combustion, flames and explosions of gases. 3rd ed. Academic Press; 1987.

[104] Zeldovich YB, Barenblatt GI, Librovich VB, Makhviladze GM. The mathematical theory of combustion and explosions. Consultants Bureau; 1985.

[105] Spalding DB. A Theory of inflammability limits and flame-quenching. Proceedings of the Royal Society of London. Series A 1957;240(1220): 83–100.

[106] Joulin G, Clavin P. Linear stability analysis of nonadiabatic flames: diffusional-thermal model. Combustion and Flame 1979;35:139–53.

[107] Strehlow RA, Noe KA, Wherley BL. The effect of gravity on premixed flame propagation and extinction in a vertical standard flammability tube. Symposium (International) on Combustion 1988;21(1):1899–908.

[108] Ronney PD. On the mechanisms of flame propagation limits and extinguishment-processes at microgravity. Symposium (International) on Combustion 1988;22(1):1615–23.

[109] Law CK, Egolfopoulos FN. A kinetic criterion of flammability limits: the C–H–O-inert system. Symposium (International) on Combustion 1990; 23(1):413–21.

[110] Sibulkin M, Frendi A. Prediction of flammability limit of an unconfined premixed gas in the absence of gravity. Combustion and Flame 1990; 82(3–4):334–45.

[111] Lakshmisha KN, Paul PJ, Mukunda HS. On the flammability limit and heat loss in flames with detailed chemistry. Symposium (International) on Combustion 1990;23(1):433–40.

[112] Maruta K, Yoshida M, Ju Y, Niioka T. Experimental study on methane-air premixed flame extinction at small stretch rates in microgravity. Symposium (International) on Combustion 1996;26(1):1283–9.

[113] Platt J, T'ien J. Flammability of a weakly stretched premixed flame: the effect of radiation loss, Fall technical meeting, eastern section. Combustion Institute; 1990.

[114] Sung CJ, Law CK. Extinction mechanisms of near-limit premixed flames and extended limits of flammability. Symposium (International) on Combustion 1996;26(1):865–73.

[115] Guo H, Ju Y, Maruta K. Niioka T and Liu F, Radiation extinction limit of counterflow premixed lean methane-air flames. Combustion and Flame 1997;109(4):639–46.

[116] Ju Y, Guo H, Maruta K, Liu F. On the extinction limit and flammability limit of non-adiabatic stretched methane-air premixed flames. Journal of Fluid Mechanics 1997;342:315–34.

[117] Ju Y, Maruta K, Niioka T. Combustion limits. Applied Mechanics Reviews 2001;54(3):257–77.

[118] Holman JP. Heat transfer. Mcgraw-hill Professional. 720; 2001.

[119] Ferguson CR, Keck JC. On laminar flame quenching and its application to spark ignition engines. Combustion and Flame 1977;28:197–205.

[120] Kurdyumov VN, Fernandez-Tarrazo E. Lewis number effect on the propagation of premixed laminar flames in narrow open ducts. Combustion and Flame 2002;128(4):382–94.

[121] Kuo CH, Ronney PD. Numerical modeling of non-adiabatic heat-recirculating combustors. Proceedings of the Combustion Institute 2007;31:3277–84.

[122] Babkin VS, Drobyshevich VI, Laevskii YM, Potytnyalov SI. Fiz. Goreniya Vzryva 1983;19:17–26.

[123] Williams FA. Combustion theory. 2nd ed. Benjamin/Cummings; 1985.

[124] Joulin G, Deshaies B. On radiation-affected flame propagation in gaseous-mixtures seeded with inert particles. Combustion Science and Technology 1986;47(5–6):299–315.

[125] Zamashchikov V. Experimental investigation of gas combustion regimes in narrow tubes. Combustion and Flame 1997;108(3):357–9.

[126] Pizza G, Frouzakis CE, Mantzaras J, Tomboulides AG, Boulouchos K. Dynamics of premixed hydrogen/air flames in microchannels. Combustion and Flame 2008;152(3):433–50.

[127] Pizza G, Frouzakis CE, Mantzaras J, Tomboulides AG, Boulouchos K. Dynamics of premixed hydrogen/air flames in mesoscale channels. Combustion and Flame 2008;155(1–2):2–20.

[128] Raimondeau S, Norton D, Vlachos DG, Masel RI. Modeling of high-temperature microburners. Proceedings of the Combustion Institute 2002;29: 901–7.

[129] Norton DG, Vlachos DG. Combustion characteristics and flame stability at the microscale: a CFD study of premixed methane/air mixtures. Chemical Engineering Science 2003;58(21):4871–82.

[130] Norton DG, Vlachos DG. A CFD study of propane/air microflame stability. Combustion and Flame 2004;138(1–2):97–107.

[131] Kaisare NS, Vlachos DG. Optimal reactor dimensions for homogeneous combustion in small channels. Catalysis Today 2007;120(1):96–106.

[132] Marbach T and Agrawal A. A meso-scale combustor using annular porous inert media for heat recirculation. 43rd AIAA aerospace sciences meeting and exhibit, AIAA-2005-942; 2005.

[133] Ju Y and Xu B. Studies of the effects of radical quenching and flame stretch on mesoscale combustion. 44th AIAA aerospace sciences meeting and exhibit, AIAA-2006-1351; 2006.

[134] Masel RI. Principles of adsorption and reaction on solid surfaces. Wiley-Interscience; 1996.

[135] Kim KT, Lee DH, Kwon S. Effects of thermal and chemical surface-flame interaction on flame quenching. Combustion and Flame 2006;146(1–2): 19–28.

[136] Tsuboi Y, Yokomori T, Maruta K. Lower limit of weak flame in a heated channel. Proceedings of the Combustion Institute 2009;32:3075–81.

[137] Tsuboi Y, Yokomori T, Maruta K. Extinction characteristics of premixed flame in heated microchannel at reduced pressures. Combustion Science and Technology 2008;180(10–11):2029–45.

[138] Oshibe H, Nakamura H, Tezuka T, Hasegawa S, Maruta K. Stabilized three-stage oxidation of DME/air mixture in a micro flow reactor with a controlled temperature profile. Combustion and Flame 2010;157(8):1572–80.

[139] Yamamoto Y, Oshibe H, Nakamura H, Tezuka T, Hasegawa S, Maruta K. Stationary three-stage oxidation of a gaseous n-heptane/air mixture in a micro flow reactor with a controlled temperature profile. Proceedings of the Combustion Institute 2011;33(2):3259–66.

[140] Ahn J, Eastwood C, Sitzki L, Ronney PD. Gas-phase and catalytic combustion in heat-recirculating burners. Proceedings of the Combustion Institute 2005; 30(2):2463–72.

[141] Maruta K, Takeda K, Ahn J, Borer K, Sitzki L, Ronney PD, et al. Extinction limits of catalytic combustion in microchannels. Proceedings of the Combustion Institute 2002;29:957–63.

[142] Deutschmann O, Schmidt R, Behrendt F, Warnatz J. Numerical modeling of catalytic ignition. Symposium (International) on Combustion 1996;26: 1747–54.

[143] Lyubovsky M, Smith LL, Castaldi M, Karim H, Nentwick B, Etemad S, et al. Catalytic combustion over platinum group catalysts: fuel-lean versus fuel-rich operation. Catalysis Today 2003;83(1–4):71–84.

[144] Zerkle DK, Allendorf MD, Wolf M, Deutschmann O. Understanding homogeneous and heterogeneous contributions to the platinum-catalyzed partial oxidation of ethane in a short-contact-time reactor. Journal of Catalysis 2000;196(1):18–39.

[145] Appel C, Mantzaras J, Schaeren R, Bombach R, Inauen A, Kaeppeli B, et al. An experimental and numerical investigation of homogeneous ignition in catalytically stabilized combustion of hydrogen/air mixtures over platinum. Combustion and Flame 2002;128(4):340–68.

[146] Schwiedernoch R, Tischer S, Deutschmann O, Warnatz J. Experimental and numerical investigation of the ignition of methane combustion in a platinum-coated honeycomb monolith. Proceedings of the Combustion Institute 2002;29(1):1005–11.

[147] Norton DG, Wetzel ED, Vlachos DG. Fabrication of single-channel catalytic microburners: effect of confinement on the oxidation of hydrogen/air mixtures. Industrial & Engineering Chemistry Research 2004;43(16): 4833–40.

[148] Karagiannidis S, Mantzaras J, Jackson G, Boulouchos K. Hetero-/homo-geneous combustion and stability maps in methane-fueled catalytic microreactors. Proceedings of the Combustion Institute 2007;31: 3309–17.

[149] Deutschmann O, Maier LI, Riedel U, Stroemman AH, Dibble RW. Hydrogen assisted catalytic combustion of methane on platinum. Catalysis Today 2000; 59(1–2):141–50.

[150] Warnatz J, Maas U, Dibble RW. Combustion: physical and chemical fundamentals, modelling and simulation, experiments, pollutant formation. Springer; 1996.

[151] Chen GB, Chen CP, Wu CY, Chao YC. Effects of catalytic walls on hydrogen/air combustion inside a micro-tube. Applied Catalysis A: General 2007;332(1): 89–97.

[152] Miller JA, Bowman CT. Mechanism and modeling of nitrogen chemistry in combustion. Progress in Energy and Combustion Science 1989;15(4): 287–338.

[153] Chao YC, Chen GB, Hsu CJ, Leu TS, Wu CY, Cheng TS. Operational characteristics of catalytic combustion in a platinum microtube. Combustion Science and Technology 2004;176(10):1755–77.

[154] Fassihi M, Zhdanov VP, Rinnemo M, Keck KE, Kasemo B. A theoretical and experimental-study of catalytic ignition in the hydrogen oxygen reaction on platinum. Journal of Catalysis 1993;141(2):438–52.

[155] Norton DG, Vlachos DG, Chen JH. Hydrogen assisted self-ignition of propane/air mixtures in catalytic microburners. Proceedings of the Combustion Institute 2005;30(2):2473–80.

[156] Kaisare NS, Stefanidis GD, Vlachos DG. Comparison of ignition strategies for catalytic microburners. Proceedings of the Combustion Institute 2009;32(2): 3027–34.

[157] Chen GB, Chao YC, Chen CP. Enhancement of hydrogen reaction in a micro-channel by catalyst segmentation. International Journal of Hydrogen Energy 2008;33(10):2586–95.

[158] Karagiannidis S, Mantzaras J. Numerical investigation on the start-up of methane-fueled catalytic microreactors. Combustion and Flame 2010; 157(7):1400–13.

[159] Cho J-H, Lin CS, Richards CD, Richards RF, Ahn J, Ronney PD. Demonstration of an external combustion micro-heat engine. Proceedings of the Combustion Institute 2009;32(2):3099–105.

[160] Whalen S, Thompson M, Bahr D, Richards C, Richards R. Design, fabrication and testing of the P3 micro heat engine. Sensors and Actuators A-Physical 2003;104(3):290–8.

[161] Tameda K and Fujita O. A research on room temperature startability of small size DME catalytic combustor. The Seventh JSME-KSME thermal and fluids engineering conference; 2008. p. 98.

[162] Bird GA. Molecular gas dynamics and the direct simulation of gas flows. Oxford University Press; 1994.

[163] Kee RJ, Zhu H, Goodwin DG. Solid-oxide fuel cells with hydrocarbon fuels. Proceedings of the Combustion Institute 2005;30(2):2379–404.

[164] Pan L, Liu G, Lam K. Determination of slip coefficient for rarefied gas flows using direct simulation Monte Carlo. Journal of Micromechanics and Microengineering 1999;9(1):89–96.

[165] McNenly MJ, Gallis MA. Determining the applicability of slip models for MEMS flows. Sandia National Laboratories Internal Memo; 2002. Engineering Sciences Center, Sept. 18.

[166] Chou CP, Chen JY, Evans GH, Winters WS. Numerical studies of methane catalytic combustion inside a monolith honeycomb reactor using multi-step surface reactions. Combustion Science and Technology 2000;150(1): 27–57.

[167] Lee MB, Yang QY, Ceyer ST. Dynamics of the activated dissociative chemisorption of CH_4 and implication for the pressure gap in catalysis: a molecular beam-high resolution electron energy loss study. Journal of Chemical Physics 1987;87(5):2724.

[168] Glumac N. Personal communication; 2003.

[169] Bertagnolli KE, Lucht RP. Temperature profile measurements in stagnation-flow, diamond-forming flames using hydrogen cars spectroscopy. Symposium (International) on Combustion 1996;26(2):1825–33.

[170] Shankar N, Glumac N. Experimental investigations into the effect of temperature slip on catalytic combustion, Eastern states section meeting of the Combustion Institute. Pennsylvania State University; 2003.

[171] Kramers HA, Kistemaker J. On the slip of a diffusing gas mixture along a wall. Physica 1943;10(8):699–713.

[172] Papadopoulos D, Rosner D. Direct simulation of concentration creep in a binary gas-filled enclosure. Physics of Fluids 1996;8(11):3179–93.

[173] Scott CD. Wall boundary equations with slip and catalysis for multicomponent, nonequilibrium gas flows. NASA TM X-58111; 1973.

[174] Gupta RN, Scott CD, Moss JN. Slip-boundary equations for multicomponent nonequilibrium airflow. NASA Technical Paper; 1985:2452.

[175] Rosner DE, Papadopoulos DH. Jump, slip, and creep boundary conditions at nonequilibrium gas/solid interfaces. Industrial & Engineering Chemistry Research 1996;35(9):3210–22.

[176] Minaev S, Maruta K, Fursenko R. Nonlinear dynamics of flame in a narrow channel with a temperature gradient. Combustion Theory and Modelling 2007;11(2):187–203.

[177] Fan Y, Suzuki Y, Kasagi N. Experimental study of micro-scale premixed flame in quartz channels. Proceedings of the Combustion Institute 2009;32(2): 3083–90.

[178] Kessler DA, Short M. Ignition and transient dynamics of sub-limit premixed flames in microchannels. Combustion Theory and Modelling 2008;12(5): 809–29.

[179] Gamezo VN and Oran ES. Flame acceleration in narrow tubes: Applications for micropropulsion in low-gravity environments, 43rd AIAA aerospace sciences meeting and exhibit, AIAA-2005-0540; 2005.

[180] Pizza G, Frouzakis CE, Mantzaras J, Tomboulides AG, Boulouchos K. Three-dimensional simulations of premixed hydrogen/air flames in micro tubes. Journal of Fluid Mechanics 2010;658:463–91.

[181] Nayagam V, Williams FA. Rotating spiral edge flames in von Karman swirling flows. Physical Review Letters 2000;84(3):479.

[182] Pearlman HG, Ronney PD. Self-organized spiral and circular waves in premixed gas flames. Journal of Chemical Physics 1994;101(3):2632.

[183] Robbins K, Gorman M, Bowers J, Brockman R. Spiral dynamics of pulsating methane–oxygen flames on a circular burner. Chaos 2004;14:467.

[184] Fan A, Minaev S, Kumar S, Liu W, Maruta K. Regime diagrams and characteristics of flame patterns in radial microchannels with temperature gradients. Combustion and Flame 2008;153(3):479–89.

[185] Fan A, Minaev S, Kumar S, Liu W, Maruta K. Experimental study on flame pattern formation and combustion completeness in a radial microchannel. Journal of Micromechanics and Microengineering 2007;17(12): 2398–406.

[186] Kumar S, Maruta K, Minaev S, Fursenko R. Appearance of target pattern and spiral flames in radial microchannels with CH_4-air mixtures. Physics of Fluids 2008;20:024101.

[187] Kumar S, Maruta K, Minaev S. On the formation of multiple rotating pelton-like flame structures in radial microchannels with lean methane - air mixtures. Proceedings of the Combustion Institute 2007;31(2):3261–8.

[188] Kumar S, Maruta K, Minaev S. Pattern formation of flames in radial microchannels with lean methane-air mixtures. Physical Review E 2007;75: 016208.

[189] Fan A, Minaev S, Sereshchenko E, Fursenko R, Kumar S, Liu W, et al. Experimental and numerical investigations of flame pattern formations in a radial microchannel. Proceedings of the Combustion Institute 2009;32(2): 3059–66.

[190] Minaev S, Sereshchenko E, Fursenko R, Fan A, Maruta K. Splitting flames in a narrow channel with a temperature gradient in the walls. Combustion, Explosion, and Shock Waves 2009;45(2):119–25.

[191] Fan A, Minaev S, Sereshchenko E, Tsuboi Y, Oshibe H, Nakamura H, et al. Dynamic behavior of splitting flames in a heated channel. Combustion, Explosion, and Shock Waves 2009;45(3):245–50.

[192] Dellimore K and Cadou C. Fuel-air mixing challenges in micro-power systems. 42nd AIAA aerospace sciences meeting and exhibit 2004: AIAA-2004-301.

[193] Cheng TS, Chao YC, Wu CY, Li YH, Nakamura Y, Lee KY, et al. Experimental and numerical investigation of microscale hydrogen diffusion flames. Proceedings of the Combustion Institute 2005;30:2489–97.

[194] Matta LM, Neumeier Y, Lemon B, Zinn BT. Characteristics of microscale diffusion flames. Proceedings of the Combustion Institute 2002;29(1):933–9.

[195] Kuwana K, Tagami N, Mizuno S, Ida T. Extinction of laminar jet diffusion microflames. Proceedings of the Combustion Institute 2009; 32(2):3115–21.

[196] Diesel Net. Emission standard. Available from, http://www.dieselnet.com/standards/; 2009.

[197] Dec JE. Advanced compression-ignition engines—understanding the in-cylinder processes. Proceedings of the Combustion Institute 2009;32(2): 2727–42.

[198] Zhao F, Asmus TN, Assanis DN, Dec JE, Eng JA, Najt PM. Homogeneous charge compression ignition (HCCI) engines. SAE International; 2003.

[199] Christensen M, Johansson B. Influence of mixture quality on homogeneous charge compression ignition. SAE Transactions 1998;107(4):982454.

[200] Iwabuchi Y, Kawai K, Shoji T, Takeda Y. Trial of new concept diesel combustion system – premixed compression-ignition combustion. SAE Transactions 1999;108(3). 1999-01-0185.

[201] Christensen M, Hultqvist A, Johansson B. Demonstrating the multi-fuel capability of a homogeneous charge compression ignition engine with variable compression ratio. SAE Transactions 1999;108(3). 1999-01-3679.

[202] Kaneko N, Ando H, Ogawa H, Miyamoto N. Expansion of the operating range with in-cylinder water injection in a premixed charge compression ignition engine. SAE Transactions 2002;111(3). 2002-01-1743.

[203] Dec JE, Canaan RE. PLIF imaging of NO formation in a DI diesel engine. SAE Transactions 1998;107(3):980147.

[204] Weißbäck M, Csato J, Glensvig M, Sams T, Herzog P. Alternative combustion - an approach for future HSDI diesel engines. MTZ Worldwide 2003;64(9).

[205] Kook S, Bae C, Miles PC, Choi D, Pickett LM. The influence of charge dilution and injection timing on low-temperature diesel combustion and emissions. SAE Transactions 2005;114(4). 2005-01-3837.

[206] Ju Y, Sun W, Burke MP, Gou X, Chen Z. Multi-timescale modeling of ignition and flame regimes of n-heptane-air mixtures near spark assisted homogeneous charge compression ignition conditions. Proceedings of the Combustion Institute 2011;33(1):1245–51.

[207] Holladay JD, Wang Y, Jones E. Review of developments in portable hydrogen production using microreactor technology. Chemical Reviews 2004;104(10):4767–89.

[208] Pattekar AV, Kothare MV. A microreactor for hydrogen production in micro fuel cell applications. Journal of Microelectromechanical Systems 2004;13(1):7–18.

[209] Takahashi S and Wakai K. Microcombustor with a sintered porous catalytic layer. 45th AIAA/ASME/SAE/ASEE joint propulsion conference and exhibit, AIAA-2009-5246; 2009.

[210] Kawamura Y, Ogura N, Yamamoto T, Igarashi A. A miniaturized methanol reformer with Si-based microreactor for a small PEMFC. Chemical Engineering Science 2006;61(4):1092–101.

[211] Ryi S-K, Park J-S, Choi S-H, Cho S-H, Kim S-H. Novel micro fuel processor for PEMFCs with heat generation by catalytic combustion. Chemical Engineering Journal 2005;113(1):47–53.

[212] Lerou JJ, Tonkovich AL, Silva L, Perry S, McDaniel J. Microchannel reactor architecture enables greener processes. Chemical Engineering Science 2010;65(1):380–5.

[213] Esakov I, Grachev L, Khodataev K, Lavrov P and Ravaev A. Boundary- layer control based on localized plasma generation: development of the microwave system. 48th AIAA aerospace sciences meeting 2010: AIAA-2010-1003.

[214] Göksel B, Greenblatt D, Rechenberg I, Kastantin Y, Nayeri CN, Paschereit CO. Pulsed plasma actuators for active flow control at MAV Reynolds numbers. Notes on numerical fluid mechanics and multidisciplinary design, vol. 95. Springer; 2007.

[215] Manesh NA, Basu S, Kumar R. Experimental flame speed in multi-layered nano-energetic materials. Combustion and Flame 2010;157:476–80.

[216] Son SF, Yetter RA, Yang V. Introduction: nanoscale composite energetic materials. Journal of Propulsion and Power 2007;23(4):643–4.

[217] Sanders VE, Asay BW, Foley TJ, Tappan BC, Pacheco AN, Son SF. Reaction propagation of four nanoscale energetic composites (Al/MoO$_3$, Al/WO$_3$, Al/CuO, and Bi$_2$O$_3$). Journal of Propulsion and Power 2007;23(4):707–14.